UNIVERSITÀ DEGLI STUDI DI MILANO
Facoltà di Scienze Matematiche Fisiche e Naturali
Dottorato di Ricerca in Fisica, Astrofisica e Fisica Applicata

Study of the doubly and singly Cabibbo suppressed decays $D^+ \to K^+\pi^-\pi^+$ and $D_s^+ \to K^+\pi^-\pi^+$ in the FOCUS experiment

Coordinatore: Prof. Rodolfo Bonifacio

Tutore: Dott.ssa Sandra Malvezzi

Tesi di dottorato di:
Laura EDERA
Ciclo XVII

Anno Accademico 2004-2005

Abstract

This thesis illustrates a complete study of the doubly and singly Cabibbo suppressed decays D^+ and $D_s^+ \to K^+\pi^-\pi^+$.

Data for this analysis have been collected by the fixed-target high-energy photoproduction experiment FOCUS at Fermilab.

I have selected the D^+ and D_s^+ samples with cuts to obtain a sufficiently high statistics, a good signal to noise ratio and, at the same time, eliminate possible contaminations from the more copious and favoured decays. The D^+ yield consists of 189 ± 24 events, with a signal to noise ratio ~ 1; the D_s^+ yield is 567 ± 31 and the signal to noise ratio is ~ 2.5.

I have measured $\Gamma(D^+ \to K^+\pi^-\pi^+)/\Gamma(D^+ \to K^-\pi^+\pi^+) = 0.0065 \pm 0.0008 \pm 0.0004$ and $\Gamma(D_s^+ \to K^+\pi^-\pi^+)/\Gamma(D_s^+ \to K^+K^-\pi^+) = 0.127 \pm 0.007 \pm 0.014$, improving the previous determinations of a factor of 2 and 5, respectively.

I have also performed a Dalitz plot analysis for both decays. My amplitude analysis for $D_s^+ \to K^+\pi^-\pi^+$ represents the first available measurement for this channel.

Contents

List of Tables

List of Figures

Chapter 1

Charm meson decays: some achievements and open issues

Charm physics, since its discovery 30 years ago, has provided a lot of interesting results, contributing to the understanding of the Standard Model (SM) phenomenology, through measurements of lifetimes, branching ratio, subresonant analyses etc... In this sector the fixed-target experiments, in particular the more recent FOCUS and E791, have played a dominant role; they have contributed to sketch out the way to the present collider experiments, such as BABAR, BELLE, CDF, D0 and CLEO-c, addressing the open issues (mixing, CP violation etc...) and suggesting analysis tools and techniques.

With the high statistics and the excellent quality of data nowadays available, the charm physics is now at the center of a renewed attention. The experimental sensitivity has reached unprecedented levels; meson lifetimes (Section 1.1), as an example, are measured with a precision up to 1%, allowing to test various theoretical predictions. Charm physics is also able to indirectly search for physics beyond the SM; $D^0\bar{D}^0$ mixing (Section 1.2), CP violation (Section 1.3) and rare decays (Section 1.4) are expected to be small or forbidden in the SM; their evidence or deviations from expected prediction can be interpreted as sign of New Physics.

However, it is becoming more and more evident that the advantages of high statistics in the search of New Physics could vanish in absence of a strategy to control strong effects among particles involved in weak decay processes. Even the semileptonic sector, which is expected to be not heavily affected by Final State Interactions (FSI), had revealed some unexpected effects: the FOCUS analysis of the $D^+ \to K^-\pi^+\mu^+\nu$ channel[1] has indeed required to include a quantum mechanics interference between the S-wave and the dominant $K^*(892)$ to interpret the decay (Section 1.5) [1].

In the hadronic sector, strong effect complications can be more severe. A powerful and proper tool to investigate the charm hadronic decay dynamics is the Dalitz

[1] Unless otherwise stated, when referencing a particular state, its charge conjugate is implicitly included.

plot analysis. It provides the complete observation of the decay, through the measurement of coefficients and relative phases of the different amplitudes contributing to the same final state. The measurement of phase-shifts allows us to probe the role of FSI and to investigate other phase dependent effects, such as CP violation; an instructive example is the $D^+ \to K^+K^-\pi^+$, which it will be briefly discussed in Section 1.6. In general Dalitz plot analyses require high statistics and clean samples; this is why the present experimental scenario is still limited to a few decay channel results. The high statistics and the excellent quality of FOCUS data allow for extension to less investigated decays. In this thesis the Dalitz plot analysis of the doubly and singly Cabibbo suppressed decays D^+ and $D_s^+ \to K^+\pi^-\pi^+$ is presented, along with the measurement of their relative branching ratios. The Dalitz plot analysis of the $D_s^+ \to K^+\pi^-\pi^+$ presented here is the first measurement available for this channel.

All we are learning now in the charm sector will be important for the future b-physics experiments. Proper analysis techniques, developed and tested in charm decays, will be crucial for the interpretation of sophisticated measurements in the b-physics, such as CP violation. An example is the $B \to \rho\pi$ decay, which is a good candidate to measure the angle α of the SM Unitarity Triangle; in order to extract the desired specific $\rho\pi$ component, a fully coherent time-dependent Dalitz plot analysis of the three-pion final state is required. It is interesting to recall that just the three-pion final state investigation, from D^+ and D_s^+, has shown some limits of the formalism traditionally used to fit charm Dalitz plots and led the FOCUS collaboration to apply a more sophisticated approach [2] for their amplitude analysis to correctly interpret the results (Section 1.6).

1.1 Lifetimes

Lifetimes represent the most inclusive way of looking at charm particle decay. The lifetime is related to the total decay width via the expression:

$$\Gamma_T(C_x) = \sum_i \Gamma_i = \frac{\hbar}{\tau(C_x)} \tag{1.1}$$

Theoretical predictions for the decay rate into a given final state, i, are generally expressed in terms of the partial width Γ_i. The determination of lifetimes allows to convert the branching ratios measured by experiments to partial decay rates predicted, providing a challenging test for the theory.

Nowadays several experiments have measured the lifetimes with precisions that can reach fractions of % for the most long lived charmed particles. FOCUS is the only experiment (with the predecessor experiment E687) to have measured the lifetimes of all the weakly decaying charmed particles, providing lifetime ratios with minimum systematics effects. Fig. 1.1 shows a comparison between the PDG [5] values and

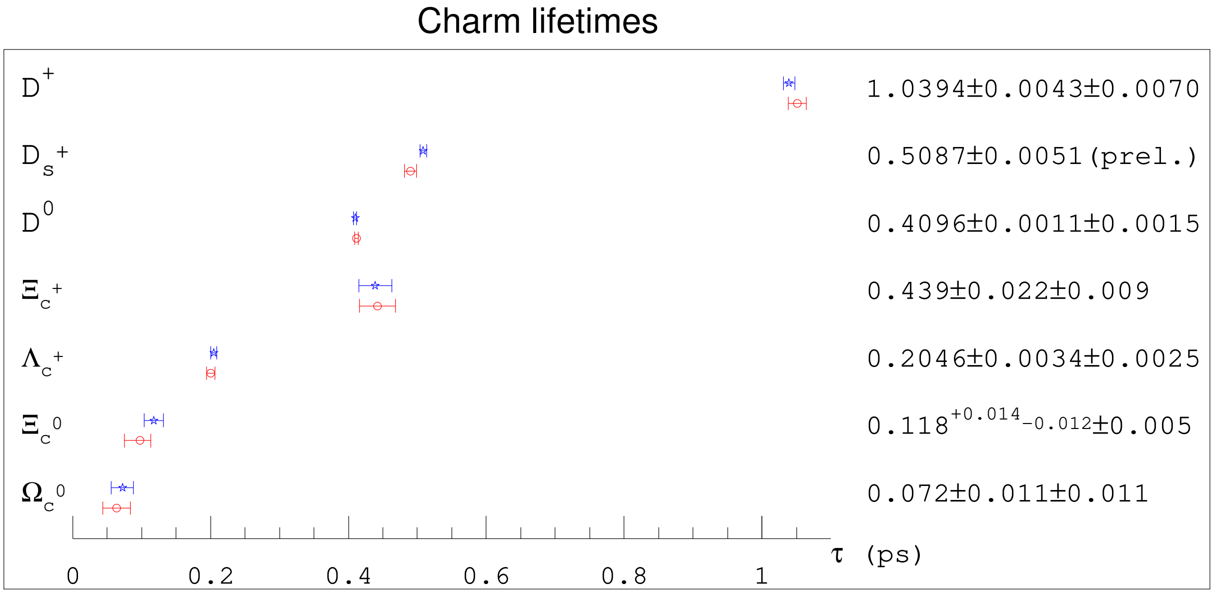

Figure 1.1: Charm particle lifetimes, comparison between the FOCUS lifetime measurements and the PDG [5] values. The $\star$ are the FOCUS results reported also on the right, while the $\circ$ correspond to the PDG values.

the FOCUS lifetime measurements. FOCUS produced new lifetimes results with precision better than the previous world average. An accurate measurement of the D^0 lifetime for the golden decay mode into $K\pi$ is a crucial ingredient to determine the lifetime difference, and consequently the parameter y of the $D^0 - \overline{D^0}$ mixing (Section 1.2).

The increasingly precise measurements of the heavy quark lifetimes have stimulated the further development of theoretical models, like the Heavy Quark Theory [6], which are able to predict successfully the rich pattern of charm hadron lifetimes, that span one order of magnitude from the longest lived D^+ to the shortest lived Ω_c^0. For the charm mesons a clear lifetime pattern emerges in agreement with the theoretical predictions: $\tau(D^0) < \tau(D_s^+) < \tau(D^+)$. Even the expectations for the charm baryon lifetimes reproduce the data; the experimental results lead to the following baryon lifetime hierarchy: $\tau(\Omega_c^0) \leq \tau(\Xi_c^0) < \tau(\Lambda_c^+) < \tau(\Xi_c^+)$.

1.2 Mixing

Mixing occurs because the two weak eigenstates D^0 and $\bar{D}^0$ are not mass eigenstates. If CP is conserved, $D_{1,2} = \frac{D^0 \pm \bar{D}^0}{\sqrt{2}}$ are mass and CP eigenstates with $\Delta\Gamma$ and ΔM different from 0. The probability that a D^0 meson produced at $t = 0$ decays as a

$\bar{D}^0$ at time t is given by

$$P(D^0 \to \bar{D}^0) = \frac{1}{4} e^{-\Gamma_1 t} \left\{ 1 - 2e^{\frac{-\Delta\Gamma}{2} t} \cos \Delta M t + e^{-\Delta\Gamma t} \right\} \tag{1.2}$$

We know experimentally that $\Delta M << \Gamma$ and $\Delta\Gamma << \Gamma$; in this limit, defining two dimensionless amplitudes $x = \frac{\Delta M}{\Gamma}$ and $y = \frac{\Delta\Gamma}{2\Gamma}$, we can write the mixing rate as

$$P(D^0 \to \bar{D}^0) = \frac{1}{4} e^{-\Gamma t} \Gamma^2 t^2 (x^2 + y^2) \tag{1.3}$$

where $\Gamma = \frac{\Gamma_1 + \Gamma_2}{2}$.

Two different ways of accessing the mixing parameters x and y are [7]:

1. measurements of wrong-sign D^0 decays, using either semileptonic or hadronic final states;
2. comparison of the lifetime of the D^0 measured in hadronic decays and to final states that are CP eigenstates.

The right-sign (RS) amplitudes are defined as $A_{\bar{f}} = A(D^0 \to \bar{f})$ and $\bar{A}_f = A(\bar{D}^0 \to f)$ and the wrong-sign (WS) amplitudes are $\bar{A}_{\bar{f}} = A(\bar{D}^0 \to \bar{f})$ and $A_f = A(D^0 \to f)$, where f and $\bar{f}$ are CP-conjugate final states. A D^0 can produce a WS hadronic final state either by undergoing a doubly Cabibbo suppressed decay or by first oscillating into a $\bar{D}^0$ that subsequently undergoes a Cabibbo favoured (CF) decay. The WS decay includes three components: one from the DCSD, a second from mixing and a third from the interference between the first two. Assuming CP conservation and expanding the decay rate up to $O(x^2)$ and $O(y^2)$ results in the following expression for the WS to RS decay rate:

$$r_D(t) = e^{-\Gamma t} \left(R_{DCS} + \sqrt{R_{DCS}}\, y' \Gamma t + \frac{1}{4}(x'^2 + y'^2) \Gamma^2 t^2 \right) \tag{1.4}$$

R_{DCS} is the DCS branching ratio relative to the CF mode, $y' = y \cos\delta - x \sin\delta$ and $x' = x \cos\delta + y \sin\delta$, δ being the strong phase difference between the CF and DCS decays. In the semileptonic mixing the situation is more easy since only the last term matters (with $x' = x$ and $y' = y$). The up-to-date experimental situation is summarized in Fig. 1.2 [8].

In the semileptonic sector FOCUS has measured, preliminarily, r_D in the mode $D^0 \to K^+ \mu^- \bar{\nu}_\mu$ to be less than 0.131% @ 95% C.L.

In the hadronic sector the specific case $f = K^+\pi^-$ is studied; the preliminary results from FOCUS are $x'^2 < 0.83\%$ @ 95% C.L. and $-7.2\% < y' < 4.1\%$ @ 95% C.L. The comparison with other experiment is shown in Table 1.1, where the measurements from the mixing without CP violation fit are reported.

The other method, largely used to study mixing effects, is based on the measurement and comparison of the lifetime for neutral D's decaying to final states of

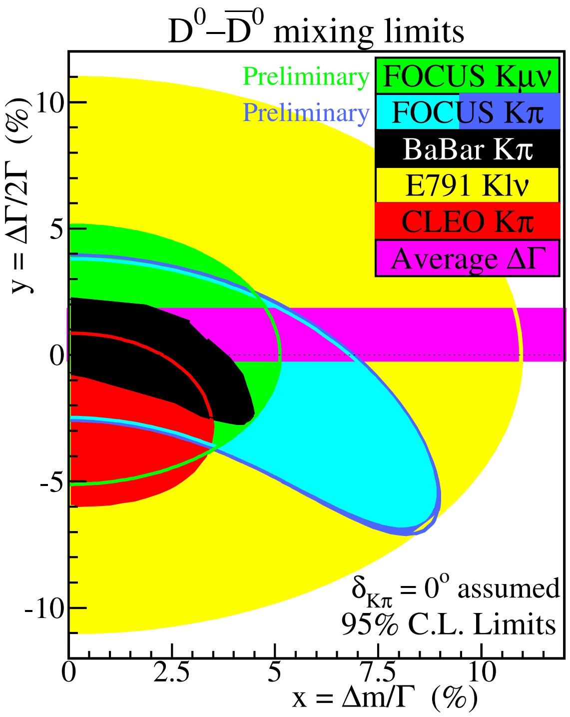

Figure 1.2: Mixing scenario.

Expt	R_{DCS}	x'^2 @95% C.L.	y' @ 95% C.L.
CLEO [9]	$0.47^{+0.11}_{-0.12} \pm 0.04$	$< 0.076\%$	$(-5.2, 0.2)\%$
BaBar [10]	0.31	$< 0.20\%$	$(-2.7, 2.2)\%$
Belle [11]	0.287 ± 0.037	$< 0.081\%$	$(-0.82, 1.6)\%$
FOCUS (prelim)	$0.382^{+0.167}_{-0.163} \pm 0.069$	$< 0.83\%$	$(-7.2, 4.1)\%$

Table 1.1: Summary of measurements from the mixing without CP violation fit.

Expt	y_{CP} (%)
FOCUS [12]	$3.4 \pm 1.4 \pm 0.7$
CLEO [13]	$-1.1 \pm 2.5 \pm 1.4$
Belle [14]	$-0.5 \pm 1.0 \pm 0.8$
BaBar [15]	$0.8 \pm 0.4^{+0.5}_{-0.4}$

Table 1.2: Current D^0 lifetime difference measurements.

pure even and odd CP. It is typically measured using the K^+K^- as the CP even final state and, in the absence of a suitable CP odd candidate, the CP mixed state $K^-\pi^+$ is used. Assuming that $K^-\pi^+$ is an equal mixture of CP even and CP odd, the relationship between the two lifetimes and the mixing parameters y_{CP} is given by:

$$y_{CP} = \frac{\Gamma(\text{CP-even}) - \Gamma(\text{CP-odd})}{\Gamma(\text{CP-even}) + \Gamma(\text{CP-odd})} = \frac{\tau(D^0 \to K^-\pi^+)}{\tau(D^0 \to K^-K^+)} - 1 \tag{1.5}$$

The experimental results are summed in Table 1.2; the FOCUS measurement [12] of $3.4 \pm 1.4 \pm 0.7$ is obtained using analysis techniques designed to minimize the relative systematic errors between the two samples and represents the most precise direct determination of the neutral D meson CP eigenstate lifetime difference.

1.3 CP violation

CP violation occurs if the decay rate for a particle differs from the decay rate of its CP-conjugate particle [16]. In the SM the D system is not as sensitive to CP violation as the K and B mesons are. The small effects predicted in the SM could leave open a window to the observation of new-physics effects. In charm meson decays (as well as in K and B) two classes of CP violation exist: indirect and direct. Indirect CP violation is mediated by D^0–$\bar{D}^0$ mixing and it is not expected to be a big effect. Direct CP violation requires the presence of both weak and strong relative phases between two or more interfering amplitudes, which contribute to a given final state. Let us consider the total decay amplitude α as $\alpha = A\exp^{i\delta_1} + B\exp^{i\delta_2}$, where A and B are two complex weak amplitudes and δ_i are the strong contributions due to the FSI. The weak contributions to the phases change sign when going to the CP-conjugate process, while the strong ones do not. Therefore we can define the CP violating asymmetry as:

$$A_{CP} = \frac{|\alpha|^2 - |\bar{\alpha}|^2}{|\alpha|^2 + |\bar{\alpha}|^2} = \frac{2Im(AB^*)sin(\delta_2 - \delta_1)}{|A|^2 + |B|^2 + 2Re(AB^*)cos(\delta_2 - \delta_1)} \tag{1.6}$$

So to obtain evidence of CP violating asymmetry it is mandatory to have two different interfering amplitudes with strong relative phases ($\delta_2 - \delta_1 \neq 0$). Good candidates

Decay mode	E791	CLEO
$D^0 \to K^-K^+$	$-0.010 \pm 0.049 \pm 0.012$	$0.000 \pm 0.022 \pm 0.008$
$D^0 \to \pi^-\pi^+$	$-0.049 \pm 0.078 \pm 0.030$	$0.030 \pm 0.032 \pm 0.008$
$D^0 \to K_sK_s$		-0.23 ± 0.19
$D^0 \to K_s\pi^0$		0.001 ± 0.013
$D^0 \to \pi^0\pi^0$		0.001 ± 0.048
$D^+ \to K^-K^+\pi^+$	-0.014 ± 0.029	
$D^+ \to \pi^-\pi^+\pi^+$	-0.017 ± 0.042	
	FOCUS	CDF
$D^0 \to K^-K^+$	$-0.001 \pm 0.022 \pm 0.015$	$0.020 \pm 0.012 \pm 0.006$
$D^0 \to \pi^-\pi^+$	$0.048 \pm 0.039 \pm 0.025$	$0.030 \pm 0.013 \pm 0.006$
$D^+ \to K^-K^+\pi^+$	$0.006 \pm 0.011 \pm 0.005$	
$D^+ \to K_s\pi^+$	$-0.016 \pm 0.015 \pm 0.009$	
$D^+ \to K_sK^+$	$0.071 \pm 0.061 \pm 0.012$	

Table 1.3: Measurements of CP asymmetries.

to search CP violation effects are the singly Cabibbo suppressed decays, since they can proceed via two different diagrams (spectator and penguin).

In Table 1.3 the experimental scenario is reported; CP asymmetries measured so far in the charm sector are consistent with zero within the errors.

1.4 Rare decays

One interesting way to search for physics beyond the SM is to look at decay modes that are extremely *rare* or *forbidden*. In the charm sector the rare and forbidden decay modes can be split mainly into three categories:

1. Flavor Changing Neutral Current (FCNC) such as $D^0 \to \ell^+\ell^-$ and $D^+ \to h^+\ell^+\ell^-$
2. Lepton Family Number Violating (LFNV) such as $D^+ \to h^+\ell_1^+\ell_2^-$
3. Lepton Number Violating (LNV) such as $D^+ \to h^-\ell_1^+\ell_{1,2}^+$

where h stands for π, K and ℓ for e, μ. The first decay modes (FCNC) are rare, with expected branching fraction of order 10^{-8} or less, proceeding largely via an internal quark loop (forbidden at tree level) [17]. The other two decay modes (LFNV and LNV) are strictly forbidden in the SM and test the conservation of the lepton family and of the lepton number.

The current experimental scenario concerning rare decay branching ratios is reported in Fig. 1.3. FOCUS has performed a complete analysis of the $D^+_{(s)} \to h^\pm\mu^\mp\mu^+$

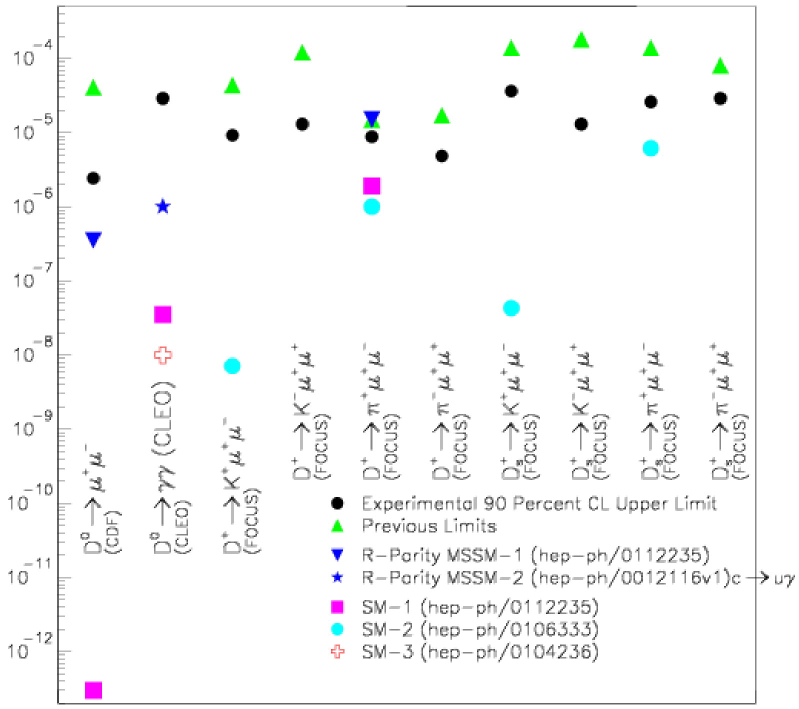

Figure 1.3: Measurements of rare decays.

modes [18], improving the previous limits [19, 20] of a factor from 2 to 14. The strength of the FOCUS fixed target experiment is the excellent vertexing, which was used to require that the two candidate leptons form a good, well separated vertex from the primary. In Table 1.4 the FOCUS measured limits, compared with the SM predictions and the previous determinations, are reported. The measurement of the $D^+ \to \pi^+\mu^+\mu^-$ branching ratio sets a new limit for the Minimal Supersymmetric Standard Model prediction [21].

In Fig. 1.3 other two interesting measurements are shown: the CDF upper limit for the decay $D^0 \to \mu^+\mu^-$ [22], which improves by a factor of two the previous bound, and the first limit determination of the $D^0 \to \gamma\gamma$ by CLEO [23].

1.5 Semileptonic decays

The semileptonic decays of charm mesons provide an ideal environment to study the charm phenomenology. The decay rates are computed from first principles, for example through Feynman diagrams, using Cabibbo-Kobayashi-Maskawa quark-mixing matrix elements. Involving only one hadron in the final decay stage implies that one does not have to worry about the usual FSI between hadrons. The possible complications coming from QCD corrections of the decay process are contained in

Mode	FOCUS	SM	Prev.
$D^+ \to K^+\mu^-\mu^+$	9.2	0.007	44
$D^+ \to K^-\mu^+\mu^+$	13	-	120
$D^+ \to \pi^+\mu^-\mu^+$	8.8	1.0	15
$D^+ \to \pi^-\mu^+\mu^+$	4.8	-	17
$D_s^+ \to K^+\mu^-\mu^+$	36	0.043	140
$D_s^+ \to K^-\mu^+\mu^+$	13	-	180
$D_s^+ \to \pi^+\mu^-\mu^+$	26	6.1	140
$D_s^+ \to \pi^-\mu^+\mu^+$	29	-	82

Table 1.4: Comparison between FOCUS measured limit on the branching fraction, the SM prediction and the previous best limit. All the entries are $\times 10^{-6}$.

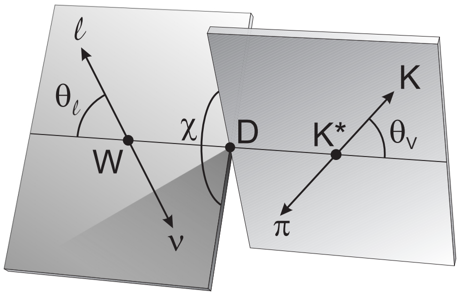

Figure 1.4: Definition of kinematic variables.

form factors. The form factors can be calculated by various models: HQET, Lattice QCD and quark models. However the recent FOCUS analysis of the vector channel $D^+ \to K^-\pi^+\mu^+\nu$ [1] have shown that decays in the semileptonic sector also reveal the presence of quantum mechanical effects and hadronic complications have to be dealt with in the analysis.

The kinematics of the 4-body decay is described by two invariant masses and three decay angles (defined in Fig. 1.4). The decay amplitude is written by using these five kinematic variables and three helicity-based form factors: $H_0(q^2)$, $H_+(q^2)$, and $H_-(q^2)$, which can be computed by the lattice QCD. The helicity form factors are combinations of one vector and two axial-vector form factors, which are parameterized in general as:

$$A_i(q^2) = \frac{A_i(0)}{1 - q^2/M_A^2}, \quad V(q^2) = \frac{V(0)}{1 - q^2/M_V^2} \tag{1.7}$$

Traditionally, three observables are used to describe the vector channel: the branch-

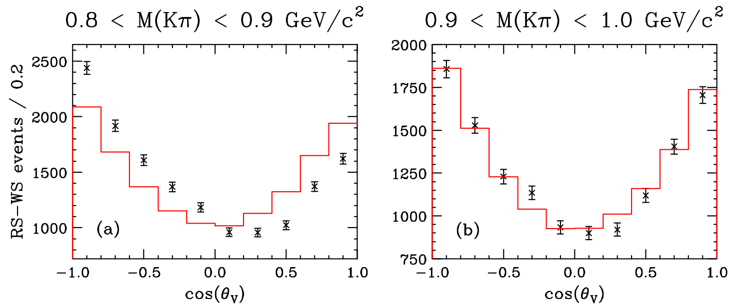

Figure 1.5: $\cos\theta_V$ distribution.

ing fraction and the form factor ratios r_V and r_2, which are defined as $V(0)/A_1(0)$ and $A_2(0)/A_1(0)$, respectively. During the form factor analysis, FOCUS checked the angular distribution of kaon in the $K\,\pi$ rest frame ($\cos\theta_V$) and found that it showed a huge forward-backward asymmetry below the $K^*(892)$ pole mass while almost no asymmetry above the pole (Fig. 1.5). Since the K^* is a P-wave, pure $K^* \to K\pi$ decays would have shown only a symmetric forward-backward $\cos\theta_V$ distribution over the entire $K\,\pi$ invariant mass range. This suggests a possible quantum mechanics interference between the Breit-Wigner amplitude describing the $\overline{K}^{*0}$ and a broad or nearly constant S-wave amplitude. A simple approach to emulate the interference effect is adding a spin zero amplitude in the matrix elements of the $D^+ \to K^-\pi^+\mu^+\nu$ decays. FOCUS assumed a simple toy S-wave model with a constant amplitude and a phase, and fitted the asymmetry. The amplitude was measured about 7% of the $\overline{K}^{*0}$ Breit-Wigner amplitude and the relative phase between the S-wave and the $\overline{K}^{*0}$ was measured at $\pi/4$. As shown in Fig. 1.6 where the invariant mass of the $K\pi$ particles are weighted by $\cos\theta_V$, the interference effect is reproduced with satisfaction. Interesting to note that the measured phase of $\pi/4$ is consistent with that found by LASS collaboration from the $K\pi$ phase-shift analysis [25].

FOCUS has then measured the form factor ratios of the $D^+ \to \overline{K}^{*0}\mu^+\nu$ decay [26] and its relative branching ratio [27], including the effects of the S-wave. Besides these measurements, FOCUS has performed (and it is performing) analyses on many semileptonic channels. All the results are summed in Table 1.5. In the vector semileptonic sector, it has calculated the $D_s^+ \to \phi\mu^+\nu$ relative branching ratio [27] and the corresponding form factor ratios [28]; these ratios are in good agreement with those obtained in the $D^+ \to \overline{K}^{*0}\mu^+\nu$ analysis, according to the flavour SU(3) symmetry. The first analysis of the $D^0 \to \overline{K}^0\pi^-\mu^+\nu$ and the study of the pseudoscalar channel $D^0 \to K^-\mu^+\nu$ are going to be published [29, 30].

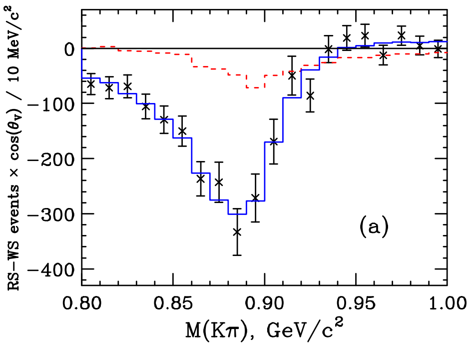

Figure 1.6: Asymmetry distribution in $K\pi$ invariant mass. The dashed line represents Monte Carlo simulation with no interfering S-wave amplitude while the solid line represents Monte Carlo simulation with S-wave amplitude.

Measured quantity	Value
$\Gamma(D^+ \to \overline{K}^{*0}\mu^+\nu)/\Gamma(D^+ \to K^-\pi^+\pi^+)$	$0.602 \pm 0.010 \pm 0.021$
$\Gamma(D_s^+ \to \phi\mu^+\nu)/\Gamma(D_s^+ \to \phi\pi^+)$	$0.54 \pm 0.033 \pm 0.048$
$\Gamma(D^+ \to \overline{K}^{*0}\mu^+\nu)/\Gamma(D^+ \to \overline{K}^0\mu^+\nu)$	$0.594 \pm 0.043 \pm 0.033$
$\Gamma(D^0 \to K^{*-}\mu^+\nu)/\Gamma(D^0 \to \overline{K}^0\pi^-\pi^+)$	$0.337 \pm 0.034 \pm 0.013$
$\Gamma(D^0 \to \pi^-\mu^+\nu)/\Gamma(D^0 \to K^-\mu^+\nu)$	$0.074 \pm 0.008 \pm 0.007$
$\lvert f_+^\pi(0)/f_+^K(0)\rvert$	$0.85 \pm 0.04 \pm 0.04 \pm 0.01$
r_V } from $D^+ \to \overline{K}^{*0}\mu^+\nu$	$1.504 \pm 0.057 \pm 0.039$
r_2 } from $D^+ \to \overline{K}^{*0}\mu^+\nu$	$0.875 \pm 0.049 \pm 0.064$
r_V } from $D_s^+ \to \phi\mu^+\nu$	$1.549 \pm 0.250 \pm 0.145$
r_2 } from $D_s^+ \to \phi\mu^+\nu$	$0.713 \pm 0.202 \pm 0.266$
r_V } from $D^0 \to \overline{K}^0\pi^-\mu^+\nu$	$1.706 \pm 0.677 \pm 0.342$
r_2 } from $D^0 \to \overline{K}^0\pi^-\mu^+\nu$	$0.912 \pm 0.370 \pm 0.104$

Table 1.5: FOCUS measurements in the semileptonic sector.

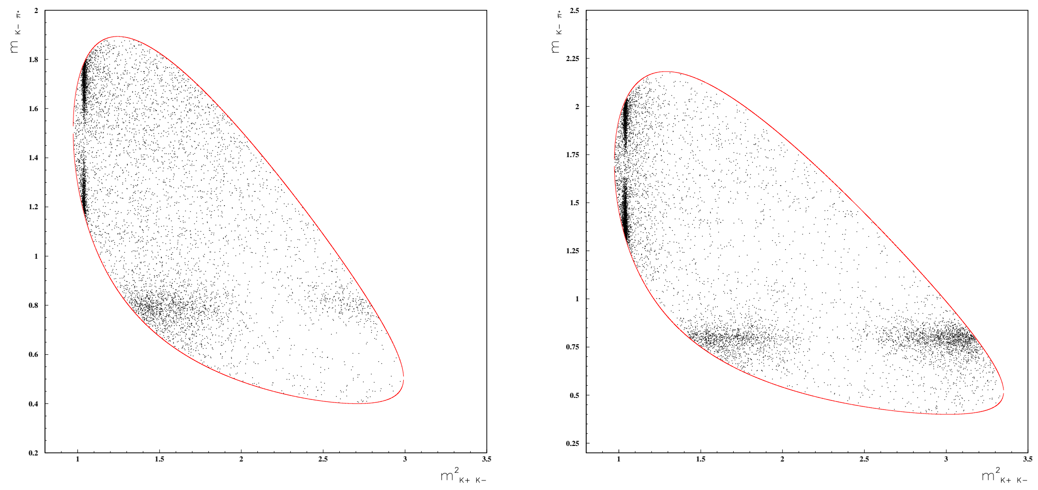

(a) D^+ (b) D_s^+

Figure 1.7: D^+ (a) and $D_s^+ \to K^+K^-\pi^+$ (b) Dalitz plots.

1.6 Amplitude analysis in hadronic decays

Charm meson decay dynamics has been extensively studied in the last decade. Dalitz plot has emerged as an unique tool to fully exploit the available charm statistics allowing to investigate the underlying decay dynamics. Through a Dalitz plot analysis, we can access to the coefficients and relative phases of the different amplitudes contributing to the same final state, thus obtaining the full set of observables of the decay. In particular the measurement of amplitude relative phases allows for probing those effects which are connected to phase phenomena, i.e. FSI and CP violation.

An instructive example is the $D^+ \to K^+K^-\pi^+$ decay. In this channel the FSI play an important role and induce a visible effect over the Dalitz plot. In Fig. 1.7 the Dalitz plots of the $D^+ \to K^+K^-\pi^+$ and $D_s^+ \to K^+K^-\pi^+$ decays are shown. Both the channels are dominated by the $\overline{K}^*(892)K^+$ and $\phi(1020)\pi^+$ states, visible over the Dalitz plots as horizontal and vertical bands, respectively. In the center of each band there is a node due to the angular momentum conservation for vector resonances (see Section 5.1 for details). The D^+ Dalitz plot shows, differently from the D_s^+, a pronounced asymmetry between the two lobes of the $\overline{K}^*(892)$ band; this can be explained through the interference of the $\overline{K}^*(892)K^+$ channel with a broad, spinless resonant channel. The weak amplitudes computed in a factorization model are real. However, complex phases can be acquired via long-range strong interactions between the final state hadrons [32]. From the interference pattern, one can infer that the data require a nearly imaginary relative phase shift. Indeed, modelling the $\overline{K}^*(892)$ as a Breit-Wigner function, with a term for the angular momentum conservation,

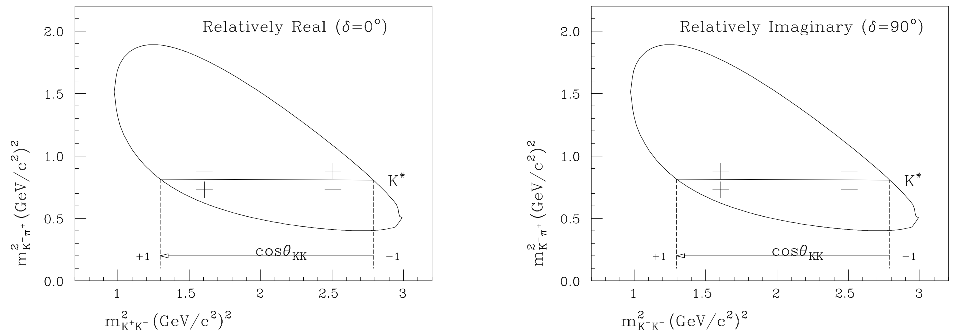

Figure 1.8: A graphical representation of the signs of the interference terms in the intensity function for real and imaginary phase differences.

and, for simplicity, the broad resonance as a nearly constant amplitude $\cos\delta + i\sin\delta$, the interference term is written as:

$$2Re\left[(\cos\delta + i\sin\delta)^* \frac{\cos\theta_{KK}}{m^2_{K^*} - m^2_{K\pi} - i\Gamma m_{K^*}}\right] = \tag{1.8}$$

$$= 2\frac{(m^2_{K^*} - m^2_{K\pi})\cos\theta_{KK}\cos\delta}{(m^2_{K^*} - m^2_{K\pi})^2 + \Gamma^2 m^2_{K^*}} + 2\frac{\Gamma m_{K^*}\cos\theta_{KK}\sin\delta}{(m^2_{K^*} - m^2_{K\pi})^2 + \Gamma^2 m^2_{K^*}}$$

As one moves in the direction of increasing m^2_{KK} mass along the $\overline{K}^*$ band, $\cos\theta_{KK}$ goes from $+1$ to -1 and both terms of Eq. (1.8) will switch sign. Along a line of constant m^2_{KK} mass, the first interference term, which dominates for relatively real amplitudes ($\delta = 0$), switches sign as one moves from $m^2_{K\pi}$ masses below the $\overline{K}^*$ resonance to masses above the resonance; the second interference term, which dominates for relatively imaginary amplitudes, does not change under this motion. The pattern for real and imaginary phase differences is illustrated in Fig. 1.8. When a complete Dalitz analysis is performed, these observations are confirmed [33]: the fit returns contributions of $\overline{K}^*(892)$ (with a fit fraction of about 20%) and of a broad and large scalar, the $\overline{K}^*(1430)$ ($\sim$ 67%), in a relatively imaginary phase configuration, pointing at relevant FSI effects, which manifest themselves as an asymmetry in the $\overline{K}^*$ band.

This decay channel is an example of how Dalitz plot analyses can provide an alternative approach to investigate CP violation effects. In general each measured phase in the Dalitz plot can be interpreted as a sum of two components, one CP conserving, the other CP violating: under CP conjugation the first does not switch sign, while the second does. Therefore differences between the relative phases of the CP-conjugate states for the various resonant channels could suggest CP violation effects. As discussed in Section 1.3, the two necessary requirements for detecting a

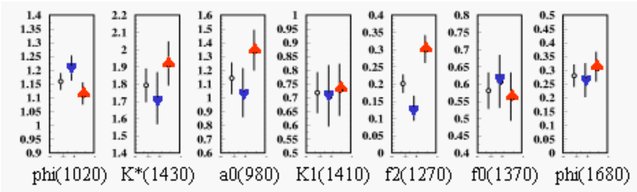

(a)

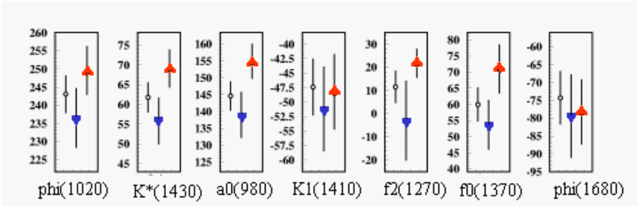

(b)

Figure 1.9: Amplitude coefficient and relative phases (in degrees) of all the resonant contributions of the $D^+ \to K^-K^+\pi^+$ decay: the circles are for the full sample, upward triangles for D^- and downward triangles for D^+.

CP asymmetry are the presence of two diagrams contributing to the final state and the presence of strong effects. The $D^+ \to K^-K^+\pi^+$ channel is a good candidate to observe CP effects: as just shown FSI are important and, being Cabibbo suppressed, it can proceed through two interfering diagrams (spectator and penguin). FOCUS has performed a complete Dalitz analysis on the two D^+/D^- split samples [33]. The comparison between the D^+/D^- results, shown in Fig. 1.9, do not suggest any CP violation manifestation. The relative phases are measured with an accuracy of about 5–10°; hopefully new higher statistics, such as those expected in the BTeV experiment, will allow for a sensitivity of the order of the degree.

However reliability of sophisticated measurements, such as CP violation, requires good control of amplitude parametrization and of strong effects. Charm has offered us a lesson in the $D^+ \to \pi^+\pi^-\pi^+$ decay. Traditionally, the decay amplitude is written as a sum of relativistic Breit-Wigner propagators multiplied by form factors plus a term describing the angular distribution of the two body decay of each intermediate state of a given spin (see Section 5.1). Following this method, fit of the $D^+ \to \pi^+\pi^-\pi^+$ [34] has required the introduction of an ad hoc resonance modelled as single Breit-Wigner function ($\sigma(600)$) to obtain a good fit C.L. When broad, overlapping and many channel scalar resonances play a dominant role in the decay, as in the $D^+ \to \pi^+\pi^-\pi^+$, it is necessary to well describe their contribution. FOCUS collaboration has performed a Dalitz plot analysis using a formalism based on the

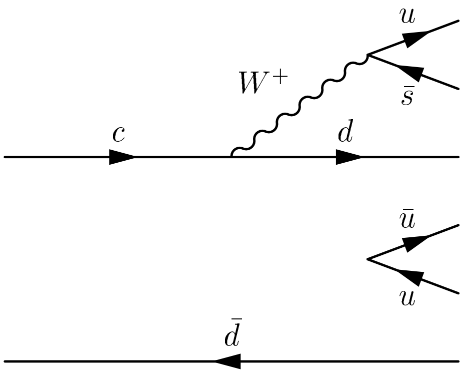

(a) $D^+ \to K^+\pi^-\pi^+$

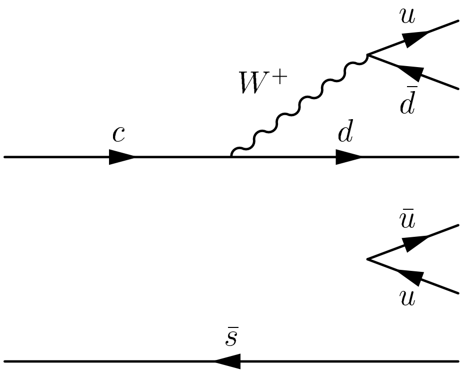

(b) $D_s^+ \to K^+\pi^-\pi^+$

Figure 1.10: Feynman diagram for the D^+ and $D_s^+ \to K^+\pi^-\pi^+$ decays.

K-matrix [35, 36] parametrization. This formalism treats the many channel and overlapping resonances imposing directly the two-body unitarity condition, which is not explicitly guaranteed with the Breit-Wigner approximation, and allows us to incorporate directly the results from the spectroscopy experiments. The results obtained are extremely encouraging, since the same *K-matrix* description gives a coherent picture of both two-body scattering measurements in light-quark experiments as well as charm meson decay, without the introduction of new ingredients not present in the scattering [2]. It will be interesting to perform the $D^+ \to K^+K^-\pi^+$ Dalitz plot analysis with this formalism.

1.6.1 The D^+ and $D_s^+ \to K^+\pi^-\pi^+$ decays

As previously shown through the examples of the $D^+ \to K^+K^-\pi^+$ and the $D^+ \to \pi^+\pi^-\pi^+$, the Dalitz plot analyses play a crucial role in the correct interpretation of the heavy flavour decays. To have a clear phenomenological picture it is mandatory to extend the analysis to many channels and enrich the experimental scenario. The Dalitz plot analyses of the doubly and singly Cabibbo suppressed decays D^+ and $D_s^+ \to K^+\pi^-\pi^+$ (DCSD and SCSD), subjects of this thesis, are a contribution in this direction; in particular the $D_s^+ \to K^+\pi^-\pi^+$ analysis is performed for the first time [37]. The results obtained show that both the channels are dominated by two vector states ($K^*(892)$ and $\rho(770)$), in a relative phase shift configuration almost real, suggesting a marginal role of FSI in these decays.

For these channels it is important to improve also the accuracy of the branching ratio measurements, which is still very poor. These decays are described, in the SM, through spectator Feynman diagrams, shown in Fig. 1.10. The branching ratios measured in this thesis are evaluated with respect to Cabibbo favoured decays, in particular the $D^+ \to K^-\pi^+\pi^+$ and the $D_s^+ \to K^+K^-\pi^+$; therefore the simple SM expectations for the branching ratios are $\tan^4\theta_C \sim 0.25\%$ for the D^+ and $\tan^2\theta_C \sim$

5% for the D_s^+. The branching ratios measured are $\Gamma(D^+ \to K^+\pi^-\pi^+)/\Gamma(D^+ \to K^-\pi^+\pi^+) = (0.65 \pm 0.08 \pm 0.04)\%$ and $\Gamma(D_s^+ \to K^+\pi^-\pi^+)/\Gamma(D_s^+ \to K^+K^-\pi^+) = (12.7 \pm 0.7 \pm 1.4)\%$ and differ from the expected values. The disagreement, in the D^+ branching ratio, can be due to the possible Pauli destructive interference in the normalization channel, absent in the DCSD since all the quarks in the final state have different flavours. This is the argument generally proposed to explain the lifetime difference between D^+ and D^0. In this simple picture one would expect, neglecting effects of final state interactions, $\tau(D^+)/\tau(D^0) = \Gamma(D^0_{\rm CF})/\Gamma(D^+_{\rm CF}) = (1/\tan^4\theta_{\rm C}) \times \Gamma(D^+_{\rm DCS})/\Gamma(D^+_{\rm CF})$. The comparison of $(1/\tan^4\theta_{\rm C}) \times \Gamma(D^+_{\rm DCS})/\Gamma(D^+_{\rm CF}) = 2.60 \pm 0.32$ with the precise FOCUS lifetime ratio $\tau(D^+)/\tau(D^0) = 2.538 \pm 0.023$ [38] and the marginal role of FSI inferred by the $D^+_{\rm DCS}$ Dalitz plot analysis, presented in this thesis, support the interpretation that destructive interference between spectator amplitudes with indistinguishable quarks in the CF D^+ final state is responsible for the lifetime difference between D^+ and D^0.

The FOCUS collaboration has already analysed the DCSD of the neutral meson $D^0 \to K^+\pi^-$ [39]; the study of the DCS decay of the charged D^+ meson presented in this thesis, free of any possible uncertainty due to $D^0\bar{D}^0$ mixing effects, provides complementary information.

The D_s^+ branching ratio measurement is improved of a factor of 5 with respect to the previous determination and it is measured to be lower than the expected simple SM prediction. A factor of two increase is caused by the different phase spaces of the two channels; the still remaining disagreement could be explained by FSI effects in the normalization channel. A Dalitz plot analysis of this channel will be interesting to interpret the decay.

Chapter 2

The FOCUS spectrometer

FOCUS is a photoproduction experiment which took data during the 1996–1997 Fermilab fixed target run. It is a considerably upgraded version of the previous experiment E687, using the same beamline and many of the same spectrometer components. The necessary modifications take into account the increase of a factor of 5 in the luminosity of the beam. FOCUS reconstructed more than one million Golden Mode charm decays (the decay modes $D^0 \to K^-\pi^+$, $D^+ \to K^-\pi^+\pi^+$, and $D^0 \to K^-\pi^+\pi^+\pi^-$), a factor of 10 increase over E687, enabling to perform precision studies of charm decays not possible before.

Charm particles are produced by the interaction of high energy photons, obtained by means of bremsstrahlung of electron and positron beams, with a beryllium oxide target. The mean energy of the photon beam is approximately 180 GeV. The FOCUS detector is a two magnet spectrometer with excellent vertexing and particle identification. It is shown schematically in Fig. 2.1. It is divided into two portions, termed "inner" and "outer". The inner portion subtends small angles (less than about 30 mrad) and consists of the detectors downstream of the second magnet. The outer portion subtends larger angles and is the portion of the spectrometer between the two magnets. The charged particles, which emerge from the target, enters from the upstream direction and are tracked by a silicon microvertex detectors, providing high resolution separation of primary (production) and secondary (decay) vertices. The momentum of a charged particle is determined by measuring its deflections in two analysis magnets of opposite polarity with five stations of multiwire proportional chambers. Three multicell threshold Čerenkov counters are used to identify particles. The detector is completed by electromagnetic and hadronic calorimeters and muon identification systems.

2.1 The photon beam

Obtaining the final photon beam for FOCUS, from the proton beam produced in the Tevatron, is a multi-step process involving three production targets (in addition to the experimental target). A schematic of the photon beamline is shown in 2.2.

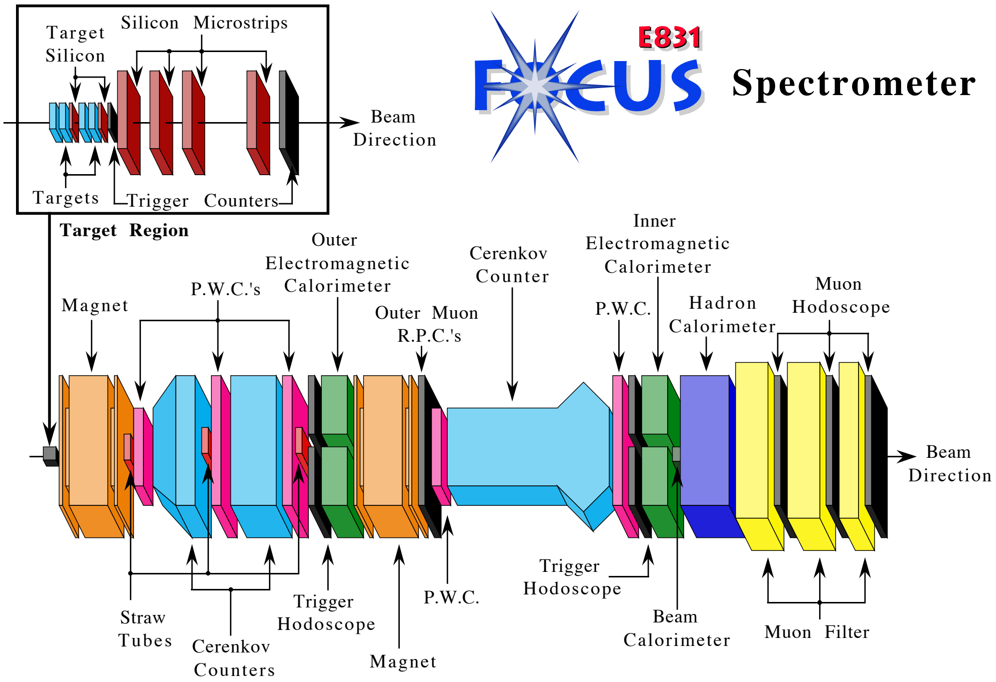

Figure 2.1: An overview of the elements of the FOCUS spectrometer. The inset shows an expanded view of the target region.

Incident 800 GeV protons strike a liquid deuterium target, producing, among other particles, π^0s which decay promptly ($\tau \sim 10^{-16}$ s) into two photons. Charged particles produced in the target are swept aside using powerful dipole magnets while the neutral component of the beam strikes the photon converter, a sheet of lead 50% of a radiation length thick. Photons convert to e^+e^- pairs while other neutral particles, owing to the small number of interaction lengths, usually pass through. After the electrons and positrons are focused with quadrapole magnets, the charged portion of the beam is bent around a dump which absorbs the uninteracting neutral particles. The beam is momentum selected by being passed through collimators. For most of the FOCUS running the nominal beam energy was chosen to be 300 GeV. The electrons and positrons are transported by separate beamlines towards the experimental apparatus. The two beams are recombined into a single beam by the momentum recombining dipoles. The combined beam is refocused and impacts the radiator which is a sheet of lead 20% of a radiation length thick where photons are produced by the bremsstrahlung process. After the beam passes through the radiator, powerful sweeping magnets remove the remaining charged portion of the beam which is directed into two calorimeters. The neutral portion of the beam (primarily photons) continues towards the experimental target. The mean photon energy produced by the 300 GeV electron beam is about 180 GeV.

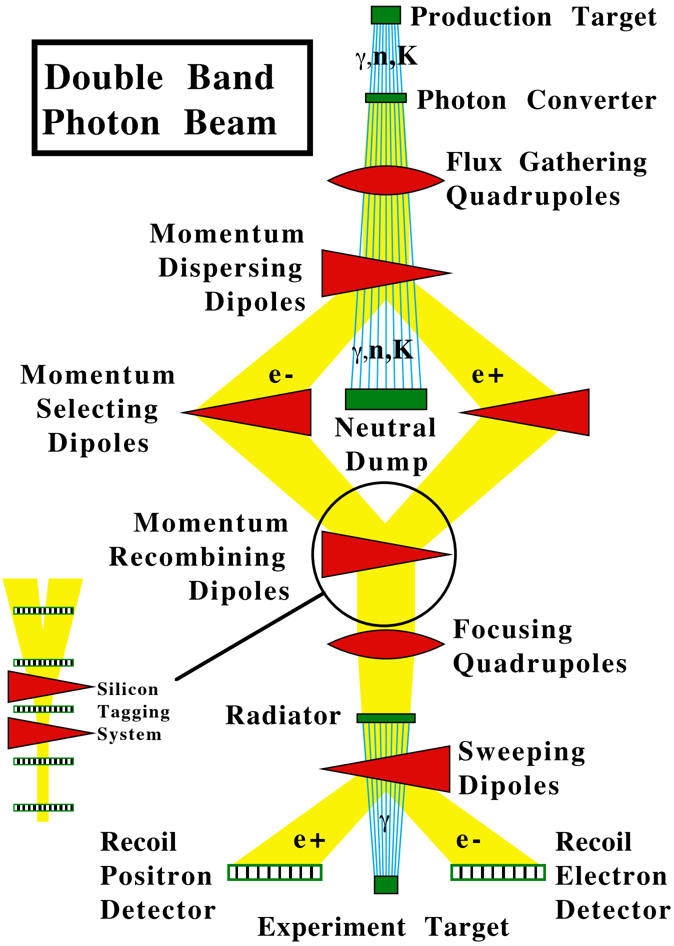

Figure 2.2: A schematic view of the major elements of the photon beamline. The inset shows a schematic view of the electron beam tagging system.

2.2 Target configuration

The FOCUS target is set up of four beryllium oxide (BeO) targets with embedded silicon strip detectors. This choice has been driven by the E687 experience, which has shown that requiring secondary decay vertices to be outside of the target material greatly increases the cleanliness of charm signals. The segmentation allows a large number of "out-of-target" decays. Studies have shown that a large portion of the out-of-target background comes from other charm decays which are easier to model than production and re-interaction processes. The final FOCUS target configuration is shown in 2.3.

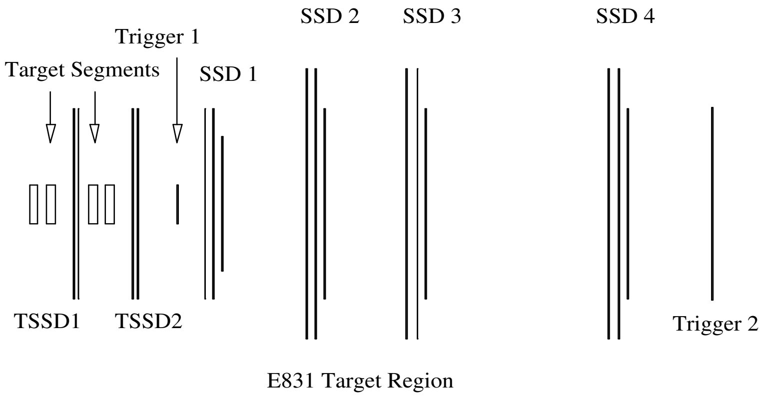

Figure 2.3: Diagram of the target region. Shown are the BeO targets, the embedded silicon microstrip (TSSD) planes, the downstream silicon microstrip (SSD) planes, and triggering hodoscopes. The beam enters from the left.

2.3 Silicon microstrip tracking

Tracking and vertexing in the target region is performed by two silicon microstrip systems.

The first system is embedded between target segments; it consists of two stations of high resolution silicon strip detectors. The first station of the Target Silicon or TSSD is positioned between the second and third target segments. The second station is located just after the last target segment and upstream of the first trigger counter. Each station has two views oriented at $\pm 45°$ from horizontal; each view has 1024 strips with 25 μm spacing, creating an active region about 25 mm across. This dimension is well matched to the beam size and to the extent of the target segments. The Target Silicon system was only in place for the 1997 running of FOCUS which comprises about 2/3 of the data collected.

The second system is located downstream of the target and upstream of the first magnet. Tracking is performed by a system of silicon microstrip detectors referred to as the Silicon Strip Detector (SSD). There are four stations of detectors, as shown in 2.3 and labeled as “SSD.” Each station has 3 views. With respect to the horizontal axis of the experiment, the three views are oriented at $-135°$, $-45°$, and $-90°$ from most upstream to most downstream. The planes within a station are separated by 5 mm. The first three stations are separated by 6 cm; the last two stations are separated by 12 cm. Each plane consists of two regions, an inner region with finer pitch strips and an outer region with more widely spaced strips. The most upstream station has 25 μm inner strips and 50 μm outer strips. The remaining three stations have 50 μm inner strips and 100 μm outer strips.

2.4 Analysis magnets

To find the momentum of tracks, we use two high current, large aperture analysis magnets. The momentum of a particle is determined by measuring the change in the slopes of tracks before and after each magnet. The first magnet, M1, is just downstream of the silicon vertex detectors. The second magnet, M2, is in the center of the spectrometer, between the third and fourth wire chambers. The two magnets are operated with opposite polarities and deflect charged particles in the vertical direction; the net result of both magnets is an approximate refocusing of charged particles in the vicinity of the hadronic calorimetry.

2.5 Multiwire proportional chambers

Tracking downstream of the first magnet is accomplished using five multiwire proportional chambers (called PWCs). Each PWC has four planes per station. The stations are labeled (from most upstream to most downstream) P0, P1, P2, P3, and P4. The tracks are naturally divided tracks into two categories: 3-chamber tracks ("outer") which are outside the aperture of M2 and 5-chamber tracks ("inner") which traverse the entire spectrometer. Each chamber has four planes of sense wires. The X wires run vertically and measure the position in the horizontal direction. The Y planes measure the horizontal position. The U and V planes are inclined at $\pm 11.3°$ from the horizontal. This arrangement is shown in 2.4.

2.6 Straw tube chambers

Three straw tube chambers were constructed to cover the pair region of each of the first three PWCs, to take into account the possibility that the PWC system would not be able to handle the high rates present in the pair region and that the PWCs would have to be "deadened" in this region. The first two chambers ST0 and ST1 are placed just in front of P0 and P1 respectively, ST2 is placed just behind P2. There are three views per station, one vertical and two aligned at $\pm 11.3°$ from vertical. Each view has three layers of straws. In the end, deadening the PWC system was not necessary, so the straw tubes were not needed for tracking, but they were used to provide useful information about the timing of events.

2.7 Čerenkov system

The FOCUS spectrometer includes three threshold Čerenkov detectors. We look for the presence or absence of light to identify a particle. For a given track momentum we determine the four particle identification possibilities (e, π, K, and p). The gases in the detectors have been chosen to provide wide momentum ranges over

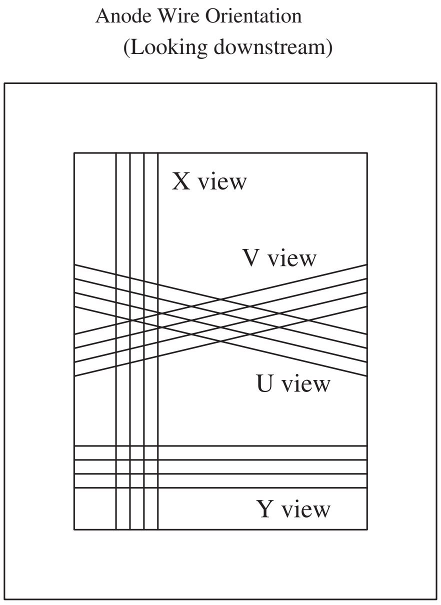

Figure 2.4: Orientation of the PWC wire planes, showing the $\pm 11.3°$ angle of the U and V planes with respect to the horizontal.

Detector	Gas	Threshold (GeV/c)		
		π	K	p
C1	58% He/42% N_2	8.5	29.9	56.8
C2	N_2O	4.5	16.2	30.9
C3	He	17.0	61.0	116.2

Table 2.1: Gases and threshold momenta of the three Čerenkov detectors.

which pions can be distinguished from kaons and protons. There is also a wide range over which kaons and protons can be distinguished from each other. The three Čerenkov detectors are called C1, C2, and C3. The properties of the Čerenkov detectors are summarized in Table 2.1.

The C1 detector is located between P0 and P1. It is filled with a 58% helium, 42% nitrogen mixture, which gives the detector a pion threshold of 8.5 GeV/c. The design of C2 is similar to C1. This Čerenkov detector is located between P1 and P2 and is filled with nitrous oxide (N_2O) gas which has a pion threshold of 4.5 GeV/c. The final Čerenkov detector in the FOCUS spectrometer is C3, a helium filled device with a pion threshold of 17.0 GeV/c, located between P3 and P4. From Table 2.1 it follows that the pions can be distinguished without ambiguity in the range (4.5 – 61.0) GeV/c, the kaons in the range (16.2–56.8) GeV/c and the protons in the ranges (16.2–56.8) GeV/c and (61.0–116.2) GeV/c.

2.8 Calorimetry

Calorimetry is especially important for reconstructing neutral particles since these particles leave no ionization in any of the tracking systems. In FOCUS, these particles are the γ and the π^0 (decaying to two photons) which are detected by electromagnetic calorimeters. The hadronic calorimeter detects the K^0_L and neutrons. The electromagnetic calorimeters are also used for electron identification.

There are two electromagnetic calorimeters, named inner and outer (IE and OE). The IE is positioned just after the last PWC and detects and measures the energy of electromagnetic particles that are within the acceptance of M2. Its energy resolution is about 5%. The OE is positioned just in front of M2 and detects photons and electrons produced at wider angles, outside the acceptance of M2. Its angular acceptance is of $28 \leq |\theta_x| \leq 142$ mrad and $49 \leq |\theta_y| \leq 114$ mrad and its resolution is given by $3\% + 15\% \sqrt{E(GeV)}$.

The hadron calorimeter (HC) is positioned behind the IE. It measures the energy of hadronic particles within the acceptance of M2. Its energy resolution is given by $0.86\% {+} 85\% \sqrt{E(GeV)}$. The HC also plays a crucial role in the first level of triggering by providing a fast sum of the hadronic energy in each event.

2.9 Muon detectors

The fact that pions and muons have very similar masses makes separation by Čerenkov thresholds possible only in very limited momentum ranges. Instead, we exploit the fact that muons interact weakly in material to make the identification. Thick block of iron are used to range out showers from electrons, pions and other hadrons. Particles detected beyond the iron are likely to be muons.

The FOCUS experiment has two muon detection systems. The outer muon system uses the steel of M2 as its filter. Muon hits are detected in resistive plate chambers. The detectors cover the region outside the M2 aperture. The inner muon system consists of three stations of scintillating hodoscopes. Each station is proceeded by a steel block.

2.10 The trigger

FOCUS typically had $\sim 100 \times 10^6$ (mostly electromagnetic) interactions per spill and only triggered on $\sim 30 \times 10^3$ (mostly hadronic) interactions per spill. In order to identify and select physically interesting events and to reduce the data rate to an acceptable level, a triggering system is used. FOCUS employs two levels of trigger referred to as the master gate and the second level trigger. High speed detector elements placed at various strategic locations throughout the spectrometer provide the summary information on which the trigger decisions are based.

2.10.1 Trigger elements

There are several scintillating hodoscopes in the experiment which are used exclusively for triggering. Additional informations from the IE, HC, OM and PWC's are also used in the trigger.

AM and AMD: In order to reduce the number of triggered events due to muons from the primary production target, it is necessary to have a reliable way of detecting muons entering the experiment. The AM and AMD hodoscope arrays are two "walls" of scintillator upstream of the target surrounding the beam. A coincidence between the two arrays is an excellent indication that a "halo" muon[1] is present in the spectrometer. This signal is used as a veto on certain muon triggers.

TR1: This counter is situated between the last Target Silicon and the first SSD planes. This counter consists of a thin scintillator with a PMT readout. The purpose of TR1 is to positively identify that an interaction has occurred in the target.

TR2: This "counter" consists of four individual counters arranged in quadrants, just downstream of the last SSD plane. The four signals are discriminated and combined with a logical OR. A pulse in this counter indicates that a charged particle entered the aperture of M1.

H×V: This array of 36 counters is positioned between C3 and the IE. The H×V has a central gap to avoid counting conversion pairs. The counters from this detector are input into a fast trigger logic module which supplies two output signals: $(H\times V)_1$ and $(H\times V)_2$ which signal that at least one or two charged particles, respectively, have passed through the array.

OH: This array of 24 counters is positioned at the front of the OE. The OH array has an aperture sized to match the aperture of M2 and a gap in the center of the array to avoid detecting electron pairs. We derive the signal OH_1 from the array, which signifies that at least one particle passed through the OH array.

IM1 and IM2: These hodoscopes are positioned in approximately the same locations as the MH2 and MH3 arrays. IM1H and IM1V are positioned just downstream of MH2; IM2H is positioned just upstream of MH3. The individual counters are much larger than those in the MH systems and are used only for triggering purposes. All the signals from these counters are input into the same logic used to form the $(H\times V)_1$ and $(H\times V)_2$ signals. The corresponding signals from the IM arrays are called IM_1 and IM_2 and signify that at least one or two muons were observed in the inner region.

[1]A muon produced far upstream in the primary target. When these reach the experiment they usually have very low angles.

2.10.2 The master gate

The master gate is the first level of triggering in FOCUS. Information from the trigger elements listed in the previous section are used to produce 8 master gate trigger outputs. Each of the 8 triggers selects different types of physics and diagnostic events. The data used in this analysis come in through the hadronic trigger. It consists of the following signal:

$$TR_1 \cdot TR_2 \cdot [(H \times V)_2 + (H \times V)_1 \cdot OH_1] \cdot E_{HI} \tag{2.1}$$

where we use the standard logical algebra that '+' is a logical OR and '$\cdot$' is a logical AND. E_{HI} represents a request on the hadronic energy over a high threshold. The expression between the squared brackets is the 2-body requirement, i.e. "two particles in the inner region or one in the inner region and one in the outer region."

2.10.3 The second level trigger

If the event passes the MG selection criteria, the readout process begins. The second level trigger logic begins to work on its triggering decision, 1.2 μs after the MG decision is made. Again, the events used in this thesis come through the hadronic trigger. In the second level there are two additional requirements made for hadronic events. The first is a minimum IE energy sum and the second is a PWC hit multiplicity that is consistent with 4 tracks in the system.

Events passing the second level trigger are readout and written to tape for future analysis. It takes about 1 ms to readout an event. During this time no other events can trigger the system. This period is known as the deadtime. If the event fails the second level trigger the system resets with a deadtime of about 1.5 μs.

Chapter 3

Signal selection

3.1 Data reconstruction

The reconstruction of the events in FOCUS proceeds through different steps:

- track reconstruction:
  the SSD and PWC tracks are reconstructed by proper algorithms and then linked, i.e. associated with each other;

- momentum determination:
  track momenta are measured by determining the deflection angle in one of the two large aperture analysis magnets;

- particle identification:
  the Čerenkov identification algorithm is based on likelihood ratios between the various particle hypotheses. The product of all firing probabilities for all cells within the three Čerenkov cones produces a χ^2-like variable $W_{\text{obs}}(i) = -2\ln\mathcal{L}$ where i ranges over the electron, pion, kaon and proton hypothesis. Čerenkov identification is performed by cutting on the difference between two likely hypothesis, defining $\Delta W_i = W_{\text{obs}}(j) - W_{\text{obs}}(i) > n$. This means that hypothesis i is n units of ΔW more likely than hypothesis j. In the $K^+\pi^-\pi^+$ analysis reported here, two quantities are taken into account: $\Delta W_\pi = W_{\text{obs}}(K) - W_{\text{obs}}(\pi)$ and $\Delta W_K = W_{\text{obs}}(\pi) - W_{\text{obs}}(K)$. In addition, another Čerenkov cut is defined as the separation of a hypothesis from the minimum one through $\Delta W_{i,\text{min}} = W_{\text{obs}}(i) - W_{\text{obs}}(\text{min}) < n$. This cut determines how likely the i hypothesis is compared to the other hypotheses. For the selection of the samples under analysis, $\Delta W_{\pi,\text{min}}$ and $\Delta W_{K,\text{min}}$ are considered.

- vertex reconstruction:
  a candidate driven vertex algorithm is used. A decay vertex is formed from three reconstructed charged tracks. The momentum of the D candidate is used to intersect other reconstructed tracks to form a production vertex.

Exploiting the informations obtained from the reconstruction process, some quantities, besides the Čerenkov requests, are used to select the sample under study.
The confidence levels (C.L.) of each vertex are required to exceed 1%.
From the vertexing algorithm, the variable L, which is the separation of the primary and secondary vertices, and its associated error σ_L are calculated; the detachment cut requires that L/σ_L be greater than some value.
The two vertices are also required to satisfy isolation conditions. The primary vertex isolation cut (isolation 1) determines the largest confidence level that one of the tracks in the secondary actually comes from the primary. The lower this value, the less likely it is that any of the charm candidate tracks are really associated with the primary vertex. The secondary vertex isolation cut (isolation 2) determines the largest confidence level that a track not in the primary or secondary belongs to the secondary. The lower the value, the more likely it is that the secondary is a "pure" vertex.
Finally the decay vertex is required to be outside of the target material; this cut requires that $\mathrm{Z_{out}}$, defined as $|Z - Z_{\mathrm{tg}}|/\sigma_Z$, be greater than some value $\mathrm{Z_{cut}}$.

3.2 $D^+ \to K^+\pi^-\pi^+$ selection

The doubly suppressed nature of the $D^+ \to K^+\pi^-\pi^+$ decay makes the selection of the sample a very important issue for this analysis. The selection is driven by different requirements: having a proper statistics, obtaining a good signal-to-noise ratio (S/N) (crucial to perform a reliable Dalitz plot analysis) and eliminating possible contaminations from more copious and favored decays. Indeed the background can come from random combinations of particles (combinatorial background) or from charm decays (charm background). The former includes, for instance, directly photoproduced light mesons (ρ, ϕ), combined with any π or K particle; the latter includes contaminations from rich decays when one or two charged particles are Čerenkov misidentified and/or one neutral particle is missing (so-called reflections).

The reflections have to be investigated carefully, especially in view of the Dalitz plot analysis. Generally, to describe the background under the signal, regions close to the signal peak (sidebands) are used, assuming that they provide a good representation of the background in the signal region. The Dalitz plot of mass sidebands is therefore fitted and the resulting fit function is used to describe the shape of the signal background (see Section 5.2 for the detailed discussion). Contributions coming from reflections can be different across the invariant $K^+\pi^-\pi^+$ mass spectrum and therefore can contaminate differently the signal and the sideband Dalitz plots, weakening the assumption about the shape of the background. Therefore the cut selection is performed trying to reach a reasonable compromise between a high yield, a good S/N and negligible level of the reflections, both in the signal and sideband regions.

3.2.1 Optimizing cuts

As starting point the invariant mass spectrum shown in Fig. 3.1 is considered. The loose selection cuts applied are the following:

- Multiplicity of primary vertex > 1
- Hadron trigger
- Z position of the primary vertex (Zprim) < 2 cm
- Z position of the secondary vertex (Zsec) < 2 cm
- C.L. of secondary vertex > 0.01
- $L/\sigma > 8$
- Isolation 1 < 0.01
- Isolation 2 < 0.001
- Out of material (Z_{out}) > 0
- $\Delta W_K > 3$
- $\Delta W_{\pi^-} > 0$
- $\Delta W_{\pi^+} > 0$
- $\Delta W_{K,\min} < 3$
- $\Delta W_{\pi,\min} < 3$

Of course, to minimize the reflections, severe requests on the Čerenkov identification are necessary. Also a tight L/σ cut (> 14) is effective, since it can reject reflections coming from short living mesons, such as D_s and Λ_c, without discarding the major portion of the D^+ signal. From here a detailed study of the selection criteria is performed through cut tree plots, where the number of reconstructed events in the signal region (yield) versus the corresponding S/N is shown for different combinations of the selection cuts. In Fig. 3.2(a) isolation1 and Z_{out} are analyzed; for each value of isolation1 fixed in the set $10^{-1}, 10^{-2}, 10^{-3}, 10^{-4}$, Z_{out} moves from > 0 through > 3. The black line shows the behaviour when Z_{out} is not applied. The importance of the Z_{out} cut is evident: reinforcing this criterion get the S/N increased, maintaining the yield quite constant. This cut reduces the background due to hadronic re-interactions in the target.

In Fig. 3.2(b) ΔW_K and ΔW_{π^-} are shown. ΔW_K varies from > 1 to > 5 along the black line, ΔW_{π^-} from > 0 to > 3 in whole steps and then from > 3.5 to > 5 in half steps, along the colored lines. The effectiveness of the ΔW_K cut is clear looking at the evolution of S/N along the black line.

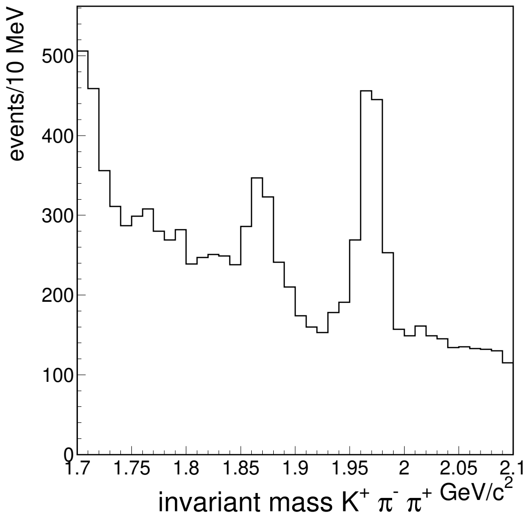

Figure 3.1: Invariant mass spectrum $K^+\pi^-\pi^+$, obtained with a set of loose selection cuts.

L/σ and ΔW_{π^-} and ΔW_{π^+} are studied in Fig. 3.2(c) and 3.2(d), respectively. In both the plots L/σ goes from > 8 to > 14 (black lines) and ΔW_π varies from > 1 to > 3 in whole steps and then from > 3.5 to > 5 in half steps (colored lines).

Analyzing all these cut tree plots, the final set of selection cuts for the DCS sample is chosen as following:

- Multiplicity of primary vertex > 1
- Hadron trigger
- Zprim < 2 cm
- Zsec < 2 cm
- C.L. of secondary vertex > 0.01
- L/$\sigma > 14$
- Isolation 1 < 0.01
- Isolation 2 < 0.001
- Out of material ($\mathrm{Z_{out}}$) > 3
- $\Delta W_K > 4$
- $\Delta W_{\pi^-} > 3.5$

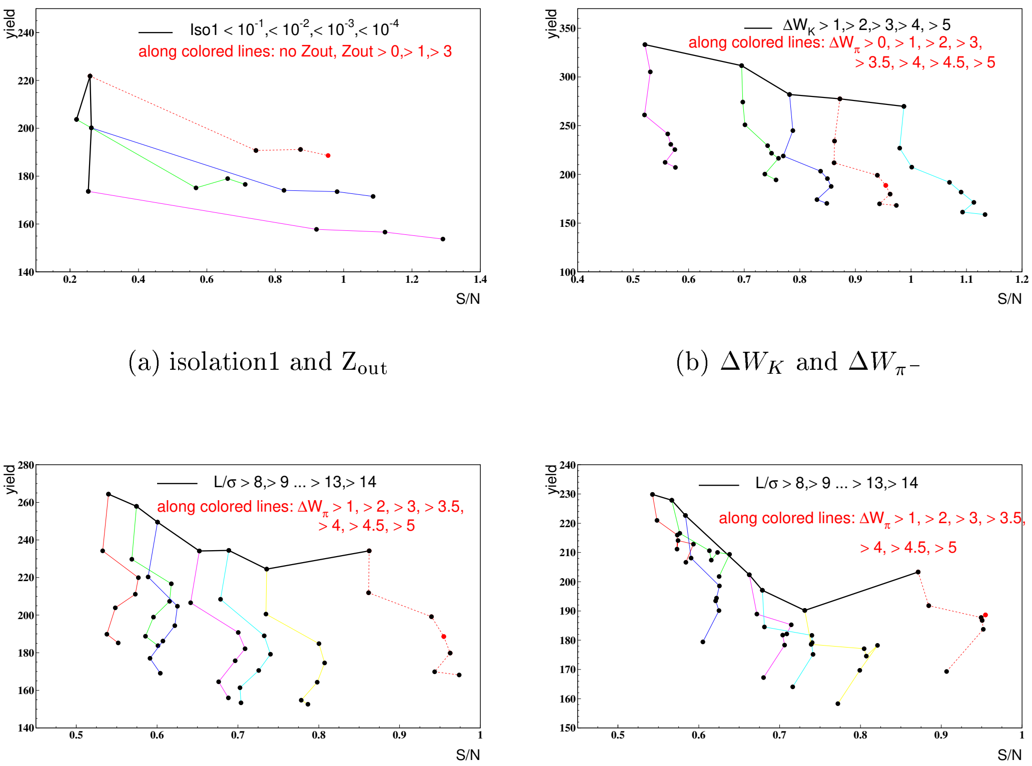

(a) isolation1 and Z_{out}

(b) ΔW_K and ΔW_{π^-}

(c) L/σ and ΔW_{π^-}

(d) L/σ andΔW_{π^+}

Figure 3.2: Yield versus S/N for different combinations of selection cuts. In (a) isolation1 and Z_{out} are moved, in (b) ΔW_K and ΔW_{π^-}, in (c) and in (d) L/σ with ΔW_{π^-} and ΔW_{π^+}, respectively. The red point corresponds to the criteria chosen for the sample selection.

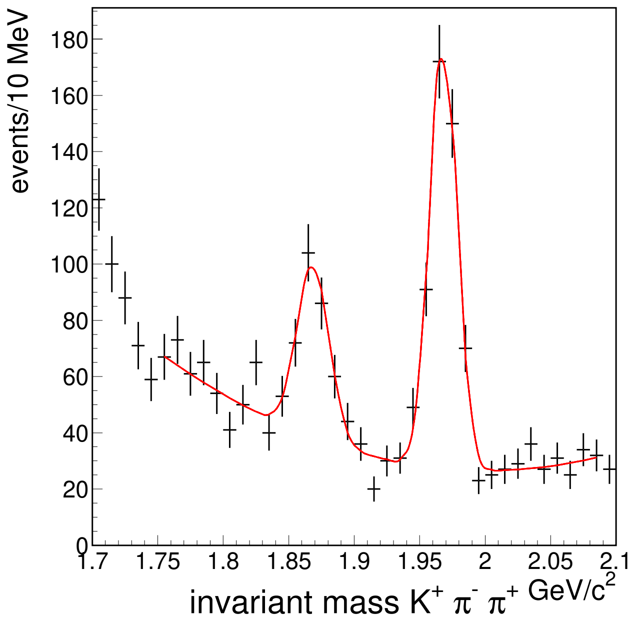

Figure 3.3: Invariant mass spectrum $K^+\pi^-\pi^+$, obtained with the final set of cuts optimized for the D^+ sample. The result of the fit is also shown.

- $\Delta W_{\pi+} > 3.5$
- $\Delta W_{K,\mathrm{min}} < 3$
- $\Delta W_{\pi,\mathrm{min}} < 3$

The resulting invariant mass spectrum is shown in Fig. 3.3. The fit to the $K^+\pi^-\pi^+$ mass distribution starts from the 1.75 GeV/c^2 energy threshold since a Monte Carlo (MC) $c\bar{c}$ generation shows that the region below is dominated by the partial reconstruction of multi-body charm channels where neutrals are missing. The fit is performed with two Gaussian functions for the signals and a second order polynomial for the background. Centroid and width are found to be 1.869 ± 0.002 GeV/c^2 and 0.012 ± 0.002 GeV/c^2, in good agreement with the MC predictions. The signal yield consists of 189 ± 24 events and the S/N is 1.0 ± 0.1.

These studies about the selection criteria allowed to find a set of cuts which provided yield and S/N proper to perform a reliable Dalitz plot analysis. Since, as already said, reflections from charm decays can complicate the analysis, a detailed investigation of the possible contaminations and structures, survived to the selection requests, has to be performed. Initially a qualitative study is carried out, to know the shape of the reflections across the invariant mass spectrum and over the Dalitz plot; then an evaluation of the number of expected reflected events is done, to see the possible impact of these contaminations on the analysis.

3.2.2 Study of reflections

A detail MC study is performed to evaluate the possible contaminations and structures induced by reflections both in the signal and in the sideband regions. The considered sources of charm background are:

1. D^+ and D_s^+ three-body hadronic decays, where one or two particles are misidentified:

   - $D^+ \to K^-K^+\pi^+$
   - $D_s^+ \to K^-K^+\pi^+$
   - $D^+ \to \pi^+\pi^-\pi^+$
   - $D^+ \to K^-\pi^+\pi^+$

2. Four-body hadronic and semileptonic decays, where charged particles are misidentified and neutrals are missing:

   - $D^+ \to \overline{K}^{*0}\mu^+\nu$
   - $D^+ \to K^-\pi^+\pi^+\pi^0$
   - $D_s^+ \to \phi\mu^+\nu$

For each of these channels about 5 millions of MC events are generated and then reconstructed, through an analysis program, as $K^+\pi^-\pi^+$ events. The MC code generates events of the wanted decay, along with events coming from the $\bar{c}$ channel. The $\bar{c}$ can decay in one of the channels that are listed in the MC code, according to their branching ratio. For this study the branching ratio of the DCSD is set to zero to be sure that the reconstructed events correspond only to misidentified particles and no $D^+ \to K^+\pi^-\pi^+$ tracks are taken into account.

To investigate the shape of each reflection across the $K^+\pi^-\pi^+$ invariant mass spectrum, only few and loose selection cuts are first applied to the MC samples: multiplicity of primary vertex > 1, L$/\sigma > 5$ and $\Delta W_K > 0.5$. In Fig. 3.4 the resulting distributions are shown. The decays where one particle is misidentified ($D^+ \to K^-K^+\pi^+$ Fig. 3.4(a), $D_s^+ \to K^-K^+\pi^+$ Fig. 3.4(b) and $D^+ \to \pi^+\pi^-\pi^+$ Fig. 3.4(c)) have an asymmetric behaviour: these reflections are localized in particular energy regions and they can induced different structures in the signal and sideband areas. The remaining decays where two particles are misidentified ($D^+ \to K^-\pi^+\pi^+$ Fig. 3.4(d), $D^+ \to \overline{K}^{*0}\mu^+\nu$ Fig. 3.4(e), $D^+ \to K^-\pi^+\pi^+\pi^0$ Fig. 3.4(f) and $D_s^+ \to \phi\mu^+\nu$ Fig. 3.4(g)) are smoothly distributed across the invariant mass spectrum and they should not induced different structures in different energy regions.

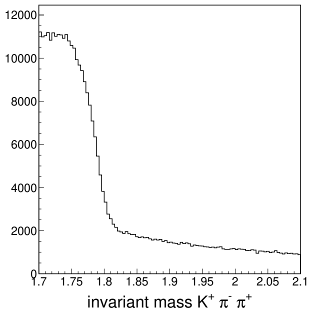

(a) MC $D^+ \to K^- K^+ \pi^+$

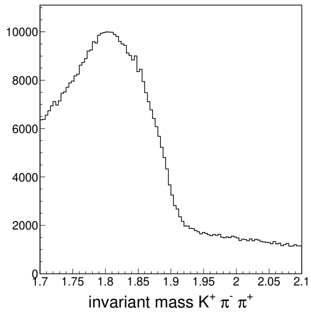

(b) MC $D_s^+ \to K^- K^+ \pi^+$

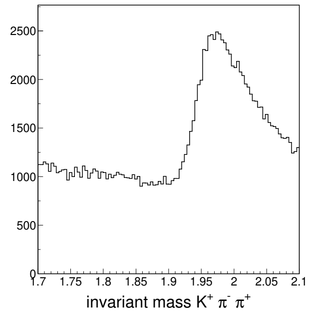

(c) MC $D^+ \to \pi^+ \pi^- \pi^+$

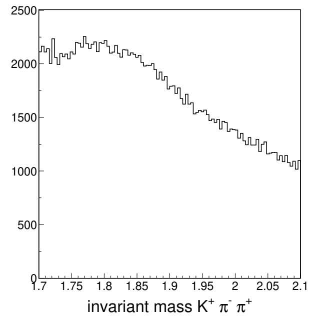

(d) MC $D^+ \to K^- \pi^+ \pi^+$

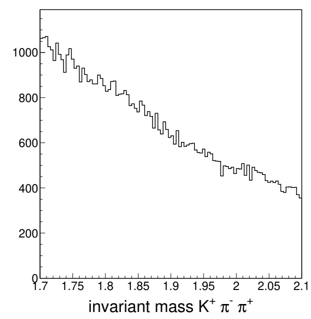

(e) MC $D^+ \to K^- \pi^+ \mu^+ \nu$

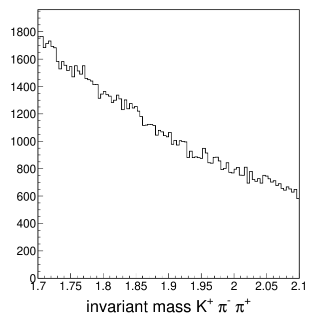

(f) MC $D^+ \to K^- \pi^+ \pi^+ \pi^0$

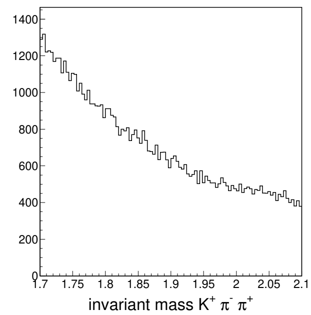

(g) MC $D_s^+ \to K^- K^+ \mu^+ \nu$

Figure 3.4: Shapes of the possible reflections in the $K^+\pi^-\pi^+$ invariant mass distribution, generated by the channels cited in the captions. These spectra are obtained with loose selection cuts, to know the shape of the structures.

Also Λ_c^+ decays ($\Lambda_c^+ \to pK^-\pi^+$, $\Lambda_c^+ \to p\pi^-\pi^+$ and $\Lambda_c^+ \to pK^-K^+$) can induce reflections in the $D^+ \to K^+\pi^-\pi^+$ sample, but these contributions are expected to be small. Nevertheless, to be sure that no contaminations from these channels are present, the particle assignments in the $K^+\pi^-\pi^+$ data sample are changed to look for the corresponding mass peaks. For instance, the events in the signal region of the $K^+\pi^-\pi^+$ invariant mass spectrum are selected and the proton mass is assigned to the K^+ particle; then the $p\pi^-\pi^+$ invariant mass spectrum is reconstructed to looking for a mass peak corresponding to the Λ_c^+ mass. For all the decays under study no visible peaks are found; these channels do not give any problem for the $D^+ \to K^+\pi^-\pi^+$ analysis.

The next step is to study how structures can be induced by the reflections over the $D^+ \to K^+\pi^-\pi^+$ Dalitz plots of signal and sideband events. The signal region is defined within $\pm 2\sigma$ of the D^+ mass peak. Several possible sidebands are analyzed; they are three left sidebands, from -3σ to -5σ, from -4σ to -6σ and from -5σ to -7σ, and two right sidebands, from $+3\sigma$ to $+5\sigma$ and from $+4\sigma$ to $+6\sigma$. The region from $+5\sigma$ to $+7\sigma$ is not considered, since it overlaps to the $D_s^+ \to K^+\pi^-\pi^+$ signal. To perform this study, the generated MC events are represented over the Dalitz plot as if they were $D^+ \to K^+\pi^-\pi^+$ events; again loose selection cuts are applied.

As already said, the main concern is to have a different behaviour of the reflections in different energy regions. A clear and instructive example is the $D_s^+ \to K^-K^+\pi^+$ decay. This channel is highly structured, as it is easily visible in Fig. 3.5(a), where the Dalitz plot of the data is shown; the dominant resonances are $\phi(1020)$ (vertical band) and $K^*(892)$ (horizontal band). When the $D_s^+ \to K^-K^+\pi^+$ MC events are reconstructed as $D^+ \to K^+\pi^-\pi^+$, the previous resonances are reflected and they appear over the Dalitz plot under study (Fig. 3.5(b)-3.5(g)). These structures lie only over particular plots because of the shape of the reflection across the invariant mass spectrum (Fig. 3.4(b)).

The same behaviour is present in the $D^+ \to K^-K^+\pi^+$ decay, which is dominated by $\phi(1020)$ and $K^*(892)$ as well.

All the other MC studies give quite flat distributions.

At this point it is necessary to evaluate the number of reflected events, expected in the $D^+ \to K^+\pi^-\pi^+$ sample, which survived the selection cuts. Let us consider a generic reflection channel $D \to X$, among those listed at the beginning of section 3.2.2; from the MC generation the number of reflected events $N(\mathrm{Refl_{MC}})$ with respect to the generated events $N(\mathrm{Gen_{MC}})_{D\to X}$ is available and the estimate of the expected events in the FOCUS data $N(\mathrm{Refl_{FOCUS}})$ can be obtained through a simple proportional relation:

$$N(\mathrm{Refl_{MC}}) : N(\mathrm{Gen_{MC}})_{D\to X} = N(\mathrm{Refl_{FOCUS}}) : N(\mathrm{Gen_{FOCUS}})_{D\to X} \tag{3.1}$$

$N(\mathrm{Gen_{FOCUS}})_{D\to X}$ is the number of the $D \to X$ produced events in the experiment, before the reconstruction process. This quantity can be calculated, once the total

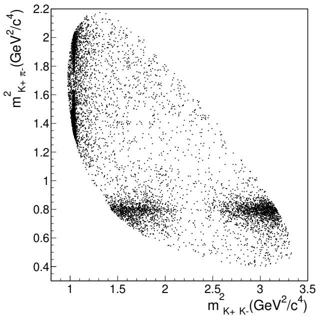

(a) $D_s^+ \to K^- K^+ \pi^+$ data.

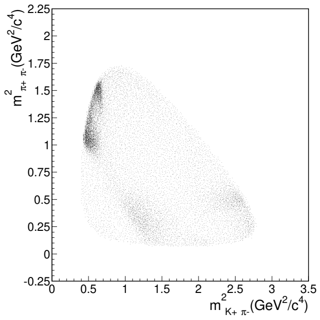

(b) Sideband from -7σ to -5σ

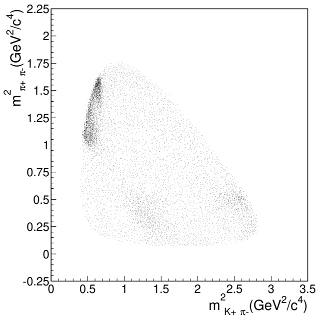

(c) Sideband from -6σ to -4σ

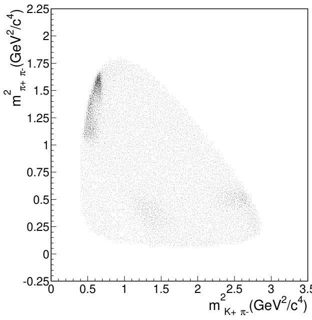

(d) Sideband from -5σ to -3σ

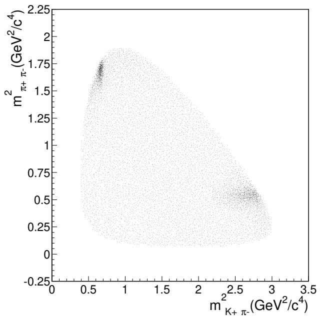

(e) Signal region

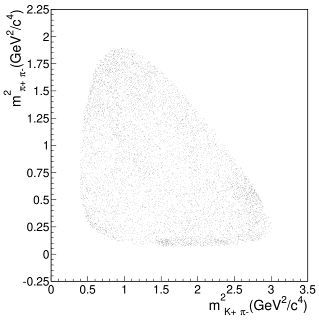

(f) Sideband from $+4\sigma$ to $+6\sigma$

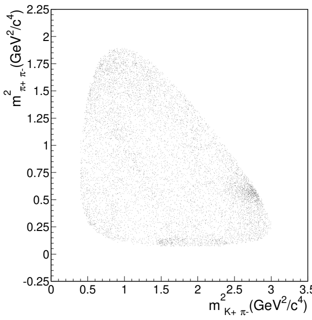

(g) Sideband from $+3\sigma$ to $+5\sigma$

Figure 3.5: $D_s^+ \to K^- K^+ \pi^+$ reflections. In (a) the $D_s^+ \to K^- K^+ \pi^+$ data are shown; from (b) to (g) MC $D_s^+ \to K^- K^+ \pi^+$ events reconstructed as $D^+ \to K^+ \pi^- \pi^+$ are represented.

number of D generated in FOCUS $N(D_{\rm tot})$ is known, through the definition of branching ratio:

$$Br(D \to X) = \frac{N(\mathrm{Gen}_{\mathrm{FOCUS}})_{D\to X}}{N(D_{\rm tot})} \tag{3.2}$$

If the reflection mode comes from a D_s decay, the total number of D_s generated in FOCUS $N(D_{s-\rm tot})$ is necessary to obtain the evaluation of the reflected events. To have an estimate of $N(D_{\rm tot})$ and $N(D_{s-\rm tot})$, two normalization channels are chosen among the most copious decays: the $D^+ \to K^-\pi^+\pi^+$ and the $D_s^+ \to K^+K^-\pi^+$.

1. $D^+ \to K^-\pi^+\pi^+$

Loose selection cuts are applied to have a high statistic sample. They are:

- Multiplicity of primary vertex > 1
- Hadron trigger
- Zprim < 2 cm
- Zsec < 2 cm
- C.L. of secondary vertex > 0.01
- L/$\sigma > 10$
- Isolation 1 < 0.2
- Isolation 2 < 0.001
- $\Delta W_K > 1$
- $\Delta W_\pi > 1$
- $\Delta W_{K,\rm min} < 3$
- $\Delta W_{\pi,\rm min} < 3$

In Fig. 3.6 the $K^-\pi^+\pi^+$ invariant mass spectra for data and MC are shown. The fits are performed with a Gaussian function for the signals, a first degree polynomial for the data background and a constant for the MC background. The reconstructed efficiency ε is defined as:

$$\varepsilon = \frac{Yield(D^+ \to K^-\pi^+\pi^+)}{N(\mathrm{Gen})_{D^+\to K^-\pi^+\pi^+}} \tag{3.3}$$

This equation has to be valid both for data and MC events. From the MC simulation the Yield$(D^+ \to K^-\pi^+\pi^+)_{MC}$ and the generated events $N(\mathrm{Gen}_{MC})_{D^+\to K^-\pi^+\pi^+}$ are

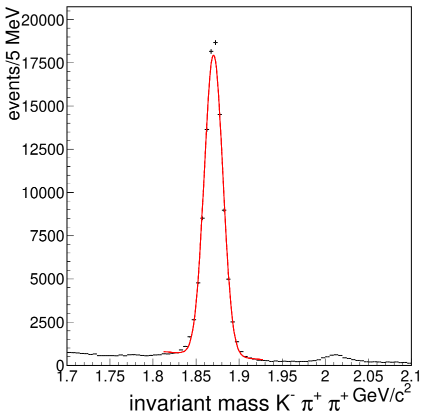

(a) data

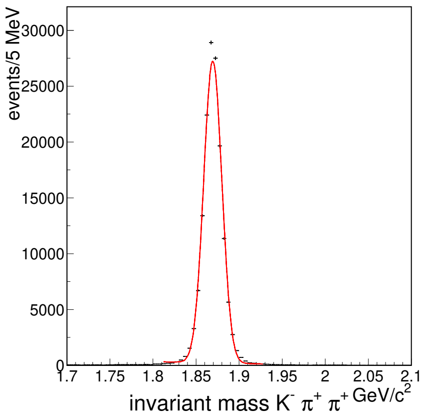

(b) MC

Figure 3.6: Data and MC $K^-\pi^+\pi^+$ invariant mass spectra. The $D^+ \to K^-\pi^+\pi^+$ is used as normalization channel in the evaluation of the reflections.

available; therefore ε can be calculated and consequently $N(\mathrm{Gen}_{\mathrm{FOCUS}})_{D^+\to K^-\pi^+\pi^+}$ (the so-called efficiency corrected yield) is obtained as:

$$N(\mathrm{Gen}_{\mathrm{FOCUS}})_{D^+\to K^-\pi^+\pi^+} = \frac{Yield(D^+ \to K^-\pi^+\pi^+)_{FOCUS}}{\varepsilon} \tag{3.4}$$

From the equation 3.2 and from the measurement of the branching ratio reported in the PDG [5] the total number of D can be evaluated as:

$$N(D_{\mathrm{tot}}) = \frac{N(\mathrm{Gen}_{\mathrm{FOCUS}})_{D^+\to K^-\pi^+\pi^+}}{Br(D^+ \to K^-\pi^+\pi^+)} \tag{3.5}$$

2. $D_s^+ \to K^+K^-\pi^+$

Also in this case the selection criteria are chosen in order to have a high statistic sample. They are:

- Multiplicity of primary vertex > 1
- Hadron trigger
- Zprim < 2 cm
- Zsec < 2 cm

	$\text{Yield}_{\text{FOCUS}}$	ε %
$D^+ \to K^-\pi^+\pi^+$	94041 ± 329	2.564 ± 0.007
$D_s^+ \to K^+K^-\pi^+$	10385 ± 143	1.739 ± 0.006

Table 3.1: Data yields and reconstructed efficiencies for the two normalization channels.

- C.L. of secondary vertex > 0.01
- $\text{L}/\sigma > 5$
- Isolation 1 < 0.2
- Isolation 2 < 0.001
- Out of material (Z_{out}) > 0
- $\Delta W_K > 1$
- $\Delta W_{\pi,\min} < 2$

Kinematic cuts are also applied to remove the reflections from the $D^+ \to K^-\pi^+\pi^+$ and from the $D^{*+} \to D^0\pi^+$, followed by the D^0 decay to K^-K^+. In this case, since the D^{*+} decays via strong interaction, the primary and secondary vertices are so close that the resolution of the spectrometer is not sufficient to separate them; it is possible that the reconstruction algorithm identifies a wrong production vertex and uses the D^{*+} decay as decay vertex. The corresponding invariant mass spectra for data and MC are shown in Fig. 3.7. The fits are performed with Gaussian functions for the signals and with a second order polynomial and a constant for the data and MC backgrounds, respectively. Following the previous procedure, the reconstructed efficiency is calculated and the total number of produced D_s in FOCUS is:

$$N(D_{s-\text{tot}}) = \frac{N(\text{Gen}_{\text{FOCUS}})_{D_s^+ \to K^+K^-\pi^+}}{Br(D_s^+ \to K^+K^-\pi^+)} \tag{3.6}$$

In Table 3.1 the data yields and the efficiencies for both the normalization channels are reported. The total number of D and D_s produced in FOCUS are estimated to be about 40 and 13 millions, respectively.

Using these results, the number of expected reflected events for each channel, in different regions of the mass spectrum, can be evaluated from Eq. 3.1 and Eq. 3.2. The obtained values are summarized in Table 3.2(a) for the signal region and in Table 3.2(b) for the sideband regions. In the signal region the major contributions come

decay channel	reflected events
$D_s^+ \to K^+K^-\pi^+$	11.4 ± 3.3
$D^+ \to K^-\pi^+\pi^+$	12.5 ± 3.0
$D^+ \to K^+K^-\pi^+$	0.8 ± 0.2
$D^+ \to \pi^+\pi^-\pi^+$	0.6 ± 0.1
$D^+ \to \overline{K}^{*0}\mu^+\nu$	1.9 ± 0.7
$D_s^+ \to \phi\mu^+\nu$	0.2 ± 0.1
$D^+ \to K^-\pi^+\pi^+\pi^0$	7.3 ± 2.1

(a) signal region

decay channel	reflected events				
	right SB		left SB		
	$3-5\sigma$	$4-6\sigma$	$3-5\sigma$	$4-6\sigma$	$5-7\sigma$
$D_s^+ \to K^+K^-\pi^+$	0.9 ± 0.4	1.0 ± 0.4	8.6 ± 2.5	9.3 ± 2.7	9.3 ± 2.7
$D^+ \to K^-\pi^+\pi^+$	5.9 ± 2.0	8.6 ± 2.4	5.9 ± 2.0	7.9 ± 2.3	7.2 ± 2.2
$D^+ \to K^+K^-\pi^+$	0.5 ± 0.2	0.4 ± 0.2	0.7 ± 0.2	1.1 ± 0.3	2.1 ± 0.4
$D^+ \to \pi^+\pi^-\pi^+$	0.4 ± 0.1	0.7 ± 0.1	0.1 ± 0.1	0.2 ± 0.1	0.2 ± 0.1
$D^+ \to \overline{K}^{*0}\mu^+\nu$	1.6 ± 0.7	0.8 ± 0.5	1.3 ± 0.6	1.9 ± 0.7	1.1 ± 0.5
$D_s^+ \to \phi\mu^+\nu$	0.1 ± 0.1	0.1 ± 0.1	0.2 ± 0.1	0.2 ± 0.1	0.3 ± 0.1
$D^+ \to K^-\pi^+\pi^+\pi^0$	2.8 ± 1.3	2.8 ± 1.3	5.6 ± 1.8	5.0 ± 1.7	3.9 ± 1.5

(b) sideband regions

Table 3.2: Estimate of the MC reflected events in the signal region and in different possible sideband regions.

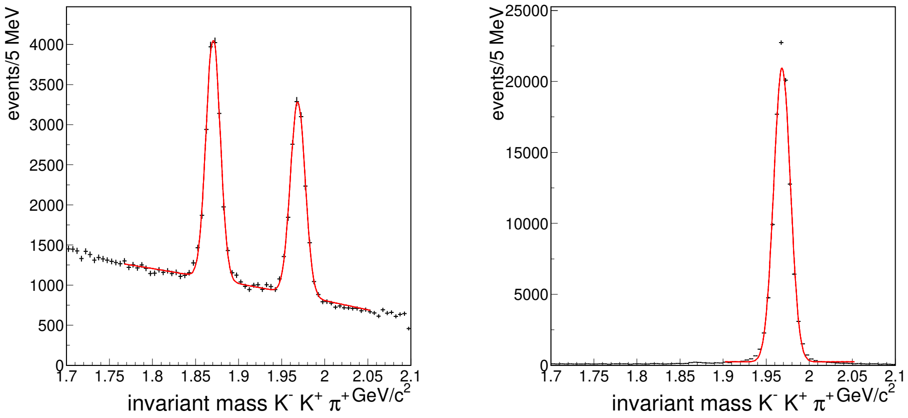

(a) data (b) MC

Figure 3.7: Data and MC $K^+K^-\pi^+$ invariant mass spectra. The $D_s^+ \to K^+K^-\pi^+$ is used as normalization channel in the evaluation of the reflections.

from $D_s^+ \to K^+K^-\pi^+$, $D^+ \to K^-\pi^+\pi^+$ and $D^+ \to K^-\pi^+\pi^+\pi^0$. The same channels are dominant in the left sidebands, while in the right sidebands the $D^+ \to K^-\pi^+\pi^+$ is dominant. In Fig. 3.8 the comparison of these three contributions across the invariant mass spectrum is represented. The total contribution coming from all the survived reflected events is shown in Fig. 3.9, where the $K^+\pi^-\pi^+$ selected sample is plotted. The reflected events are smoothly distributed across the invariant mass spectrum and are thus properly accounted for by the background polynomial fitting function.

Table 3.2 shows that the number of reflected events in every studied region is quite small. Moreover no residual structures, coming from the channels listed at the beginning of Section 3.2.2, are evident over the signal and sideband Dalitz plots of the MC reflected events. A further check is performed through a $c\bar{c}$ event generation ($\sim$ 40 millions); again, with this more complete simulation, no residual structures are evident over the Dalitz plots. It can be reasonably assumed that the reflections in the sidebands adequately represent the reflections in the signal region.

3.3 $D_s^+ \to K^+\pi^-\pi^+$ selection

The $D_s^+ \to K^+\pi^-\pi^+$ selection is performed, as for D^+, to have proper statistics, a good S/N and to try to eliminate possible contaminations from reflections; also for this decay the sample choice is a crucial issue. Since this channel is a singly Cabibbo suppressed decay, a higher statistics and less severe contributions from the reflections are expected.

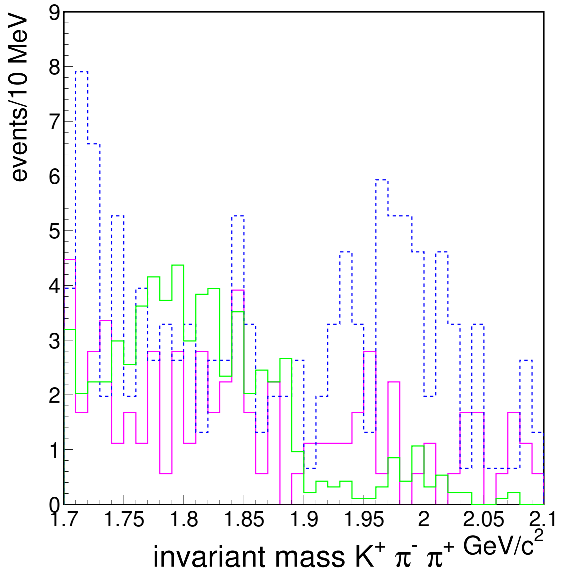

Figure 3.8: Distributions of the MC expected reflected events for the more important contributions in the D^+ analysis; in blue the $D^+ \to K^-\pi^+\pi^+$, in purple the $D^+ \to K^-\pi^+\pi^+\pi^0$ and in green the $D_s^+ \to K^+K^-\pi^+$.

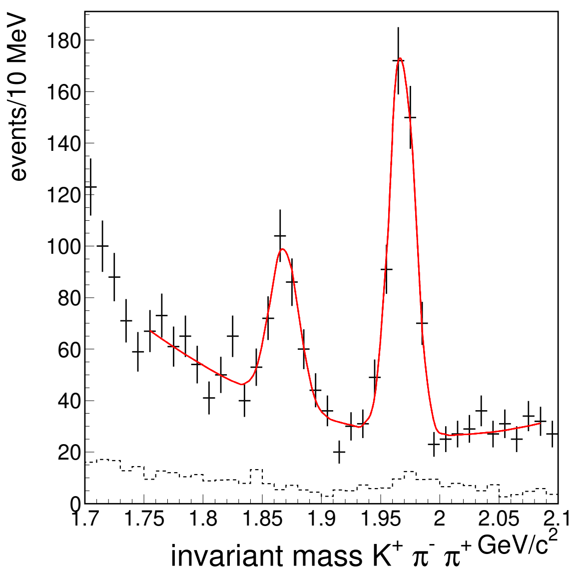

Figure 3.9: Invariant mass spectrum $K^+\pi^-\pi^+$, obtained with the final selection criteria, along with the distribution of the residual reflected events expected from MC (dotted curves). The result of the fit is also shown.

3.3.1 Optimizing cuts

The starting point is the D_s^+ sample selected with the optimized cuts for D^+ (Fig. 3.9); the fit returns a yield of about 400 events and a S/N equal to 3.3. The idea is to release some cuts in order to increase the statistics, maintaining a good S/N (greater than 2). Also in this case a detailed study of the cuts is carried out, comparing the different yields and the corresponding S/N. Of course L/σ is a criterion that has to be released, since the D_s^+ meson has a shorter lifetime than the D^+. Moreover, since the reflections should be less important, looser requests on the Čerenkov identification could be possible.

Using the same cut variation ranges as for the D^+, different cut tree plots are analyzed. In Fig. 3.10(a) the moved cuts are isolation1 and Z_{out}; the behaviour of Z_{out} is similar to those observed for the D^+. In Fig. 3.10(b) ΔW_K and ΔW_{π^-} are represented; in Fig. 3.10(c) and 3.10(d) L/σ together with ΔW_{π^-} and ΔW_{π^+} are changed, respectively.

Looking at all these cut tree plots, the final set of selection cuts for the SCS sample is chosen as following:

- Multiplicity of primary vertex > 1
- Hadron trigger
- Zprim < 2 cm
- Zsec < 2 cm
- C.L. of secondary vertex > 0.01
- L/$\sigma > 10$
- Isolation 1 < 0.01
- Isolation 2 < 0.001
- Out of material (Z_{out}) > 3
- $\Delta W_K > 4$
- $\Delta W\pi^- > 2$
- $\Delta W\pi^+ > 1$
- $\Delta W_{K,\min} < 3$
- $\Delta W_{\pi,\min} < 3$

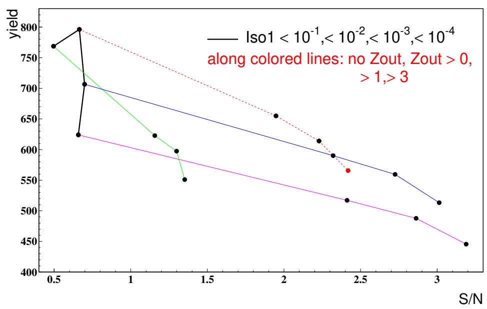

(a) isolation1 and Z_{out}

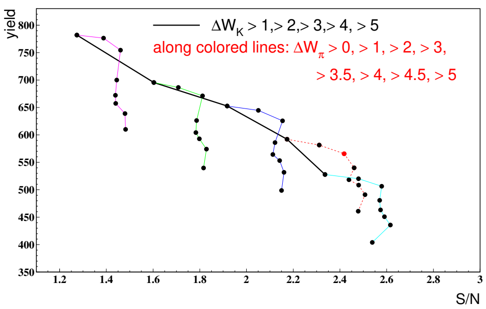

(b) ΔW_K and ΔW_{π^-}

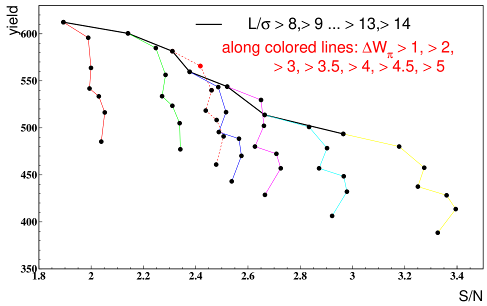

(c) L/σ and ΔW_{π^-}

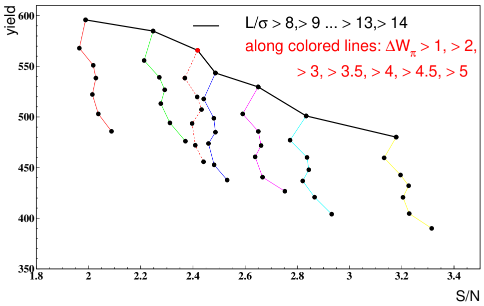

(d) L/σ and ΔW_{π^+}

Figure 3.10: Yield versus S/N for different combinations of selection cuts. In (a) isolation1 and Z_{out} are moved, in (b) ΔW_K and ΔW_{π^-}, in (c) and in (d) L/σ with ΔW_{π^-} and ΔW_{π^+}, respectively. The red point corresponds to the criteria chosen for the sample selection.

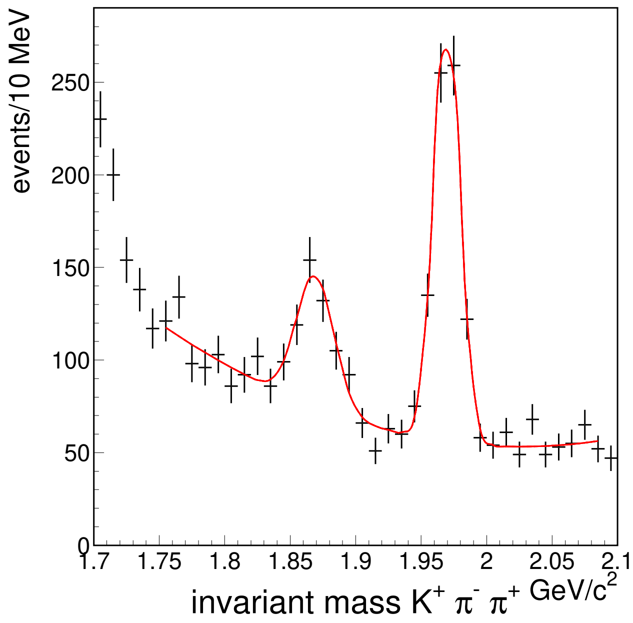

Figure 3.11: Invariant mass spectrum $K^+\pi^-\pi^+$, obtained with the final set of cuts optimized for the D_s^+ sample. The result of the fit is also shown.

The corresponding invariant mass spectrum is shown in Fig. 3.11. The fit, performed with two Gaussian functions for the signals and a second order polynomial for the background, returns a centroid of 1.970 ± 0.001 GeV/c^2 and a width of 0.010 ± 0.001 GeV/c^2, in good agreement with the MC predictions. The signal yield consists of 567 ± 31 events and the S/N is 2.4 ± 0.4.

3.3.2 Study of reflections

Also for the D_s^+ a detailed study of the effects of the possible reflections is carried out. The sources of charm background are expected to be the same as for D^+ and are listed at the beginning of section 3.2.2. As for the D^+, the branching ratio of the SCSD is set to zero in the MC code, to ensure that the MC events reconstructed as $D_s^+ \to K^+\pi^-\pi^+$ do not include tracks of this decay.

The shape of each reflection across the invariant mass spectrum $K^+\pi^-\pi^+$ is shown in Fig. 3.4. Now there is only a channel, the $D^+ \to \pi^+\pi^-\pi^+$ (Fig. 3.4(c)), which has an asymmetric structure in the D_s region. The right sidebands considered are three: from $+3\sigma$ to $+5\sigma$, from $+4\sigma$ to $+6\sigma$ and from $+5\sigma$ to $+7\sigma$; the left sidebands are two: from -3σ to -5σ and from -4σ to -6σ. The zone from -5σ to

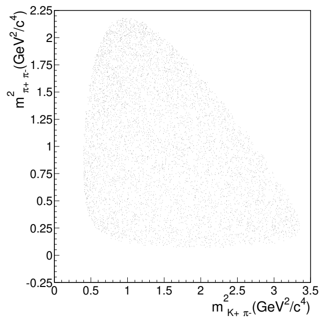

(a) Sideband from $+5\sigma$ to $+7\sigma$

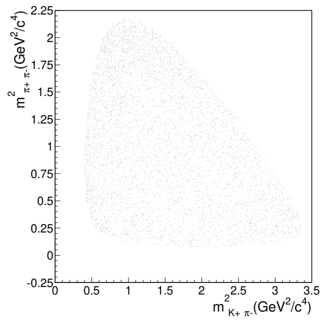

(b) Sideband from $+4\sigma$ to $+6\sigma$

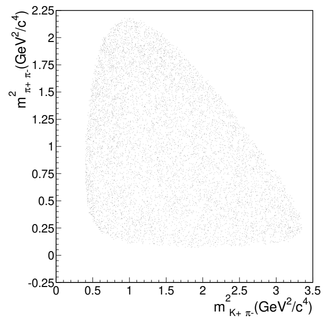

(c) Sideband from $+3\sigma$ to $+5\sigma$

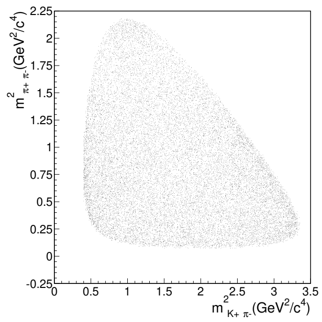

(d) Signal region

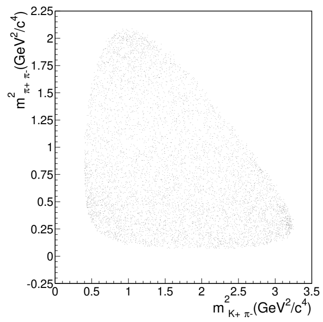

(e) Sideband from -5σ to -3σ

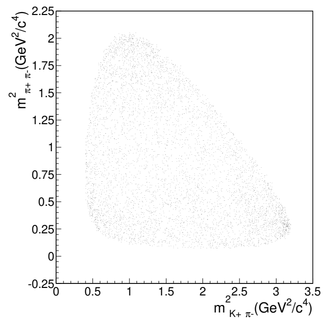

(f) Sideband from -6σ to -4σ

Figure 3.12: $D^+ \to \pi^+\pi^-\pi^+$ MC events, reconstructed as $D_s^+ \to K^+\pi^-\pi^+$.

-7σ overlaps the D^+ signal region and it is not taken into account.

As for the D^+, a qualitative study is performed with other possible reflection channels. They are the same decays of the Λ_c analyzed for the D^+, plus the D^0 decays into $\pi^+\pi^-$ and $K^-\pi^+$ and the $D^* \to D_0\pi^+ \to (K^-\pi^+)\pi^+$ mode. For all these channels no mass peaks corresponding to the decay particle are found.

Then the MC events belonging to different regions are represented over the Dalitz plot as if they were $D_s^+ \to K^+\pi^-\pi^+$ events. Unlike the D^+ case, now there are not evident reflected structures and all the Dalitz plots have quite flat event distributions. In Fig. 3.12 the example of the $D^+ \to \pi^+\pi^-\pi^+$ is reported.

Also for the D_s^+ the evaluation of the expected events is carried out, having

decay channel	reflected events
$D_s^+ \to K^+K^-\pi^+$	2.8 ± 0.9
$D^+ \to K^-\pi^+\pi^+$	29.6 ± 4.8
$D^+ \to K^+K^-\pi^+$	1.5 ± 0.3
$D^+ \to \pi^+\pi^-\pi^+$	8.7 ± 0.7
$D^+ \to \overline{K}^{*0}\mu^+\nu$	6.2 ± 1.3
$D_s^+ \to \phi\mu^+\nu$	0.4 ± 0.2
$D^+ \to K^-\pi^+\pi^+\pi^0$	8.4 ± 2.2

(a) signal region

decay channel	reflected events				
	right SB			left SB	
	$3-5\sigma$	$4-6\sigma$	$5-7\sigma$	$3-5\sigma$	$4-6\sigma$
$D_s^+ \to K^+K^-\pi^+$	1.1 ± 0.4	1.1 ± 0.4	1.3 ± 0.5	1.1 ± 0.4	1.8 ± 0.7
$D^+ \to K^-\pi^+\pi^+$	13.2 ± 3.1	11.9 ± 2.9	6.6 ± 2.1	13.8 ± 3.2	10.5 ± 2.7
$D^+ \to K^+K^-\pi^+$	0.4 ± 0.2	0.3 ± 0.1	0.3 ± 0.1	0.6 ± 0.2	0.8 ± 0.2
$D^+ \to \pi^+\pi^-\pi^+$	6.2 ± 0.6	5.3 ± 0.5	4.7 ± 0.5	0.9 ± 0.2	0.5 ± 0.1
$D^+ \to \overline{K}^{*0}\mu^+\nu$	0.8 ± 0.5	1.1 ± 0.5	1.9 ± 0.7	1.6 ± 0.7	1.6 ± 0.7
$D_s^+ \to \phi\mu^+\nu$	0.2 ± 0.1	0.1 ± 0.1	0.2 ± 0.1	0.3 ± 0.1	0.2 ± 0.1
$D^+ \to K^-\pi^+\pi^+\pi^0$	3.9 ± 1.5	3.9 ± 1.5	3.9 ± 1.5	5.0 ± 1.7	3.4 ± 1.4

(b) sideband regions

Table 3.3: Estimate of the MC reflected events in the signal region and in different possible sideband regions.

already calculated the total number of D and D_s produced in FOCUS. The results are reported in Table 3.3. The prevalent contribution both in the signal and sideband regions comes from the $D^+ \to K^-\pi^+\pi^+$. There are not much than 10 events from the $D^+ \to \pi^+\pi^-\pi^+$ in the signal region and in the right sidebands and a few events from $D^+ \to K^-\pi^+\pi^+\pi^0$ in all the zones. These three reflections are shown across the invariant mass spectrum in Fig. 3.13. All the survived reflected events are summed and the total contribution is shown in Fig. 3.14. As for the D^+, the reflected events are smoothly distributed across the $K^+\pi^-\pi^+$ spectrum and the background polynomial fitting function is able to properly account for them.

Also for the D_s^+ it is verified that no reflected structures, coming from the MC generated channels listed at the beginning of Section 3.2.2 and from $c\bar{c}$ generation, are evident over the Dalitz plots of signal and sideband events.

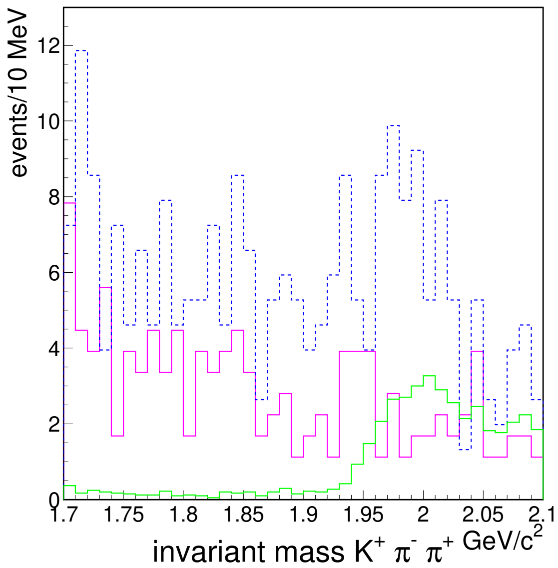

Figure 3.13: Distributions of the expected reflected events for the more important contributions in the D_s^+ analysis; in blue the $D^+ \to K^-\pi^+\pi^+$, in purple the $D^+ \to K^-\pi^+\pi^+\pi^0$ and in green the $D^+ \to \pi^+\pi^-\pi^+$.

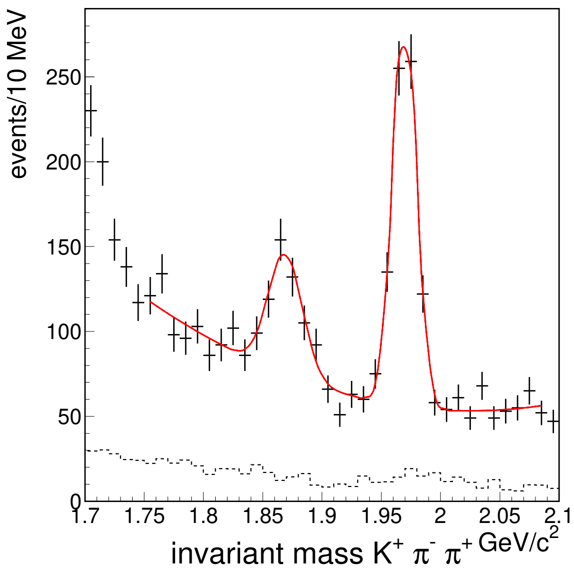

Figure 3.14: Invariant mass spectrum $K^+\pi^-\pi^+$, obtained with the final selection criteria, along with the distribution of the residual reflected events expected from MC (dotted curves). The result of the fit is also shown.

3.4 Conclusions

Tight cuts have been applied to the D^+ and $D_s^+ \to K^+\pi^-\pi^+$ decays, in order to eliminate the reflections. They have provided yield and S/N adequate to perform both branching ratio and Dalitz plot analyses; in particular for the D^+ a sample of 189 ± 24 events with a S/N equal to 1.0 ± 0.1 has been selected, for the D_s^+ a sample of 567 ± 31 events with S/N equal to 2.4 ± 0.4. A thorough investigation of the effects of the reflections has been carried out to verify that any residual contribution is small and no residual structures are present, to compromise the background assumption and parametrization. Anyway, to verify that the selected sets of cuts do not introduce bias in the final results, a systematic error is evaluated by performing the analysis on samples selected with different cut values (Section 4.1.1 and 4.2.1).

Chapter 4

Branching ratio measurements

The branching ratio of a certain channel is defined as (Eq. 3.2):

$$Br(D \to X) = \frac{N(\text{Gen}_{\text{FOCUS}})_{D\to X}}{N(D_{\text{tot}})} \tag{4.1}$$

The measurement of a decay rate is usually made with respect to a normalization channel $D \to X'$:

$$Br\left(\frac{D \to X}{D \to X'}\right) = \frac{\Gamma(D \to X)}{\Gamma(D \to X')} = \frac{N(\text{Gen}_{\text{FOCUS}})_{D\to X}}{N(\text{Gen}_{\text{FOCUS}})_{D\to X'}} \tag{4.2}$$

The normalization channel is chosen among high statistics decays with the same particles (where possible) as the channel under study. In this way statistical errors can be reduced and, choosing the same selection cuts for the two decays in the ratio, possible systematics effects, due to particular selection criteria, are canceled. Using the reconstruction efficiencies ε and the yields of the two samples, the relative branching ratio can be obtained as the ratio of the two efficiency corrected yields (Eq. 3.4):

$$BR\left(\frac{D \to X}{D \to X'}\right) = \frac{Y(D \to X)}{\varepsilon(D \to X)} \cdot \frac{\varepsilon(D \to X')}{Y(D \to X')} \tag{4.3}$$

To obtain the efficiencies necessary for the evaluation of the branching ratios a fully coherent MC generation has been used. For the channels under study the resonant substructure comes from the Dalitz plot analysis presented in this thesis; for the normalization modes results, coming from previous Dalitz analysis performed in the E687 collaboration, are used.

4.1 $\Gamma(D^+ \to K^+\pi^-\pi^+)/\Gamma(D^+ \to K^-\pi^+\pi^+)$

The DCS $D^+ \to K^+\pi^-\pi^+$ decay fraction is evaluated with respect to the CF $D^+ \to K^-\pi^+\pi^+$ mode. The normalization channel is selected with the same set of cuts as for the DCS sample. The selection cuts are reported in Table 4.1. The signal yield

Cut on $D^+ \to K^-\pi^+\pi^+$	Value
Multiplicity of primary vertex	> 1
Hadron trigger condition	on
Zprim	< 2 cm
Zsec	< 2 cm
C.L. of secondary vertex	> 0.01
L/σ	> 14
Isolation 1	< 0.01
Isolation 2	< 0.001
Zout	> 3
ΔW_{K^-}	> 4
ΔW_{π^+1}	> 3.5
ΔW_{π^+2}	> 3.5
$\Delta W_{K,\min}$	< 3
$\Delta W_{\pi,\min}$	< 3

Table 4.1: Selection criteria for the $D^+ \to K^-\pi^+\pi^+$ sample.

Decay mode	$N(\mathrm{Gen_{MC}})$	$\mathrm{Yield_{MC}}$	ε %
$D^+ \to K^+\pi^-\pi^+$	5499725	41251 ± 207	0.750 ± 0.004
$D^+ \to K^-\pi^+\pi^+$	5633205	47568 ± 226	0.844 ± 0.004

Table 4.2: Number of MC events and efficiencies for the D^+ branching ratio.

consists of 32714 ± 184 events; the fit is performed with a Gaussian function for the signal and a second order polynomial for the background. In Fig. 4.1 the mass distribution for the normalization channel is shown, for data and MC events.

For the evaluation of the efficiencies the MC generation is based on the results shown in Table 6.4 for the $D^+ \to K^+\pi^-\pi^+$ and on the Dalitz plot analysis performed by the E687 experiment [41] for the $D^+ \to K^-\pi^+\pi^+$. In Fig. 4.2 the Dalitz plots of the two channels, obtained by the MC simulation, are shown. The number of generated and reconstructed events and the corresponding efficiencies are reported in Table 4.2.

From the yields and the efficiencies of the two channels, the branching ratio is calculated to be:

$$\frac{\Gamma\left(D^+ \to K^+\pi^+\pi^-\right)}{\Gamma\left(D^+ \to K^-\pi^+\pi^+\right)} = 0.0065 \pm 0.0008 \tag{4.4}$$

Previous determinations of this branching ratio come from E687 [42] and E791 [43]

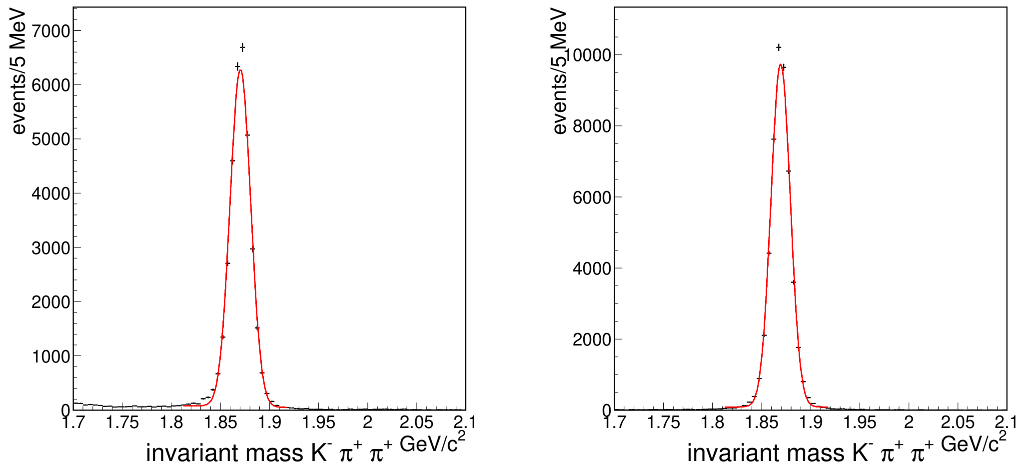

(a) (b)

Figure 4.1: Invariant mass distribution of $D^+ \to K^-\pi^+\pi^+$ normalization channel, for data (a) and MC (b) events.

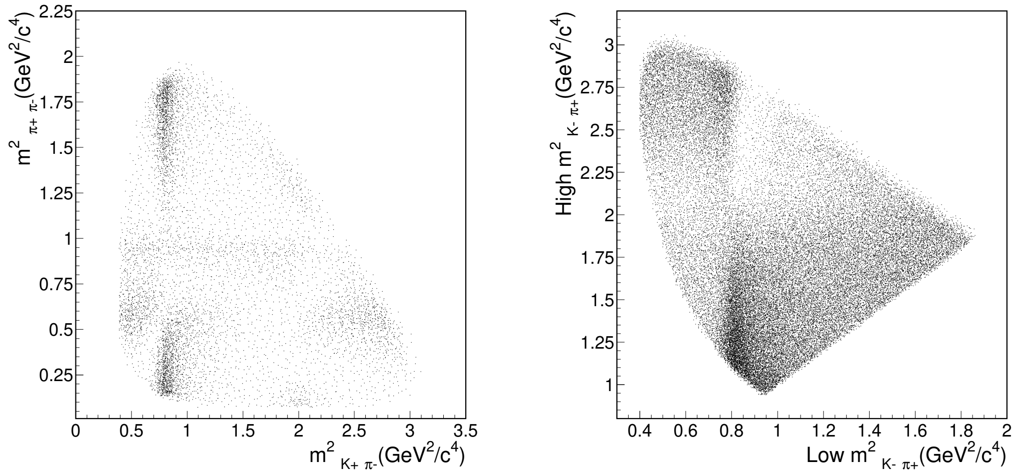

(a) (b)

Figure 4.2: Dalitz plots of MC generated events, for $D^+ \to K^+\pi^-\pi^+$ (a) and $D^+ \to K^-\pi^+\pi^+$ (b) decays.

Split sample	Branching ratio
Run 96 and low momentum	0.0062 ± 0.0017
Run 96 and high momentum	0.0039 ± 0.0014
Run 97 and low momentum	0.0065 ± 0.0012
Run 97 and high momentum	0.0058 ± 0.0011
$\sigma_{split} = 0$	

Table 4.3: Split samples, corresponding branching ratio values and resulting systematic error for D^+.

experiments; they obtain 0.0072 ± 0.0023 and 0.0077 ± 0.0017, respectively. The result reported in this thesis is consistent with the previous ones and reduces the statistical error by about a factor of 2.

4.1.1 Systematic error evaluation

To evaluate the systematic error three contributions are considered, which are added in quadrature to obtain the global systematic error: the *split sample*, *fit variant* and *cut variant* components. In Appendix A the methods used to calculate the split sample and the fit variant errors are outlined; the cut variant component is obtained analogously to the fit variant one.

Split samples

The split sample component is obtained dividing the full data set in 4 subsamples, on the basis of variables which may cause a shift in the branching ratio measurements. The split criteria are the D momentum range (high and low momentum) and the configuration of the vertex detector, that is, before and after the insertion of the upstream silicon system (named *Run 96* and *Run 97*[1]). As dividing momentum value the mean is chosen, which is, for the $D^+ \to K^+\pi^-\pi^+$ reconstructed events, about 70 GeV. Due to the low statistics of the split samples, the fits of the four $D^+ \to K^+\pi^-\pi^+$ invariant mass spectra are performed fixing the signal widths to the values obtained by the fits to the MC spectra. The systematic error due to split samples is calculated to be equal to zero. In Fig. 4.4(a) the comparison between the different splits is shown; in Table 4.3 the values of the branching ratio for each sample and the corresponding systematic error are reported.

[1]Run 9750 is the first run in which the Target Silicon information is used by the reconstruction. This run is picked as the dividing line. This dividing line roughly corresponds to the dividing line between 1996 & 1997 data. All these terms are used interchangeably.

Fit variant

The fit variant component is computed by varying the fitting conditions on the whole data set. In this analysis fit variants include the background and signal shape, the bin size of the mass-distribution histogram and the Monte Carlo generation modeling. More precisely different degrees (3^{rd} and 4^{th}) of the polynomial functions are used for the background parametrization and two Gaussian peaks with the same mean but different widths are used for the signal, to take into account the different resolution in momentum of our spectrometer. The bin size of the invariant mass spectrum, normally equal to 10 MeV per bin for the DCSD, is chosen equal to 5 and 20 MeV per bin, respectively. The fully coherent generation for the decays under analysis is based on the results of the Dalitz plot study presented in this thesis. To access a possible systematic effect in the branching ratio evaluation, coming from the amplitude analysis, coefficients and phases returned by the Dalitz plot fit are varied within their errors (eight different generations are made); also a non coherent MC generation, with only the two dominant resonances $\rho(770)$ and $K^*(892)$ plus a flat contribution, is used for the DCSD in the fit variant calculation. The Dalitz plots corresponding to all these different generations are shown in Fig. 4.3. Finally in the MC generation also the possibility of soft bremsstrahlung photons being created during the decay is considered (here indicated as 'photos on', from the flag in the MC code). The resulting systematic error due to these different 'fit variants' is equal to 0.017%. In Fig. 4.4(b) the comparison between the different branching ratios is shown; in Table 4.4 the values of the branching ratio for each data set and the resulting systematic error are reported.

Cut variant

To investigate the dependence of the branching ratio on the particular choice of cuts, they are varied in a reasonable range, singularly, and the evolution of the different measurements is analyzed. The cuts under study are: L/σ, Zout, isolation1, isolation2, ΔW_K and ΔW_π, i.e. the more discriminating cuts for the signal selection. In Fig. 4.5 the comparison between the different branching ratios obtained with different cuts is shown. To associate explicitly a systematic error to account for the fidelity of the MC in reproducing the cut efficiency, a cut variant error is calculated, analogously to the fit variant, by using the standard deviation of the different branching ratio measurements obtained with the previous sets of cuts; this error is actually overestimated since the statistics of the different samples are different. In the evaluation of the error those points in the evolution which do not satisfy the selection criteria, i.e. which do not sufficiently reject the reflection components, are discarded; these are the first four points in the L/σ evolution (Fig. 4.5(a)) and the first point both in the Zout plot (Fig. 4.5(b)) and in the ΔW_π plot (Fig. 4.10(f)). For these points the number of reflected events from the more important channels is greater then two times the number calculated with the standard cuts. The resulting systematic error is equal to 0.041%. In Table 4.5 the values of the branching ratio

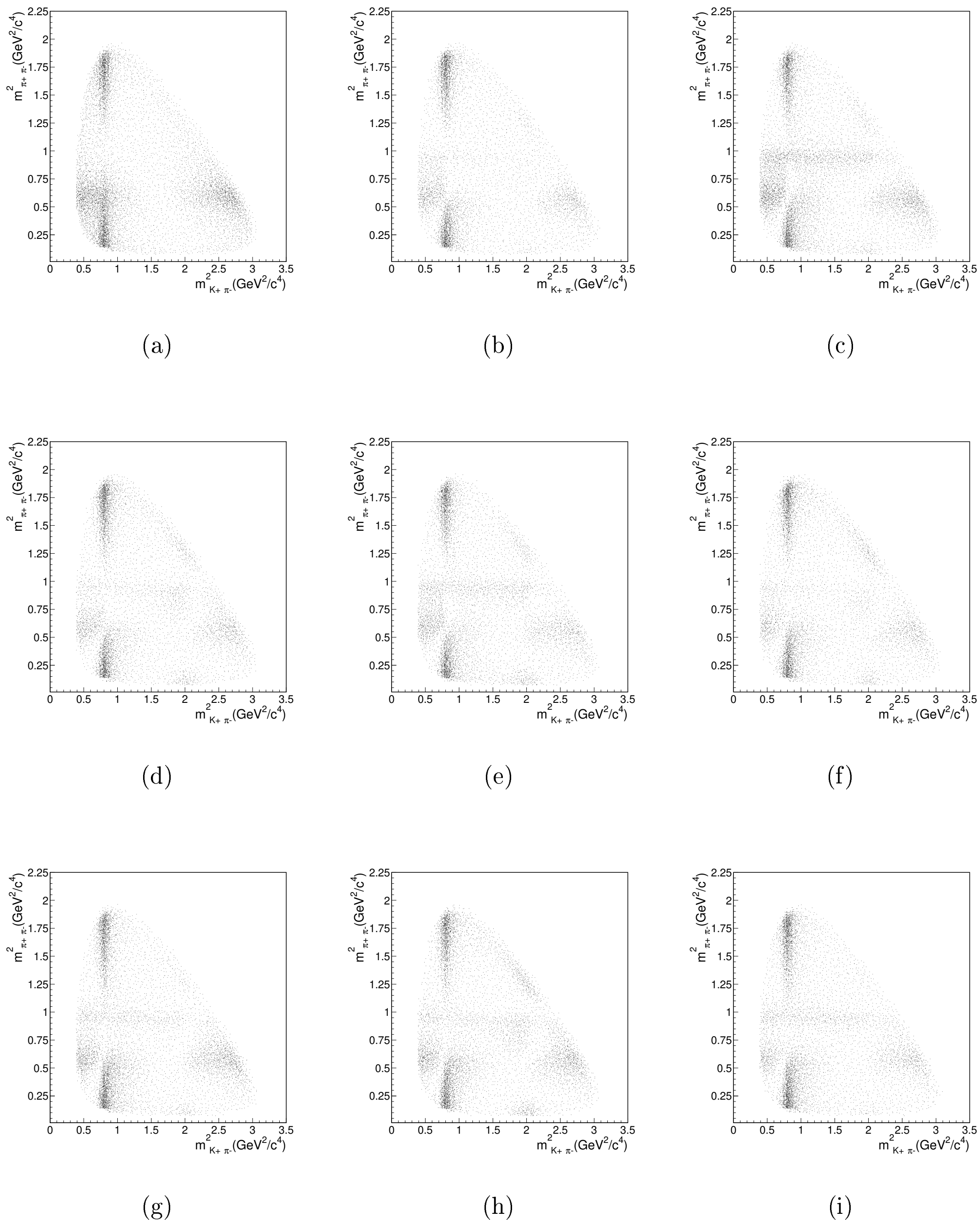

Figure 4.3: $D^+ \to K^+\pi^-\pi^+$ MC Dalitz plots generated with different resonant substructures. In (a) only $\rho(770)$ and $K^*(892)$ with no coherent interference plus a flat contribution are generated; in the remaining plots the results of the Dalitz plot analysis are used, varied within their errors.

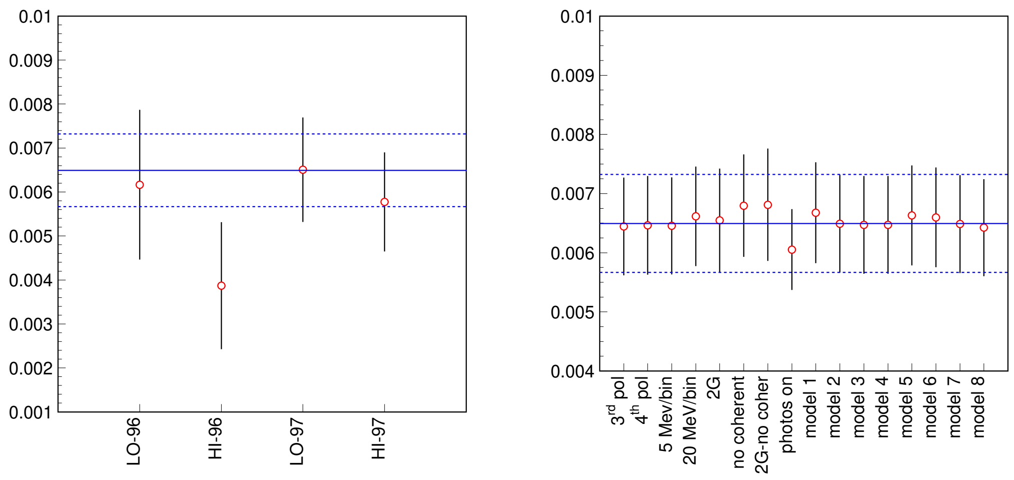

(a) (b)

Figure 4.4: D^+ systematic error coming from split sample (a) and fit variant (b). The solid and dashed lines are the measurement and the statistical error.

Fit variant	Branching ratio
3^{rd} degree	0.0064 ± 0.0008
4^{th} degree	0.0065 ± 0.0008
5 MeV per bin	0.0065 ± 0.0008
20 MeV per bin	0.0066 ± 0.0008
double Gaussian	0.0065 ± 0.0009
no coherent model	0.0068 ± 0.0009
double Gaussian and no coherent model	0.0068 ± 0.001
photos on	0.0061 ± 0.0007
coherent model 1	0.0067 ± 0.0009
coherent model 2	0.0065 ± 0.0008
coherent model 3	0.0065 ± 0.0008
coherent model 4	0.0065 ± 0.0008
coherent model 5	0.0066 ± 0.0008
coherent model 6	0.0066 ± 0.0008
coherent model 7	0.0065 ± 0.0008
coherent model 8	0.0064 ± 0.0008
$\sigma_{fit} = 0.0001696$	

Table 4.4: Fit variant, corresponding branching ratio values and resulting systematic error for D^+.

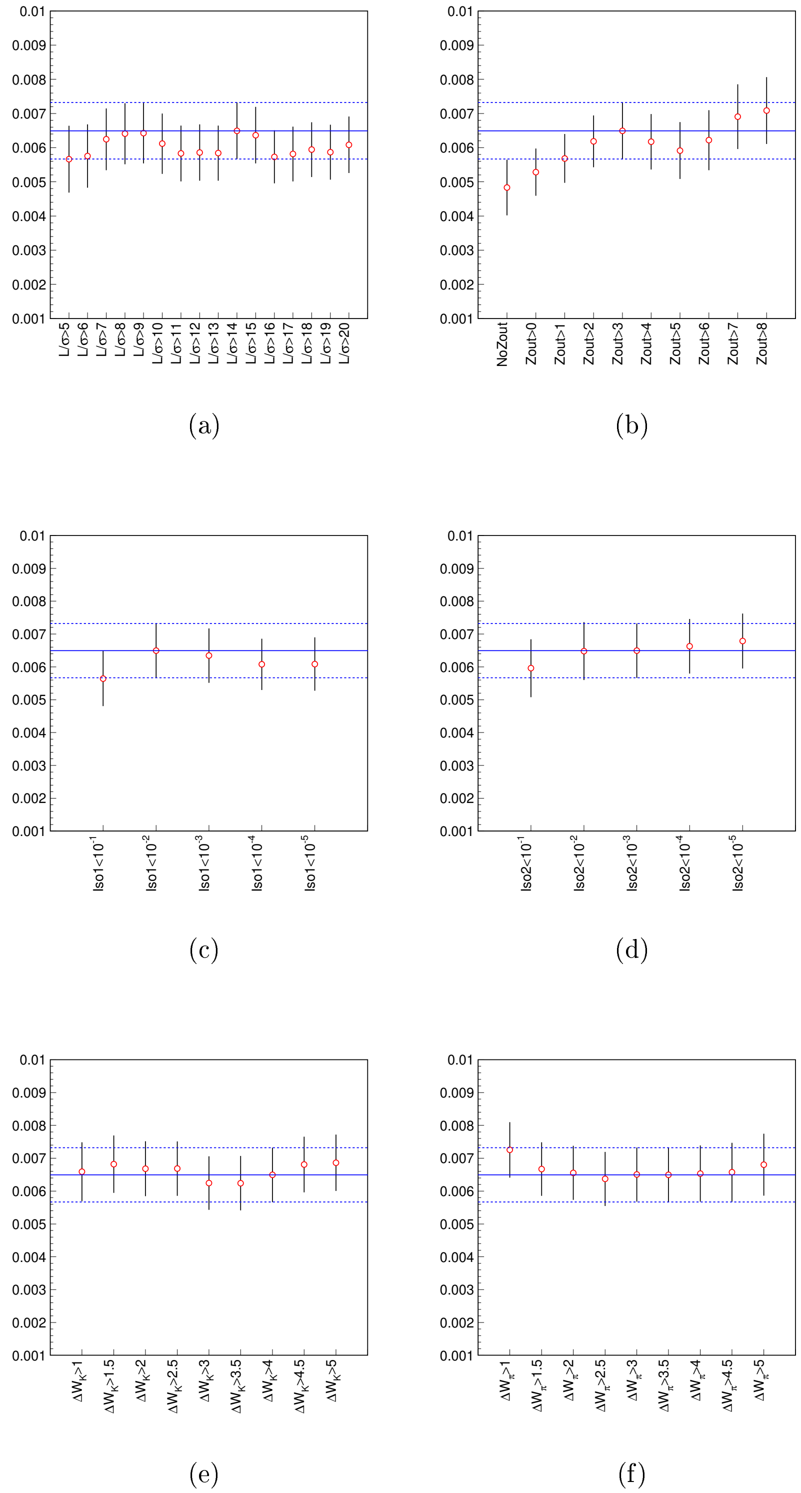

Figure 4.5: D^+ branching ratio cut evolution in L/σ (a), Zout (b), Isolation1 (c), Isolation2 (d), ΔW_K (e) and ΔW_π (f). The solid and dashed lines are the measurement and the statistical error.

for each data sample and the corresponding systematic error are reported.

The global systematic error is obtained adding in quadrature the previous components; Table 4.6 summarizes the result.

4.1.2 Final result

The final determination of the branching ratio is:

$$\frac{\Gamma\left(D^+ \to K^+\pi^+\pi^-\right)}{\Gamma\left(D^+ \to K^-\pi^+\pi^+\right)} = 0.0065 \pm 0.0008 \pm 0.0004 \tag{4.5}$$

This measurement improves the statistical accuracy by approximately a factor of 2 with respect to previous determinations.

According to the Standard Model one expects for this ratio a branching fraction of $\tan^4\theta_C \sim 0.25\%$. While in the DCSD all the quarks in the final state have different flavors, in the CFD indistinguishable quarks are present; so the normalization channel could be suppressed by the Pauli destructive interference. This is the argument generally proposed to explain the lifetime difference between D^+ and D^0. In this simple picture one would expect, neglecting effects of final state interactions, $\tau(D^+)/\tau(D^0) = \Gamma(D^0_{\mathrm{CF}})/\Gamma(D^+_{\mathrm{CF}}) = (1/\tan^4\theta_C) \times \Gamma(D^+_{\mathrm{DCS}})/\Gamma(D^+_{\mathrm{CF}})$. If $(1/\tan^4\theta_C) \times \Gamma(D^+_{\mathrm{DCS}})/\Gamma(D^+_{\mathrm{CF}}) = 2.60 \pm 0.32$ is compared to the precise FOCUS lifetime ratio $\tau(D^+)/\tau(D^0) = 2.538 \pm 0.023$ [38], the interpretation that destructive interference between spectator amplitudes with indistinguishable quarks in the CF D^+ final state is responsible for the lifetime difference between D^+ and D^0 seems to be favoured.

4.2 $\Gamma(D_s^+ \to K^+\pi^-\pi^+)/\Gamma(D_s^+ \to K^+K^-\pi^+)$

The SCS $D_s^+ \to K^+\pi^-\pi^+$ decay fraction is evaluated with respect to the CF $D_s^+ \to K^+K^-\pi^+$ mode. The analysis is performed analogously to the evaluation of the DCS branching ratio. To minimize the systematic effects, the selection cuts for the normalization channel are chosen equal, where possible, to those of the SCS decay. ΔW_{K^-} is required > 2, similar to ΔW_{π^-} in the SCS selection; kinematic cuts are applied to remove the reflections in the $K^-K^+\pi^+$ mode from the CF $D^+ \to K^-\pi^+\pi^+$ and from $D^{*+} \to D^0\pi^+$, followed by the D^0 decay to K^-K^+. The selection criteria are reported in Table 4.7. The signal yield consists of 4033 ± 68 events; as for the D^+ channels the fit is performed with a Gaussian function for the signal and a second order polynomial for the background. The mass invariant plots for the normalization channel are shown in Fig. 4.6, for data and MC events.

For the evaluation of the efficiencies the MC generation is based on the results shown in Table 6.16 for the $D_s^+ \to K^+\pi^-\pi^+$ and on the Dalitz plot analysis per-

Cut variant	Branching ratio		Cut variant	Branching ratio
Zout> 0	0.0053 ± 0.0007		$\Delta W_K > 1$	0.0066 ± 0.0009
Zout> 1	0.0057 ± 0.0007		$\Delta W_K > 1.5$	0.0068 ± 0.0009
Zout> 2	0.0062 ± 0.0008		$\Delta W_K > 2$	0.0067 ± 0.0008
Zout> 3	0.0065 ± 0.0008		$\Delta W_K > 2.5$	0.0067 ± 0.0008
Zout> 4	0.0062 ± 0.0008		$\Delta W_K > 3$	0.0062 ± 0.0008
Zout> 5	0.0059 ± 0.0008		$\Delta W_K > 3.5$	0.0062 ± 0.0008
Zout> 6	0.0062 ± 0.0009		$\Delta W_K > 4$	0.0065 ± 0.0008
Zout> 7	0.0069 ± 0.0009		$\Delta W_K > 4.5$	0.0068 ± 0.0008
Zout> 8	0.0071 ± 0.0010		$\Delta W_K > 5$	0.0069 ± 0.0009
iso1$< 10^{-1}$	0.0056 ± 0.0008		iso2$< 10^{-1}$	0.0060 ± 0.0009
iso1$< 10^{-2}$	0.0065 ± 0.0008		iso2$< 10^{-2}$	0.0065 ± 0.0009
iso1$< 10^{-3}$	0.0063 ± 0.0008		iso2$< 10^{-3}$	0.0065 ± 0.0008
iso1$< 10^{-4}$	0.0061 ± 0.0008		iso2$< 10^{-4}$	0.0066 ± 0.0008
iso1$< 10^{-5}$	0.0061 ± 0.0008		iso2$< 10^{-5}$	0.0068 ± 0.0008
L/$\sigma > 9$	0.0064 ± 0.0009		$\Delta W_\pi > 1.5$	0.0067 ± 0.0008
L/$\sigma > 10$	0.0061 ± 0.0009		$\Delta W_\pi > 2$	0.0066 ± 0.0008
L/$\sigma > 11$	0.0058 ± 0.0008		$\Delta W_\pi > 2.5$	0.0064 ± 0.0008
L/$\sigma > 12$	0.0059 ± 0.0008		$\Delta W_\pi > 3$	0.0065 ± 0.0008
L/$\sigma > 13$	0.0058 ± 0.0008		$\Delta W_\pi > 3.5$	0.0065 ± 0.0008
L/$\sigma > 14$	0.0065 ± 0.0008		$\Delta W_\pi > 4$	0.0065 ± 0.0009
L/$\sigma > 15$	0.0064 ± 0.0008		$\Delta W_\pi > 4.5$	0.0066 ± 0.0009
L/$\sigma > 16$	0.0057 ± 0.0008		$\Delta W_\pi > 5$	0.0068 ± 0.0009
L/$\sigma > 17$	0.0058 ± 0.0008			
L/$\sigma > 18$	0.0059 ± 0.0008			
L/$\sigma > 19$	0.0059 ± 0.0008			
L/$\sigma > 20$	0.0061 ± 0.0008			
$\sigma_{cut} = 0.0004112$				

Table 4.5: Cut variant, corresponding branching ratio values and resulting systematic error for D^+.

Source	Systematic error
Split sample	0
Fit variant	0.0001696
Cut variant	0.0004112
Total	$0.00044 \sim 0.0004$

Table 4.6: Total systematic error for $\Gamma(D^+ \to K^+\pi^+\pi^-)/\Gamma(D^+ \to K^-\pi^+\pi^+)$

Cut on $D_s^+ \to K^+K^-\pi^+$	Value
Multiplicity of primary vertex	> 1
Hadron trigger condition	on
Zprim	< 2 cm
Zsec	< 2 cm
D momentum	> 25 GeV
C.L. of secondary vertex	> 0.01
L/σ	> 10
Isolation 1	< 0.01
Isolation 2	< 0.001
Zout	> 3
ΔW_{K^-}	> 2
ΔW_{K^+}	> 4
ΔW_{π^+}	> 1
$\Delta W_{K,\min}$	< 3
$\Delta W_{\pi,\min}$	< 3

Table 4.7: Selection criteria for the $D_s^+ \to K^+K^-\pi^+$ sample.

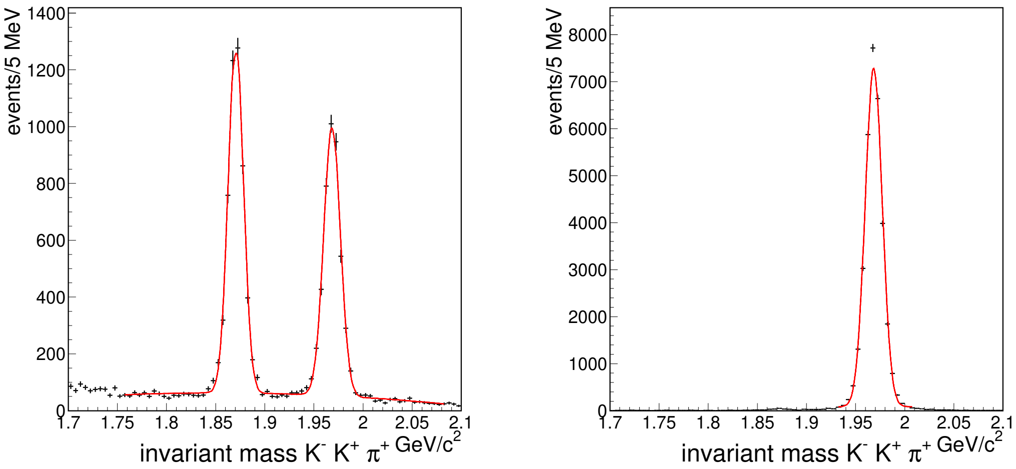

(a) (b)

Figure 4.6: Invariant mass distribution of $D_s^+ \to K^+K^-\pi^+$ normalization channel, for data (a) and MC (b) events.

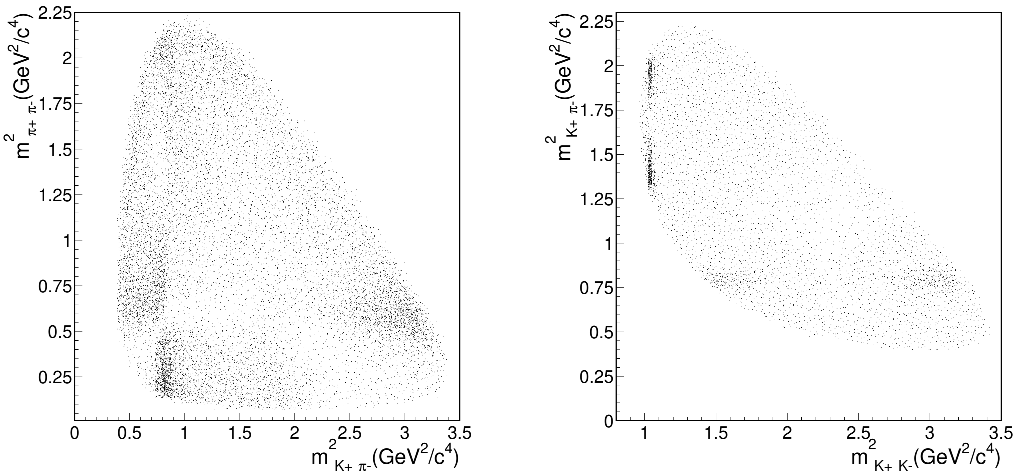

(a) (b)

Figure 4.7: Dalitz plots of MC generated events, for $D_s^+ \to K^+\pi^-\pi^+$ (a) and $D_s^+ \to K^+K^-\pi^+$ (b) decays.

Decay mode	$N(\mathrm{Gen_{MC}})$	$\mathrm{Yield_{MC}}$	ε %
$D_s^+ \to K^+\pi^-\pi^+$	5499725	34562 ± 191	0.628 ± 0.003
$D_s^+ \to K^+K^-\pi^+$	5515540	31349 ± 186	0.568 ± 0.003

Table 4.8: Number of MC events and efficiencies for the D_s^+ branching ratio.

formed by the E687 experiment [44] for the normalization channel. The MC generated Dalitz plots are shown in Fig. 4.7. The number of generated and reconstructed events and the corresponding efficiencies are reported in Table 4.8.

From the yields and the efficiencies of the two channels, the branching ratio is:

$$\frac{\Gamma\left(D_s^+ \to K^+\pi^+\pi^-\right)}{\Gamma\left(D_s^+ \to K^+K^-\pi^+\right)} = 0.127 \pm 0.007 \tag{4.6}$$

The only previous determination of this ratio comes from E687 [42] experiment, which measures 0.23 ± 0.07. The result obtained reduces the statistical error by about a factor of 5 with respect to the previous one.

Split sample	Branching ratio
Run 96 and low momentum	0.131 ± 0.017
Run 96 and high momentum	0.196 ± 0.024
Run 97 and low momentum	0.112 ± 0.011
Run 97 and high momentum	0.152 ± 0.014
$\sigma_{split} = 0.0129$	

Table 4.9: Split samples, corresponding branching ratio values and resulting systematic error for D_s^+.

4.2.1 Systematic error evaluation

The systematic error is evaluated considering three contributions as for the D^+ branching ratio.

Split samples

The split criteria are the D momentum range (for $D_s^+ \to K^+\pi^+\pi^-$ the dividing value is 83 GeV) and the run number (96–97). The fits of the four SCS data samples are performed fixing the widths to the values obtained by the MC fits. The systematic error due to this component is the dominant one; its value turns out to be equal to 1.29%. In Fig. 4.9(a) the comparison between the different splits is shown; in Table 4.9 the values of the branching ratio for each sample and the corresponding systematic error are reported.

Fit variant

The fit variants are exactly the same studied for the D^+ branching ratio. In Fig. 4.8 the different MC models used for this study are shown. The total systematic error, resulting from the fit variant component, is equal to 0.39%. In Fig. 4.9(b) the comparison between the different branching ratios is shown; in Table 4.10 the values of the branching ratio for each data set and the corresponding systematic error are reported.

Cut variant

The selection cuts studied to evaluate the corresponding systematic error are the same as for D^+. The comparison between the different branching ratios obtained with different cuts is shown in Fig. 4.10. In the evaluation of the error the first point in ΔW_K and in the Zout plots is discarded, because with these selection criteria the reflection components are not sufficiently rejected. The resulting systematic error is equal to 0.29%. In Table 4.11 the values of the branching ratio for each data sample

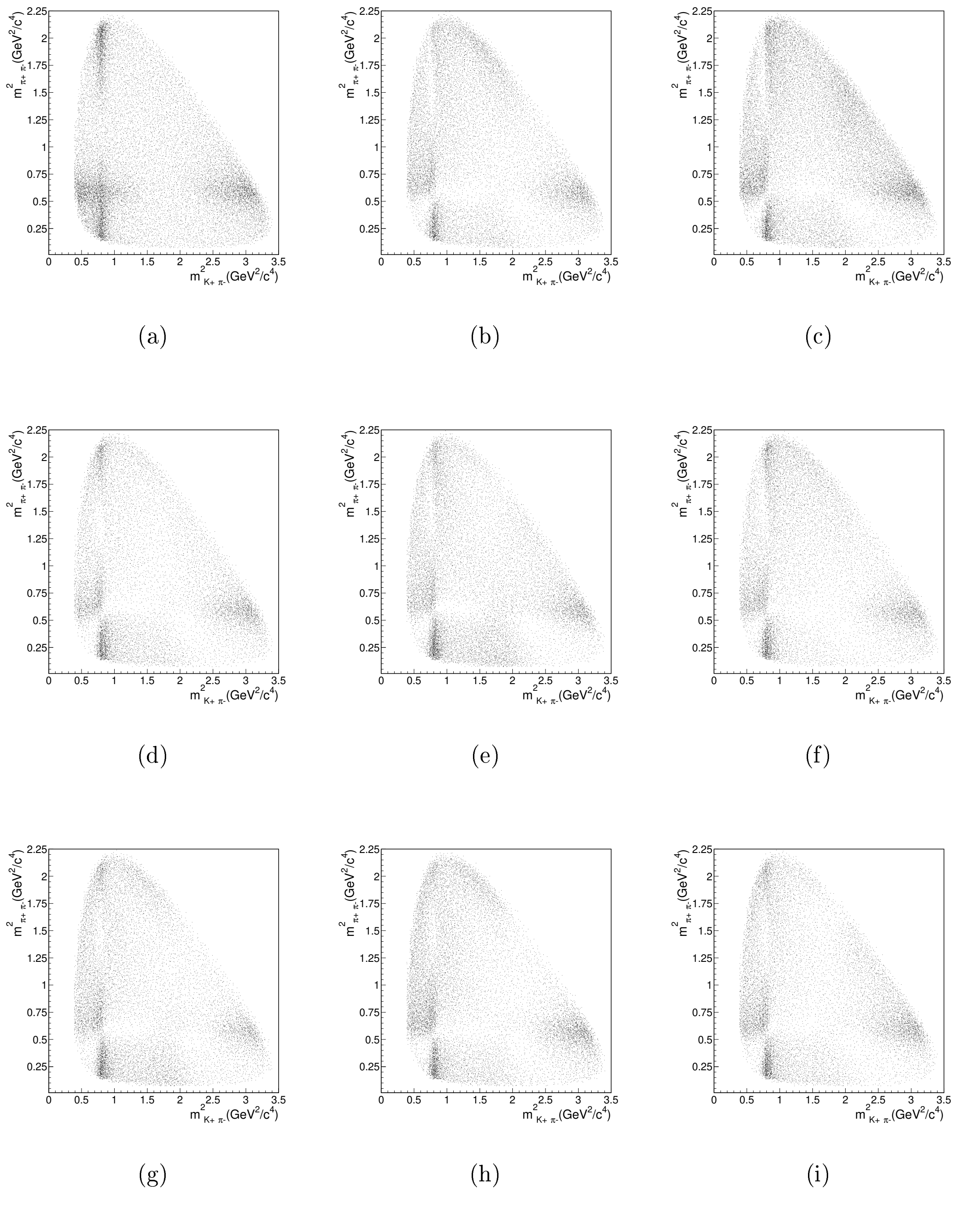

Figure 4.8: $D_s^+ \to K^+\pi^-\pi^+$ MC Dalitz plots generated with different resonant substructures. In (a) only $\rho(770)$ and $K^*(892)$ with no coherent interference plus a flat contribution are generated; in the remaining plots the results of the Dalitz plot analysis are used, varied within their errors.

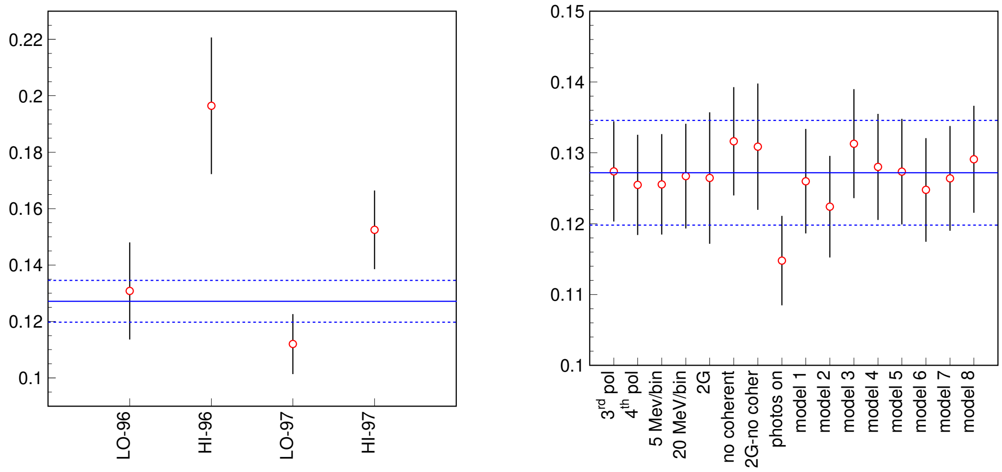

(a) (b)

Figure 4.9: D_s^+ systematic error coming from split sample (a) and fit variant (b). The solid and dashed lines are the measurement and the statistical error.

Fit variant	Branching ratio
3^{rd} degree	$0.127 +/- 0.007$
4^{th} degree	$0.125 +/- 0.007$
5 MeV per bin	$0.126 +/- 0.007$
20 MeV per bin	$0.127 +/- 0.007$
double Gaussian	$0.126 +/- 0.009$
no coherent model	$0.132 +/- 0.008$
double Gaussian and no coherent model	$0.131 +/- 0.009$
photos on	$0.115 +/- 0.006$
coherent model 1	$0.126 +/- 0.007$
coherent model 2	$0.122 +/- 0.007$
coherent model 3	$0.131 +/- 0.008$
coherent model 4	$0.128 +/- 0.007$
coherent model 5	$0.127 +/- 0.007$
coherent model 6	$0.125 +/- 0.007$
coherent model 7	$0.126 +/- 0.007$
coherent model 8	$0.129 +/- 0.008$
$\sigma_{fit} = 0.0039$	

Table 4.10: Fit variant, corresponding branching ratio values and resulting systematic error for D_s^+.

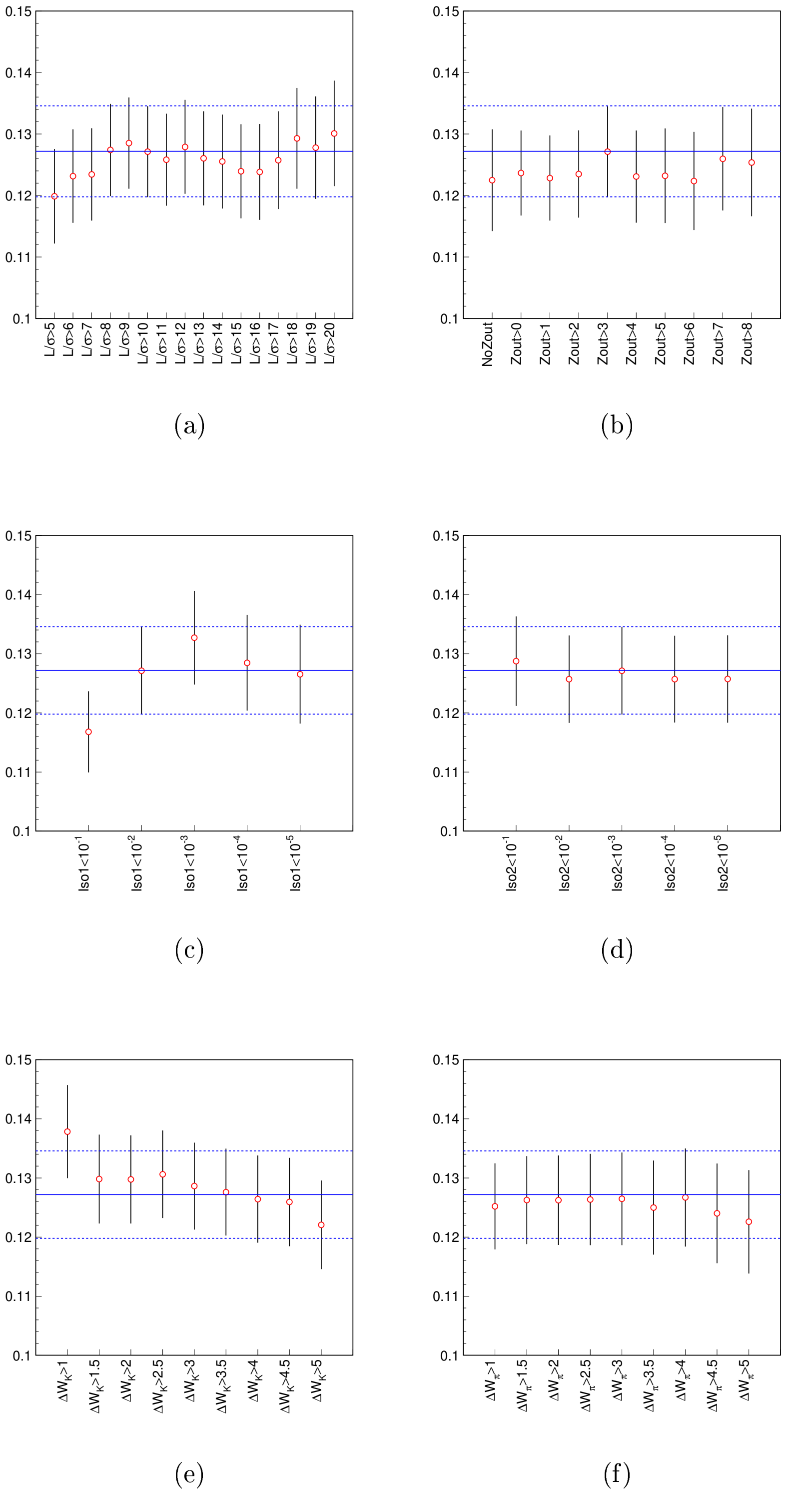

Figure 4.10: D_s^+ branching ratio cut evolution in L/σ (a), Zout (b), Isolation1 (c), Isolation2 (d), ΔW_K (e) and ΔW_π (f). The solid and dashed lines are the measurement and the statistical error.

and the corresponding systematic error are reported.

Cut variant	Branching ratio		Cut variant	Branching ratio
Zout> 0	0.124 ± 0.007		$\Delta W_\pi > 1$	0.125 ± 0.007
Zout> 1	0.123 ± 0.007		$\Delta W_\pi > 1.5$	0.126 ± 0.007
Zout> 2	0.123 ± 0.007		$\Delta W_\pi > 2$	0.126 ± 0.008
Zout> 3	0.127 ± 0.007		$\Delta W_\pi > 2.5$	0.126 ± 0.008
Zout> 4	0.123 ± 0.007		$\Delta W_\pi > 3$	0.126 ± 0.008
Zout> 5	0.123 ± 0.008		$\Delta W_\pi > 3.5$	0.125 ± 0.008
Zout> 6	0.122 ± 0.008		$\Delta W_\pi > 4$	0.127 ± 0.008
Zout> 7	0.126 ± 0.008		$\Delta W_\pi > 4.5$	0.124 ± 0.008
Zout> 8	0.125 ± 0.009		$\Delta W_\pi > 5$	0.123 ± 0.009
L/$\sigma > 5$	0.120 ± 0.008		iso1$< 10^{-1}$	0.118 ± 0.007
L/$\sigma > 6$	0.123 ± 0.008		iso1$< 10^{-2}$	0.127 ± 0.007
L/$\sigma > 7$	0.123 ± 0.008		iso1$< 10^{-3}$	0.133 ± 0.008
L/$\sigma > 8$	0.127 ± 0.008		iso1$< 10^{-4}$	0.128 ± 0.008
L/$\sigma > 9$	0.129 ± 0.007		iso1$< 10^{-5}$	0.127 ± 0.008
L/$\sigma > 10$	0.127 ± 0.007		iso2$< 10^{-1}$	0.129 ± 0.008
L/$\sigma > 11$	0.126 ± 0.007		iso2$< 10^{-2}$	0.126 ± 0.007
L/$\sigma > 12$	0.128 ± 0.008		iso2$< 10^{-3}$	0.127 ± 0.007
L/$\sigma > 13$	0.126 ± 0.008		iso2$< 10^{-4}$	0.126 ± 0.007
L/$\sigma > 14$	0.126 ± 0.008		iso2$< 10^{-5}$	0.126 ± 0.007
L/$\sigma > 15$	0.124 ± 0.008		$\Delta W_K > 1.5$	0.130 ± 0.008
L/$\sigma > 16$	0.123 ± 0.008		$\Delta W_K > 2$	0.130 ± 0.007
L/$\sigma > 17$	0.126 ± 0.008		$\Delta W_K > 2.5$	0.131 ± 0.007
L/$\sigma > 18$	0.129 ± 0.008		$\Delta W_K > 3$	0.129 ± 0.007
L/$\sigma > 19$	0.128 ± 0.008		$\Delta W_K > 3.5$	0.128 ± 0.007
L/$\sigma > 20$	0.130 ± 0.009		$\Delta W_K > 4$	0.126 ± 0.007
			$\Delta W_K > 4.5$	0.126 ± 0.007
			$\Delta W_K > 5$	0.122 ± 0.008
$\sigma_{cut} = 0.0029$				

Table 4.11: Cut variant, corresponding branching ratio values and resulting systematic error for D_s^+.

The global systematic error is obtained adding in quadrature the previous components; Table 4.12 shows the final result.

Source	Systematic error
Split sample	0.0129
Fit variant	0.0039
Cut variant	0.0029
Total	$0.0138 \sim 0.014$

Table 4.12: Total systematic error for $\Gamma(D_s^+ \to K^+\pi^-\pi^+)/\Gamma(D_s^+ \to K^+K^-\pi^+)$

4.2.2 Final result

The final determination of the branching ratio is:

$$\frac{\Gamma\left(D_s^+ \to K^+\pi^+\pi^-\right)}{\Gamma\left(D_s^+ \to K^+K^-\pi^+\right)} = 0.127 \pm 0.007 \pm 0.014 \tag{4.7}$$

For this measurement one expects, according to the Standard Model, a branching fraction of $\tan^2\theta_{\mathrm{C}} \sim 5\%$. A factor of 2 increase is caused by the different $D_s^+ \to K^+\pi^-\pi^+$ and $D_s^+ \to K^+K^-\pi^+$ phase spaces. The still remaining disagreement between the measurement and the SM prediction could be explained by FSI effects in the normalization channel. It will thus be interesting to perform a Dalitz plot analysis of $D_s^+ \to K^+K^-\pi^+$ before drawing any conclusion.

Chapter 5

Dalitz-plot analysis formalism

The Dalitz plot is a powerful and proper tool to investigate the multi-body decay. Its analysis provides the full set of observables of the decay: coefficients and relative phases of the different amplitudes contributing to the same final state. Multi-body decays can occur via various strong resonances which can interfere with each other. The Dalitz plot analysis allows to measure the phase shifts between different resonant components and so to gauge the role of FSI in the decay, shedding some light onto the underlying weak decay dynamics.

The decay amplitude, for the Dalitz plot analyses of the Cabibbo suppressed decays reported in this thesis, is described as a coherent sum of Breit-Wigner functions (which we will refer to as "isobar model"). More rigorous treatments, such as that based on the *K-matrix* formalism [2], are not viable for these analyses, because of the limited statistics of the samples, along with the large number of free parameters which would be necessary to account for the simultaneous presence of both $\pi\pi$ and $K\pi$ resonances.

5.1 The Dalitz plot and the decay amplitude

The kinematics of a spinless particle into three pseudoscalar mesons can be described by two independent variables. In fact the 4-momenta of the three daughter particles correspond to 12 unknown quantities; the energy and 3-momenta conservation plus the constraints on the three masses reduce to five the number of independent variables. Among them, three correspond to the Euler angles that specify the orientation of the final system relative to the initial particle. Since the parent particle is spinless, there is not a favourite direction for the decay and it can not depend on these three angles; so only two independent kinematic variables remain to describe the decay.

We indicate with P and M the 4-momenta and the mass of the decaying particle and with $P_{j=1,2,3}$ and $m_{j=1,2,3}$ the 4-momenta and the masses of the final particles in the rest frame of M: $P = (E, \boldsymbol{p})$ and $P_j = (E_j, \boldsymbol{p_j})$. We define the invariant mass of the system $j-k$ in the rest frame of M as $m_{jk}^2 = (P_j + P_k)^2$. For the 4-momenta conservation: $P = P_i + P_{jk}$. So:

$$P^2 = M^2 = (P_{jk} + P_i)^2 = (E_{jk} + E_i)^2 - |\boldsymbol{p_{jk}} + \boldsymbol{p_i}|^2 \tag{5.1}$$

In the rest frame of the decaying particle $\boldsymbol{p} = 0$ and consequently:

$$\boldsymbol{p_{jk}} = -\boldsymbol{p_i} \quad \Rightarrow \quad E_{jk} = M - E_i \tag{5.2}$$

From here it follows that:

$$p_i^2 = E_i^2 - m_i^2 = p_{jk}^2 = (M - E_i)^2 - m_{jk}^2 = M^2 - 2ME_i + E_i^2 - m_{jk}^2 \tag{5.3}$$

and therefore we obtain the particle energy as function of the masses:

$$E_i = \frac{M^2 - m_{jk}^2 + m_i^2}{2M} \tag{5.4}$$

From this relation and from the energy conservation law we have:

$$M = E_1 + E_2 + E_3 = \frac{3M^2 - m_{12}^2 - m_{13}^2 - m_{23}^2 + m_1^2 + m_2^2 + m_3^2}{2M} \tag{5.5}$$

from which a constraint between all the masses is obtained:

$$m_{12}^2 + m_{13}^2 + m_{23}^2 = M^2 + m_1^2 + m_2^2 + m_3^2 \tag{5.6}$$

Therefore only two of the invariant masses m_{jk} are independent and they can be chosen as kinematic variables to describe the decay. This can be verified looking at the partial decay rate of a pseudoscalar meson in three spin-0 particles; in the rest frame of M it is given in terms of the Lorentz-invariant matrix element $\mathcal{M}$, which contains the decay dynamics, by:

$$d\Gamma = \frac{(2\pi)^4}{2M} |\mathcal{M}|^2 d\phi_3 \tag{5.7}$$

where $d\phi_3$ is the three-body phase space given by:

$$d\phi_3 = \delta^4 \left(P - \sum_{i=1}^{3} P_i \right) \prod_{i=1}^{3} \frac{d^3 p_i}{(2\pi)^3 \, 2E_i} \tag{5.8}$$

From the evaluation of the phase space we obtain the standard form of the decay rate:

$$d\Gamma = \frac{1}{(2\pi)^3} \frac{1}{32M^3} |\mathcal{M}|^2 dm_{12}^2 dm_{13}^2 \tag{5.9}$$

The Dalitz plot is defined as the scatter plot in m_{12}^2 and m_{13}^2. If the decay goes directly in the final state, no dynamics is involved and the matrix element $|\mathcal{M}|^2$ is constant; the allowed region of the plot is uniformly populated. In contrast, if the decay proceeds via subresonant states, some accumulations of events are visible in the plot, giving immediate information on $|\mathcal{M}|^2$; these structures appear in the plot at the squared mass of the corresponding resonance.

The allowed region of the Dalitz plot is obtained through kinematic considerations. Since the invariant mass of the two particle j and k is:

$$m_{jk}^2 = (E_j + E_k)^2 - |\boldsymbol{p_j} + \boldsymbol{p_k}|^2 \tag{5.10}$$

the minimum of m_{jk}^2 corresponds to the maximum of $|\boldsymbol{p_j} + \boldsymbol{p_k}|^2$, i.e. when $\boldsymbol{p_j}$ and $\boldsymbol{p_k}$ are parallel. From here, with some calculations, it is deduced that the minimum of m_{jk} is:

$$m_{jk}(min) = m_j + m_k \tag{5.11}$$

Analogously the maximum of m_{jk} is obtained when $\boldsymbol{p_j}$ and $\boldsymbol{p_k}$ are antiparallel; the maximum value for m_{jk} is:

$$m_{jk}(max) = M - m_i \tag{5.12}$$

Not the entire region $\left[\left(m_{ij}^2\right)_{min}, \left(m_{ij}^2\right)_{max}\right] \times \left[\left(m_{jk}^2\right)_{min}, \left(m_{jk}^2\right)_{max}\right]$ is allowed to the final states, because of the constraint on the 4-momenta. For each $m_{ij}^2 \in \left[\left(m_{ij}^2\right)_{min}, \left(m_{ij}^2\right)_{max}\right]$, m_{jk}^2 is maximum when $\boldsymbol{p_j}$ is antiparallel to $\boldsymbol{p_k}$ and it is minimum when $\boldsymbol{p_j}$ is parallel to $\boldsymbol{p_k}$. Fixing m_{ij}^2, m_{jk}^2 can move from

$$m_{jk}^2|_{min} = (E_j + E_k)^2 - |\boldsymbol{p_j} + \boldsymbol{p_k}|^2 \tag{5.13}$$

to

$$m_{jk}^2|_{max} = (E_j + E_k)^2 - |\boldsymbol{p_j} - \boldsymbol{p_k}|^2 \tag{5.14}$$

Writing E_j, E_k, $\boldsymbol{p_j}$ and $\boldsymbol{p_k}$ in the rest frame of m_{ij}, we obtain the curves $m_{jk}^2|_{min}\left(m_{ij}^2\right)$ and $m_{jk}^2|_{max}\left(m_{ij}^2\right)$, which bound the Dalitz plot allowed region (see Fig. 5.1).

To extract informations about the underlying processes involved in the decay, a parametrization of the total decay amplitude $\mathcal{M}$ is necessary to perform a fit to the Dalitz plot surface. A quasi-two-body channel of the type

$$\begin{array}{ll} D \to & \mathcal{R} + 3 \\ & \hookrightarrow 1 + 2 \end{array} \tag{5.15}$$

can be visualized a la Feynman, as shown in Fig. 5.2. The amplitude of the process is given by three factors: the barrier form factors F_D and F_r for the production of $\mathcal{R} + 3$ and $1 + 2$, the angular distributions of the final state particles, which ensure the momentum conservation in the decay, and the dynamical function describing the resonance $\mathcal{R}$.

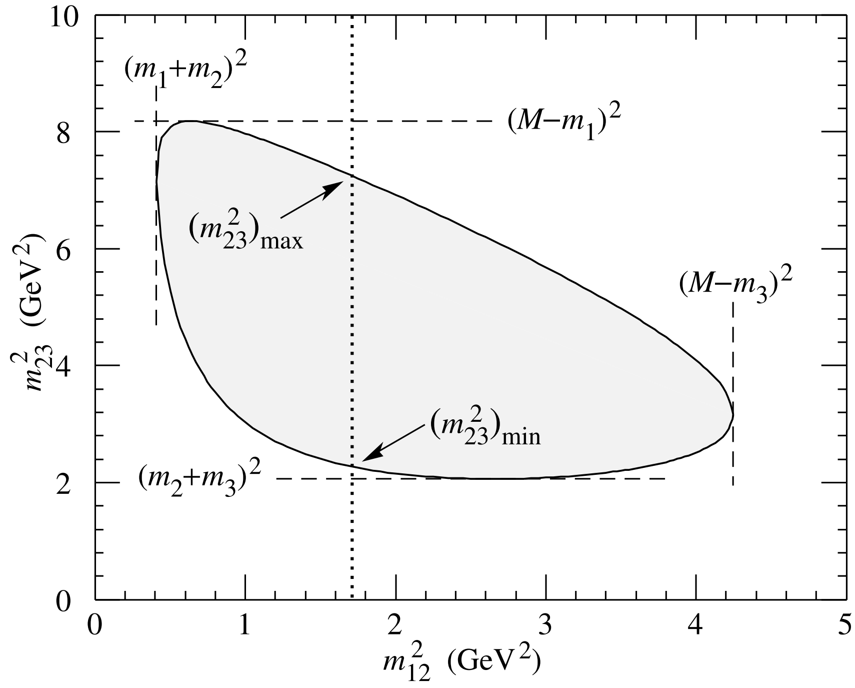

Figure 5.1: Allowed region for the Dalitz plot.

F_D and F_r represent the strong coupling at each decay vertex and are chosen according to Blatt–Weisskopf [47] as:

$$\begin{array}{ll} F = 1 & \text{for spin 0 resonances} \\ F = (1 + R^2 p^{*2})^{-1/2} & \text{for spin 1 resonances} \\ F = (9 + 3R^2 p^{*2} + (R^2 p^{*2})^2)^{-1/2} & \text{for spin 2 resonances} \end{array} \tag{5.16}$$

p^* is the momentum of the decay products in the rest frame of $\mathcal{R}$ and R represents the hadronic radius taken from [48].

Also the angular function (named $\mathcal{S}(1\ 3)$) depends from the spin of the resonance; its expression, in the Zemach formalism [49, 50], is given by:

$$\begin{array}{lll} \mathcal{S}(1\ 3) &=& 1 \quad \text{for spin 0 resonances} \\ \mathcal{S}(1\ 3) &=& (-2\ \boldsymbol{p_3} \cdot \boldsymbol{p_1}) \quad \text{for spin 1 resonances} \\ \mathcal{S}(1\ 3) &=& 2(p_3 p_1)^2 (3\cos^2\theta_{13} - 1) \quad \text{for spin 2 resonances} \end{array} \tag{5.17}$$

$\boldsymbol{p_1}$ and $\boldsymbol{p_3}$ are the momenta of particles 1 and 3 in the rest frame of the 1-2 system and θ_{13} is the angle between particles 1 and 3 in the same frame, called helicity angle. If the resonance $\mathcal{R}$ is a spin particle, there is a correlation between the particle 1,

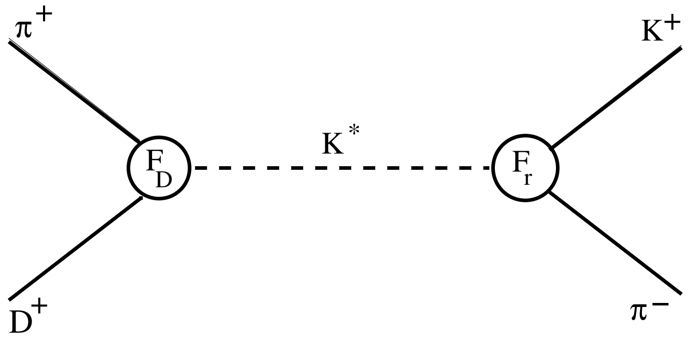

Figure 5.2: Feynman diagram for the $D^+ \to K^+\pi^-\pi^+$ decay, through the resonant state $K^*(892)$.

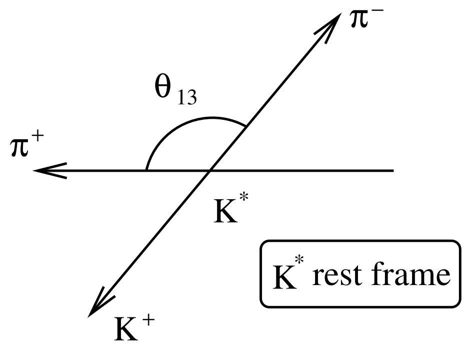

Figure 5.3: Helicity angle definition.

coming from the $\mathcal{R}$ decay, and the particle 3, remembering the flight direction of $\mathcal{R}$. θ_{13} can be obtained from the m_{13} definition:

$$\begin{aligned} m_{13}^2 &= (E_1 + E_3)^2 - (\vec{p_1} + \vec{p_3})^2 = \\ &= m_1^2 + m_3^2 + 2E_1E_3 - 2p_1p_3\cos\theta_{13} \end{aligned} \tag{5.18}$$

The choice of the particle 1 is arbitrary: the particle 2 can be chosen and the helicity conservation can be expressed through $\boldsymbol{p_2}$, $\boldsymbol{p_3}$ and θ_{23}. This angle is complementary to 180° of θ_{13} in the 1-2 frame. The two representations are equivalent; the difference comes out in the measured phases: exchanging 1 and 2 results in a phase shift of 180 degrees. Therefore it is important to specify the helicity convention, to be able to compare the results with those obtained by other experiments. In the D^+ and $D_s^+ \to K^+\pi^-\pi^+$ Dalitz plot analyses reported in this thesis, the particle 1 is chosen as the particle with D opposite sign (Fig. 5.3). The $\cos\theta_{13}$ dependence in the vectorial states reflects in a depopulation of the central region of the resonant band.

The j-spin resonance $\mathcal{R}$ is modeled with a Breit-Wigner function:

$$BW(1\ 2|\mathcal{R}) = \frac{1}{m_r^2 - m_{12}^2 - i\Gamma_{12}m_r} \tag{5.19}$$

Γ_{12} is given by:

$$\Gamma_{12} = \Gamma_r \left(\frac{p^*}{p_r^*}\right)^{2j+1} \frac{m_r}{m_{12}} \frac{F_r^2(p^*)}{F_r^2(p_r^*)} \tag{5.20}$$

where the subscript r denotes the on-shell values.

The amplitude describing the process of Eq. 5.15 is therefore:

$$A_r = F_D\ F_r\ \mathcal{S}(1\ 3)\ BW(1\ 2|r) \tag{5.21}$$

The total decay amplitude $\mathcal{M}$ is written as a coherent sum of amplitudes corresponding to a constant term for the uniform direct three-body decay and to different resonant channels:

$$\mathcal{M} = a_0 e^{i\delta_0} + \sum_j a_j e^{i\delta_j}\ A_j \tag{5.22}$$

Additional care has to be applied to describe the $f_0(980)$ resonance because of the opening of the $K\overline{K}$ channel near its pole mass. Two possible parametrizations are considered for the $f_0(980)$ amplitude in this thesis: the simpler single Breit-Wigner form (Eq. 5.19) and the more proper Flattè coupled-channel function [51], given by:

$$BW(1\ 2|f_0(980)) = \frac{1}{m_{f_0}^2 - m_{12}^2 - i m_{f_0}(\Gamma_{\pi\pi} + \Gamma_{KK})} \tag{5.23}$$

with

$$\Gamma_{\pi\pi} = g_\pi \left[\frac{1}{4}m_{12}^2 - m_\pi^2\right]^{1/2} \tag{5.24}$$

$$\Gamma_{KK} = \frac{1}{2} g_K \left[\left(\frac{1}{4}m_{12}^2 - m_{K^+}^2\right)^{1/2} + \left(\frac{1}{4}m_{12}^2 - m_{K^0}^2\right)^{1/2}\right] \tag{5.25}$$

5.2 The fitting procedure

5.2.1 The likelihood function

To measure the coefficients a_j of the various decay amplitudes as well as their relative phases δ_j, we fit the intensity function $|\mathcal{M}|^2 = \mathcal{M}\mathcal{M}^*$ (Eq. 5.22) to the observed distribution of final states on the Dalitz plot. The signal probability density function pdf_s is obtained as:

$$pdf_s = \varepsilon(m_{12}^2, m_{13}^2) \times \frac{|\mathcal{M}|^2}{\mathcal{N}_s} \tag{5.26}$$

$\varepsilon(m_{12}^2, m_{13}^2)$ is the efficiency correction function, discussed below (see Section 5.2.3). $\mathcal{N}_s$ is the normalization constant, defined as the integral of $\varepsilon \times |\mathcal{M}|^2$ across the Dalitz plot:

$$\mathcal{N}_s = \int_{DP} \varepsilon |\mathcal{M}|^2 dm_{12}^2 dm_{13}^2 \tag{5.27}$$

Since the intensity over the Dalitz plot is unchanged by an overall phase factor, one phase (usually taken to be the dominant contribution) is fixed to 0. Similarly, one of the a_j's is actually determined through the normalization condition and it can be fixed to 1. In the D^+ and $D_s^+ \to K^+\pi^-\pi^+$ analyses reported in this thesis, the fixed parameters are those of the $\rho(770)$, which is dominant mode in both decays. Once the fit parameters are obtained, it has become customary to present information on the amplitude strengths a_j indirectly, by way a "fit fraction". The fit fraction f_j into a given resonance is defined, operatively, by taking the integral of an intensity which just includes the amplitude contribution for the given mode divided by the integral of the intensity with all amplitudes present[1]:

$$f_j = \frac{\int \left| a_r e^{i\delta_r} A_r \right|^2 d\mathcal{DP}}{\int |\mathcal{M}|^2 d\mathcal{DP}} \tag{5.28}$$

The fit fraction roughly represents the probability that the state decays via a given resonant channel. Of course, unlike a conventional probability, it is possible to find $\sum_j f_j \neq 1$ owing to interference. A advantage of quoting fit fractions besides the amplitude coefficients is that many phases, Breit-Wigner, and spin factor conventions cancel out in the ratio, thus allowing for easy comparison between different analysis.

To solve for the fit parameters a_j and δ_j we use a maximum likelihood method. The signal region likelihood $\mathcal{L}_{sr}$ is the product of *pdf*'s for the entire sample:

$$\mathcal{L}_{sr} = \prod_{i=1}^{N_{ev}} pdf_i \tag{5.29}$$

N_{ev} is the number of events in the signal region ($\pm 2\sigma$ from the mass peak), being inside the kinematic Dalitz plot boundary. $\mathcal{L}_{sr}$ is a function of the measured observables $\vec{x} = (m_{12}^2, m_{13}^2)$ and of the fit parameters $\vec{\beta} = \left(\vec{a}, \vec{\delta}\right)$. We minimize the function $w_{sr} = -2 \ln \mathcal{L}_{sr}$ in order to obtain the fit parameters $\vec{\beta}$.

It has to be remembered that an event in the signal region may be from the actual decay under study or it may be from the background. To account for this, a term for the background events is included in the probability density function:

$$pdf = \varepsilon\alpha \frac{|\mathcal{M}|^2}{\mathcal{N}_s} + \varepsilon(1-\alpha)\frac{\mathcal{B}}{\mathcal{N}_{bg}} \tag{5.30}$$

[1] $d\mathcal{DP}$ represents the differential volume on the Dalitz plot.

α represents the fraction of signal events in the $\pm 2\sigma$ region from the mass peak. This *pdf* expression ensures that identifying an event as 'signal' or 'background' are mutually exclusive occurrences. So these contributions have to be normalized separately to the *pdf*. The normalization integral $\mathcal{N}_{bg}$ is explicitly written as:

$$\mathcal{N}_{bg} = \int_{DP} \mathcal{B} \; d\mathcal{DP} \tag{5.31}$$

The signal fraction α and the background parameters b_i (see Eq. 5.36) are constrained, according to a Gaussian term, to values obtained through mass spectrum and sideband fits, respectively $\overline{\alpha}$ and $\overline{b_i}$. The penalty terms are:

$$\exp\left[-\left(\frac{(\alpha-\overline{\alpha})^2}{2\sigma_{\overline{\alpha}}}\right)\right] \tag{5.32}$$

$$\exp\left[-\left(\sum_{jk=1}^{n}\frac{\left(b_j-\overline{b_j}\right)\left(b_k-\overline{b_k}\right)}{2\sigma_{jk}}\right)\right] \tag{5.33}$$

Including these term in the *pdf*, the final likelihood is:

$$\begin{aligned} \mathcal{L}_f &= \prod_{i=1}^{N_{ev}} pdf_i \times \exp\left[-\left(\frac{(\alpha-\overline{\alpha})^2}{2\sigma_{\overline{\alpha}}}\right)\right] \\ &\times \exp\left[-\left(\sum_{j,k=1}^{n}\frac{\left(b_j-\overline{b_j}\right)\left(b_k-\overline{b_k}\right)}{2\sigma_{jk}}\right)\right] \end{aligned} \tag{5.34}$$

and the actual function w_{sr} we are minimizing is:

$$\begin{aligned} w_{sr} &= -2\ln\mathcal{L}_f \\ &= -2\sum_{i=1}^{N_{ev}}\ln\left[\varepsilon_i\alpha\frac{|\mathcal{M}|_i^2}{\mathcal{N}_s}+(1-\alpha)\frac{\mathcal{B}}{\mathcal{N}_{bg}}\right]+\left[\frac{\alpha-\overline{\alpha}}{\sigma_{\overline{\alpha}}}\right]^2 \\ &+ \sum_{j,k}\frac{\left(b_j-\overline{b_j}\right)\left(b_k-\overline{b_k}\right)}{2\sigma_{jk}} \end{aligned} \tag{5.35}$$

The minimization of w_{sr}, done using the CERN minimization utility `MINUIT` [52], returns the optimal values for a_j, δ_j, α and b_j.

5.2.2 The background parametrization

Since we can not know the background in the signal region, we assume regions close to the signal peak (sidebands) to be a good representation of the background under the signal. An initial background parametrization is obtained through a fit to the sideband Dalitz plot.

The shape of the background is written as an incoherent sum of a polynomial function plus Breit-Wigner components, to account for any feed-through from resonances:

$$\mathcal{B} = (1 + b_1 X^2 + b_2 Y^2 + b_3 XY + b_4 X + b_5 Y)^2 + \sum_{i=1}^{N_R bckg} |b_{i+5} BW_i|^2 \tag{5.36}$$

where $X = m_{12}^2$ and $Y = m_{13}^2$. To fit the sideband data the normalized probability density function pdf_{bg} is considered:

$$pdf_{bg} = \frac{\mathcal{B}}{\mathcal{N}_{bg}} \tag{5.37}$$

where:

$$\mathcal{N}_{bg} = \int_{SBlimits} \mathcal{B}\ d\mathcal{DP} \tag{5.38}$$

We perform a joint fit to both the low and high sideband data for the coefficients b_i of Eq. 5.36, by again forming a continuous likelihood function $\mathcal{L}_{sb}$:

$$\mathcal{L}_{sb} = \prod_{SB\ \ events\ \ j} pdf_{bg,j} \tag{5.39}$$

Again the method is to minimize $-2\ln\mathcal{L}_{sb}$. The b_i values returned by the sideband fit, with the corresponding covariance matrix, are used to introduce likelihood penalty terms when the fit to the signal region is performed (Eq. 5.35).

5.2.3 The efficiency correction

Eq. 5.30 contains the function $\varepsilon(m_{12}^2, m_{13}^2)$ which corrects for the geometrical acceptance and reconstruction efficiency. As first approximation the efficiency does not depend on the decay dynamics but depends only on the position over the Dalitz plot where it is calculated; the idea is to divide the phase space into regions in which the efficiency is constant and estimate ε in each bin. To do this, a high statistics MC sample is generated; the ratio bin per bin between the MC reconstructed events and the MC generated events gives an estimate of the efficiency. A polynomial function is chosen to parametrize the efficiency; its coefficients are obtained through a fit, using a binned likelihood defined as:

$$\mathcal{L}^{\varepsilon} = \prod_{i=1}^{N_{bin}} p_j^{\varepsilon} \tag{5.40}$$

N_{bin} is the number of bins in which the Dalitz plot is divided; p_j^{ε} is the probability for the j-th bin and it has the form of a binomial distribution:

$$p_j^{\varepsilon}(n_j^r; \varepsilon; n_j^g) = \binom{n_j^g}{\varepsilon} \varepsilon^{n_j^r} (1-\varepsilon)^{n_j^g - n_j^r} \ = \ \frac{n_j^g!}{n_j^r!(n_j^g - n_j^r)!} \varepsilon^{n_j^r} (1-\varepsilon)^{n_j^g - n_j^r} \tag{5.41}$$

n_j^g is the number of generated events in the j-th bin, n_j^r is the number of reconstructed events in the same bin and $\varepsilon(m_{12}^2, m_{13}^2)$ is the reconstruction probability. n_j^g and n_j^r are fixed in each bin; the likelihood fit determines the polynomial coefficients of ε which maximize $\mathcal{L}^{\varepsilon}$.

5.2.4 The goodness of the fit

To gauge the goodness of the fit and to compare different fit results we evaluate the confidence level through an adaptive binning algorithm [53], designed to provide a statistically valid χ^2 test over the finest binning scales supported by the sample size. It therefore provides a stringent χ^2 test for a given model.

The algorithm begins by considering a single bin containing all events and having corner coordinates defined by kinematic boundary limits. This is the starting point for bin splitting, and we consider splitting into two new bins. The splitting procedure goes on until each bin used in the χ^2 contain at least N events. In the case of the D^+ and $D_s^+ \to K^+\pi^-\pi^+$ analyses reported in this thesis, N is chosen equal to 10. To decide how to split the bin, we look at the average derivative in the Dalitz plot variables across the bin. We split the bin in the direction of most rapid change, at the location of the centroid (i.e. the average value of the coordinate weighted by the intensity). Once the partitioning is determined and the χ^2 for each bin is calculated, the total χ^2 for degrees of freedom (equal to the number of bins minus the number of fitted parameters) is obtained. Finally we evaluate the fit C.L. through the CERNILB routine `PROB`.

Chapter 6

Amplitude analysis results

To investigate the decay dynamics of the Cabibbo suppressed decays reported in this thesis, a maximum likelihood fit to the Dalitz plots is performed, as built in the previous chapter, providing the coefficients of the various decay amplitudes as well as their relative phases. The D^+ and D_s^+ samples are fitted with likelihood functions $\mathcal{L}$ consisting of signal and background probability densities. The parametrization of the signal events is based on a coherent sum of Breit-Wigner functions, to describe different resonant channels, and a constant term for the uniform direct three-body decay. The probability density function is corrected for geometrical acceptance and reconstruction efficiency. The Dalitz plot of mass sidebands is fitted through an incoherent sum of a polynomial function plus resonant Breit-Wigner components; the resulting fit function is used to describe the background under the signal peak, according to the assumption that the shape of the background in the sidebands is a good representation of the background in the signal region. Due to the suppressed nature of the channels under analysis, copious decays can produce contaminations because of Čerenkov misidentifications and can induce different reflected structures in the regions under study. A careful investigation of possible residual effects induced by reflections has been presented in Chapter 3.

6.1 $D^+ \to K^+\pi^-\pi^+$

6.1.1 Fit strategy

The Dalitz plot analysis for $D^+ \to K^+\pi^+\pi^-$ is performed on a sample of about 190 events (selected within $\pm 2\sigma$ of the mass peak) with a signal to noise ratio equal to 1. The final D^+ sample has been selected with cuts to reduce reflections from the more copious Cabibbo favored modes and to optimize the signal to noise ratio, which is crucial for a reliable decay amplitude analysis. The Dalitz plot under analysis is shown in Fig. 6.1; the $K^+\pi^-$ and $\pi^+\pi^-$ invariant squared masses are reported on the x and y axes, respectively. From a simple visual inspection the Dalitz plot appears highly structured and two vector states are easily recognizable: a vertical one, at

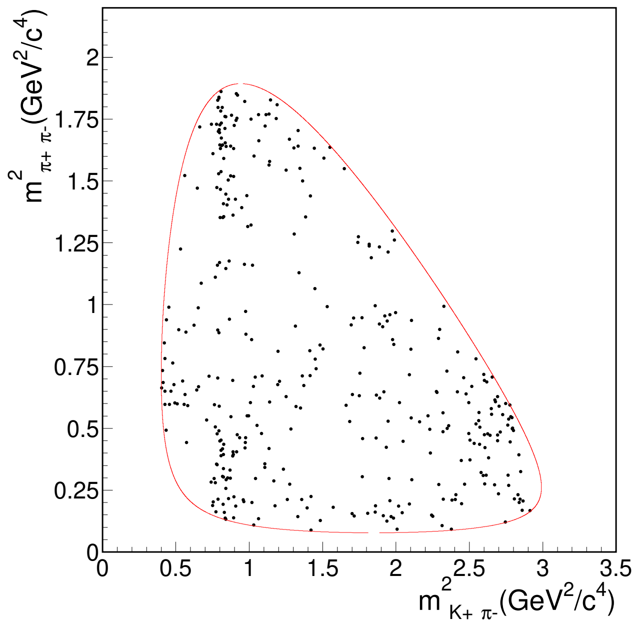

Figure 6.1: D^+ Dalitz plot in $K^+\pi^-$ and $\pi^+\pi^-$ squared mass contributions.

about 0.8 GeV^2/c^4, corresponding to $K^*(892)$, and a horizontal one, at about 0.6 GeV^2/c^4, corresponding to $\rho(770)$.

Before starting the fit of the Dalitz plot of Fig. 6.1, as already explained in Section 5.2.3, the reconstruction efficiency has to be evaluated. To do this, about 10 millions of $D^+ \to K^+\pi^+\pi^-$ MC events are generated; a four degree polynomial is found to be a good parametrization to fit the efficiency Dalitz plot. The function returned by the fit is shown in Fig. 6.2: it shows a rather smooth variation over the kinematic region, with a small decrease at the edges.

Then the background fit is performed. The sidebands cover the -5σ to -3σ and the $+3\sigma$ to $+5\sigma$ regions from the D^+ peak. They are chosen sufficiently far away from the signal region, not to include signal events, and sufficiently close to the D^+ peak, to well represent the signal background. It is however verified, changing the sideband regions, that the choice does not introduce bias in the final results. In Fig. 6.3 the signal and sideband regions for D^+ are highlighted, along with the signal region for D_s^+; the number of sideband events is 179. The Dalitz plot of mass sidebands is fitted with a second degree polynomial plus a Breit-Wigner function for the resonance $\rho(770)$; in Fig. 6.4 the Dalitz plot and the fit result are shown. The background fit function is able to well describe the reflections in the sidebands; according to the studies performed about the reflections in Section 3.2.2, it can be

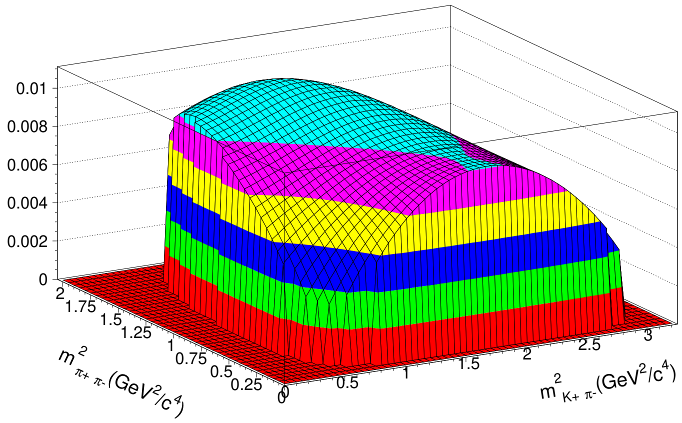

Figure 6.2: Efficiency fit function for $D^+ \to K^+\pi^+\pi^-$.

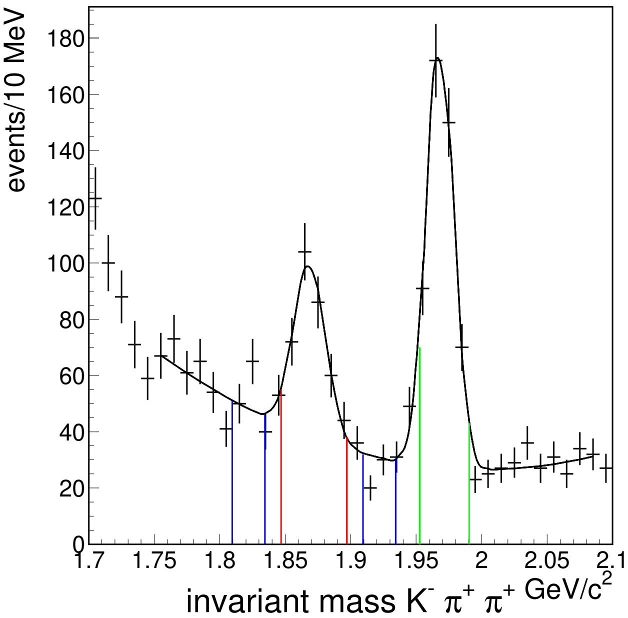

Figure 6.3: Invariant mass distribution $K^+\pi^+\pi^-$ for D^+; the red region corresponds to the signal events, the blue regions to the sidebands and the green one represents the D_s^+ signal.

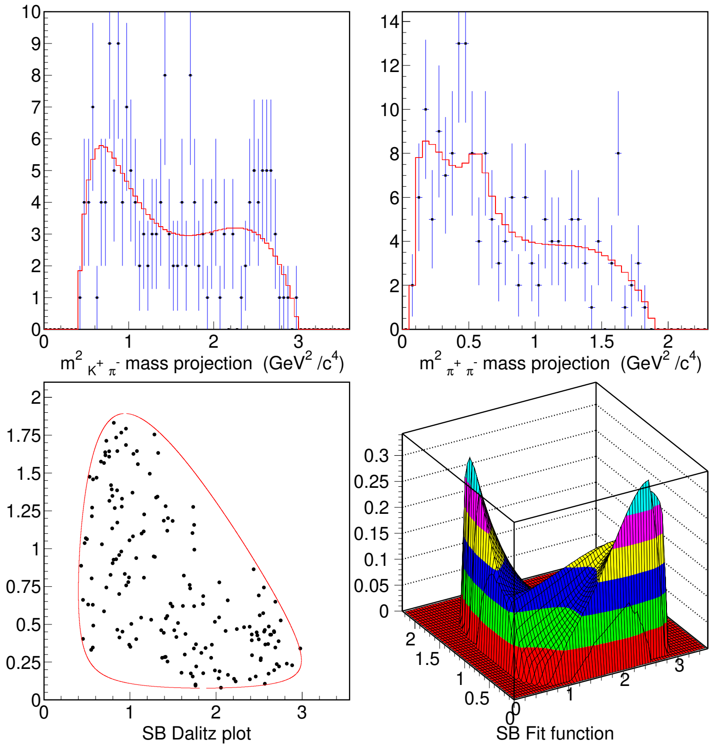

Figure 6.4: Fit to sidebands for D^+. At the top of the figure there are the projections of the data and, superimposed, the result of the fit. At the bottom the Dalitz plot of the sideband events and the fit function are shown.

assumed that this function adequately represents the reflections in the signal regions.

It is then possible to proceed to the fit of the Dalitz plot of Fig. 6.1. The resonant states, which can contribute to the decay dynamics, initially taken into account, are listed in Table 6.1. They are all the known and well established $K^+\pi^-$ and $\pi^+\pi^-$ resonances, as reported in the PDG[5]. Also a flat non-resonant contribution accounting for the direct decay of the D meson into three-body final states is considered in the initial set. The model of each resonance and the corresponding projections on the axes are shown in Appendix B, from Fig. B.1 to Fig. B.9.

The $f_0(980)$ parametrization is inferred from the FOCUS $D_s^+ \to \pi^+\pi^-\pi^+$ channel, where the $f_0(980)$ is the dominant component. When a proper Flatté form is used in the $D_s^+ \to \pi^+\pi^-\pi^+$ decay, the mass and couplings for the $f_0(980)$ (see Eq. 5.23) are $m_{f_0} = 957 \pm 8$ MeV$/c^2$, $\mathrm{g}_\pi = 0.2 \pm 0.03$ and $\mathrm{g}_K = 0.5 \pm 0.2$. When a very simple single Breit-Wigner approximation is used, mass and width are $m_{f_0} = 972 \pm 2$ MeV$/c^2$ and $\Gamma_{f_0} = 59 \pm 4$ MeV. Both forms have been tried in this analysis. The results of the initial fit, obtained including all the possible resonances, are reported

$K\pi$ resonances				
resonance	m (MeV/c^2)	Γ(MeV)	spin	decay fraction
$K^*(892)$	896.1 ± 0.27	50.7 ± 0.6	1 (vector)	$\sim 100\%$
$K^*(1410)$	1414 ± 15	232 ± 21	1 (vector)	$6.6 \pm 1.3\%$
$K_0^*(1430)$	1412 ± 6	294 ± 23	0 (scalar)	$93 \pm 10\%$
$K_2^*(1430)$	1432.4 ± 1.3	109 ± 5	2 (tensor)	$49.9 \pm 1.2\%$
$K^*(1680)$	1717 ± 27	322 ± 110	1 (vector)	$38.7 \pm 2.5\%$

(a)

$\pi\pi$ resonances				
resonance	m (MeV/c^2)	Γ(MeV)	spin	decay fraction
$\rho(770)$	768.5 ± 1.1	150.7 ± 2.9	1 (vector)	$\sim 100\%$
$f_0(980)$	980 ± 10	$40 - 100$	0 (scalar)	dominant
$f_2(1270)$	1275.4 ± 1.2	$185^{+3.5}_{-2.6}$	2 (tensor)	$84.8^{+2.5}_{-1.3}\%$
$\rho(1450)$	1465 ± 25	310 ± 60	1 (vector)	seen

(b)

Table 6.1: Possible resonant states considered in the fit procedure, from PDG.

in Tables 6.2 and 6.3, respectively when the Flatté and the single Breit-Wigner parametrizations are used for the $f_0(980)$. The projections of the data on the two invariant mass squared $m^2_{K\pi}$ and $m^2_{\pi\pi}$, with superimposed the result of the fit, are shown in Fig. 6.5 and in Fig. 6.6. Not all the states reported in the Tables 6.2 and 6.3 give significant contributions; the selection criterion chosen to achieve the actual set of resonances consists of several successive steps in order to eliminate contributions whose effects on the fit are marginal. Contributions are removed if their amplitude coefficients are less than $3\,\sigma$ significant and the fit confidence level increases due to the decreased number of degrees of freedom in the fit. Once the minimal set of parameters is determined, addition of each single contribution previously eliminated is reinstated to verify if the C.L. improves; in this case the contribution is added in the final set. Following this strategy, the final set of resonances is found to consist of four states, as reported in Tables 6.4 and 6.5, for the two different $f_0(980)$ forms. The projections of the data on the two invariant mass squared, with superimposed the result of the fit, are shown in Fig. 6.7 and in Fig. 6.8. Comparing these results, it can be seen that the low statistics $f_0(980)$ contribution is not such to distinguish between the two parametrizations, unlike in the $D_s^+ \to \pi^+\pi^-\pi^+$ decay, where the Flatté formula strongly improves the final fit quality. Final results for $K^+\pi^-\pi^+$ are then reported with the simpler single Breit-Wigner form.

Decay channel	Fit fraction (%)	Phase (degrees)	Coefficient
NR	13.75 ± 8.09	-8.6 ± 19.2	0.526 ± 0.153
$\rho(770)K^+$	49.72 ± 9.47	$0(fixed)$	$1(fixed)$
$K^*(892)\pi^+$	45.76 ± 6.20	-151.0 ± 13.3	0.959 ± 0.134
$f_0(980)K^+$	8.90 ± 4.85	80.3 ± 24.7	0.423 ± 0.134
$f_2(1270)K^+$	0.03 ± 0.25	-127.1 ± 222.0	0.026 ± 0.097
$K^*(1410)\pi^+$	16.22 ± 12.54	146.5 ± 24.9	0.571 ± 0.240
$K_0^*(1430)\pi^+$	1.38 ± 3.55	78.6 ± 57.8	0.166 ± 0.210
$K_2^*(1430)\pi^+$	5.27 ± 3.28	-32.5 ± 26.8	0.326 ± 0.109
$\rho(1450)K^+$	8.06 ± 4.13	-102.7 ± 22.4	0.403 ± 0.113
$K^*(1680)\pi^+$	23.93 ± 12.98	11.1 ± 19.5	0.694 ± 0.227

Table 6.2: Fit results with the complete set of states, with the $f_0(980)$ parametrized as a Flatté function.

Decay channel	Fit fraction (%)	Phase (degrees)	Coefficient
NR	10.42 ± 7.48	-10.3 ± 24.2	0.455 ± 0.156
$\rho(770)K^+$	50.22 ± 10.00	$0(fixed)$	$1(fixed)$
$K^*(892)\pi^+$	46.07 ± 7.06	-148.7 ± 14.8	0.958 ± 0.141
$f_0(980)K^+$	7.65 ± 4.32	70.4 ± 27.1	0.390 ± 0.125
$f_2(1270)K^+$	0.02 ± 0.23	-150.1 ± 286.9	0.020 ± 0.115
$K^*(1410)\pi^+$	13.86 ± 12.22	146.2 ± 24.1	0.525 ± 0.247
$K_0^*(1430)\pi^+$	1.27 ± 3.52	61.6 ± 70.2	0.159 ± 0.216
$K_2^*(1430)\pi^+$	5.37 ± 3.36	-36.6 ± 29.9	0.327 ± 0.115
$\rho(1450)K^+$	8.17 ± 4.64	-101.4 ± 23.5	0.403 ± 0.114
$K^*(1680)\pi^+$	19.75 ± 12.64	11.0 ± 20.4	0.627 ± 0.237

Table 6.3: Fit results with the complete set of states, with the $f_0(980)$ parametrized as a single-channel resonance.

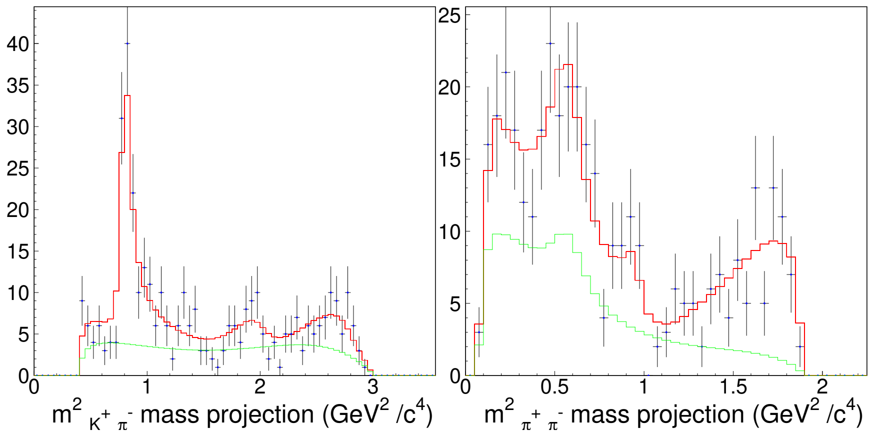

Figure 6.5: Results of the initial fit, with $f_0(980)$ parametrized as a Flatté function, on the two invariant mass squared projections $m^2_{K\pi}$ and $m^2_{\pi\pi}$: in black the data, in red superimposed the result of the fit, in green the result of the background fit.

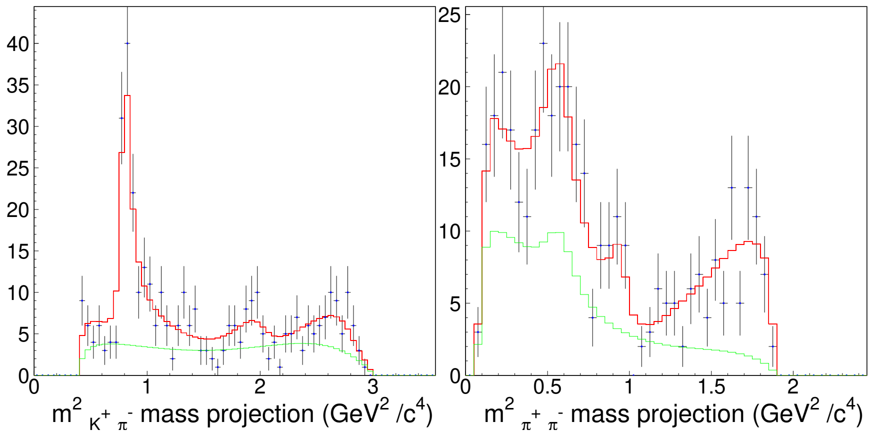

Figure 6.6: Results of the initial fit, with $f_0(980)$ parametrized as a single-channel Breit-Wigner, on the two invariant mass squared projections $m^2_{K\pi}$ and $m^2_{\pi\pi}$: in black the data, in red superimposed the result of the fit, in green the result of the background fit.

Decay channel	Fit fraction (%)	Phase (degrees)	Coefficient
$\rho(770)K^+$	35.82 ± 7.44	$0(fixed)$	$1(fixed)$
$K^*(892)\pi^+$	52.44 ± 6.58	-167.7 ± 14.5	1.210 ± 0.182
$f_0(980)K^+$	11.69 ± 3.62	-127.1 ± 25.1	0.571 ± 0.118
$K_2^*(1430)\pi^+$	7.76 ± 3.62	59.7 ± 35.1	0.466 ± 0.132

Table 6.4: Final fit results for D^+, with the $f_0(980)$ parametrized as a Flatté function.

Decay channel	Fit fraction (%)	Phase (degrees)	Coefficient
$\rho(770)K^+$	39.43 ± 7.87	$0(fixed)$	$1(fixed)$
$K^*(892)\pi^+$	52.20 ± 6.84	-167.1 ± 14.4	1.151 ± 0.173
$f_0(980)K^+$	8.92 ± 3.33	-134.5 ± 31.4	0.476 ± 0.111
$K_2^*(1430)\pi^+$	8.03 ± 3.72	54.4 ± 38.3	0.451 ± 0.125

Table 6.5: Final fit results for D^+, with $f_0(980)$ parametrized as a single-channel Breit-Wigner.

The two dominant modes are the vector resonances $\rho(770)$ and $K^*(892)$, as supposed after the visual inspection of the Dalitz plot of Fig. 6.1, which account for about 90% of the D^+ decay fraction. Their relative phase difference of about 180° suggests a marginal role of final state interactions in this decay. The clear emptinesses in the low $m^2_{K\pi}$ and low $m^2_{\pi\pi}$ region, at the crossing of the two vector bands, suggests a destructive interference effect[1]. The C.L. of the Dalitz plot fit is 9.2% and the corresponding adaptive binning scheme is shown in Fig. 6.9. Comparing the decay fractions, reported in Table 6.1, of the two possible states in $K\pi$ at about 1430 GeV, and looking at the two different spins, the presence of the tensor $K_2^*(1430)$, while the scalar $K_0^*(1430)$ is absence, seems a bit suspicious. However it is justified by the three-lobe helicity structure visible in the D^+ Dalitz plot. Further investigations would required higher statistics. The band of events at about (1 GeV$/c^2)^2$ in the $m^2_{\pi^+\pi^-}$ mass combination indicates the presence of the scalar $f_0(980)$ in the decay at a four sigma significance level. It is nevertheless interesting to observe that the DCS decay $D^+ \to K^+\pi^+\pi^-$ is dominated by vector resonances with no major role of rescattering effects.

6.1.2 Systematic error evaluation

The systematic errors are evaluated following the same strategy used in the branching ratio measurements, defining a *split sample* and a *fit variant* component. The

[1]It has been carefully checked that this effect is not due to efficiency or background problems.

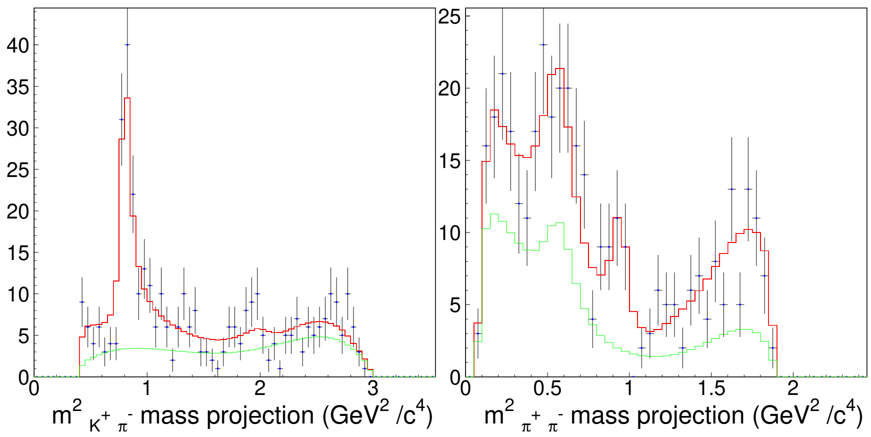

Figure 6.7: Results of the final fit, with $f_0(980)$ parametrized as a Flatté function, on the two invariant mass squared projections $m^2_{K\pi}$ and $m^2_{\pi\pi}$: in black the data, in red superimposed the result of the fit, in green the result of the background fit.

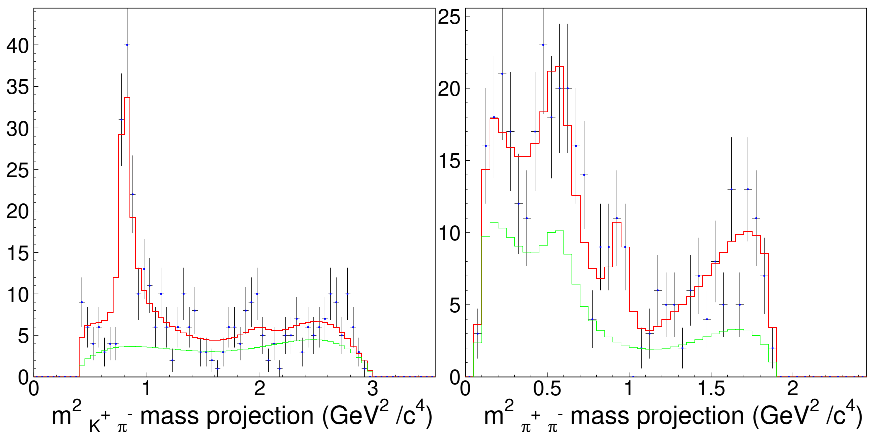

Figure 6.8: Results of the final fit on the two invariant mass squared projections $m^2_{K\pi}$ and $m^2_{\pi\pi}$, with $f_0(980)$ parametrized as a single-channel Breit-Wigner: in black the data, in red superimposed the result of the fit, in green the result of the background fit.

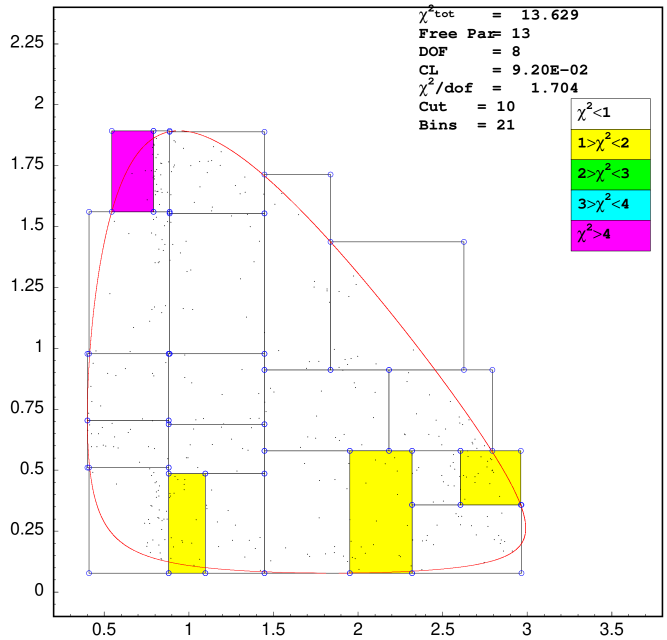

Figure 6.9: Adaptive binning scheme for the final fit of D^+.

methods to calculated these errors are sketched out in appendix A. The *split sample* and *fit variant* contributions are then added in quadrature to obtain the final systematic errors.

Split samples

Due to the limited statistics of the sample and to the difficult to perform a Dalitz plot analysis on few events, the split sample component is evaluated dividing the full data set in 2 subsamples. Three different split criteria are considered: the D momentum range, the D signum and a different choice of selection cuts, which divides the sample in approximately two comparable subsamples, named high/low purity criterion. This last component is evaluated to investigate the possible cut modeling effects. The cuts applied to obtain the high purity sample are $L/\sigma > 26$, $\Delta W_K > 6$ and $\Delta W_{\pi^-} > 5$; the low purity sample is the complementary one. The run 96-97 criterion is not taken into account due to the low statistics, because, following this principle, the full data set is divided in two different subsamples, one with a statistics of about 1/3, the other with a statistics of about 2/3.

Once the χ^2/d.o.f. in these three different cases is evaluated, the split sample errors, which are added to the fit variant ones, are those coming from the split samples with the highest χ^2. In Table 6.6 the resulting χ^2 are reported; the dominant contribution comes from the high/low momentum split. In Table 6.7 the results of the fit on the low and high momentum samples are shown and in Table 6.8 the

Split criteria	χ^2/d.o.f.
Momentum	3.2
Signum	0.9
High/low purity	0.6

Table 6.6: χ^2 from the split samples for D^+.

Decay channel	Fit fraction (%)	Phase (degrees)	Coefficient
Low momentum split			
$\rho(770)K^+$	48.06 ± 9.91	$0(fixed)$	$1(fixed)$
$K^*(892)\pi^+$	32.37 ± 7.82	-127.9 ± 31.6	0.821 ± 0.162
$f_0(980)K^+$	4.42 ± 3.36	172.4 ± 40.6	0.303 ± 0.130
$K_2^*(1430)\pi^+$	15.94 ± 5.34	33.4 ± 24.3	0.576 ± 0.125
High momentum split			
$\rho(770)K^+$	37.13 ± 9.48	$0(fixed)$	$1(fixed)$
$K^*(892)\pi^+$	57.49 ± 8.51	-166.5 ± 17.9	1.244 ± 0.228
$f_0(980)K^+$	5.04 ± 3.57	28.1 ± 47.8	0.369 ± 0.152
$K_2^*(1430)\pi^+$	6.20 ± 4.47	174.5 ± 48.8	0.409 ± 0.179

Table 6.7: Results for the momentum split sample for D^+.

Split sample errors			
Decay channel	Fit fraction (%)	Phase (degrees)	Coefficient
$\rho(770)K^+$	6.82	0	0
$K^*(892)\pi^+$	6.10	23.0	0.141
$f_0(980)K^+$	3.53	39.9	0.116
$K_2^*(1430)\pi^+$	3.87	0	0.128

Table 6.8: Split sample errors for D^+, from high/low momentum.

followed systematic errors are reported.

Fit variant

The fit variant component is computed by varying the fitting conditions on the whole data set. A possible source of systematic error is the assumption that the shape of the background in the sideband is a good representation of the background in the signal region. To take into account this effect the background parametrization is changed. In particular, for the D^+ analysis, a fit without the $\rho(770)$ in the background is

Decay channel	Fit fraction (%)	Phase (degrees)	Coefficient
$\rho(770)K^+$	45.73 ± 7.94	$0(fixed)$	$1(fixed)$
$K^*(892)\pi^+$	49.55 ± 6.96	-164.5 ± 13.4	1.041 ± 0.151
$f_0(980)K^+$	5.90 ± 3.31	-152.4 ± 35.6	0.359 ± 0.118
$K_2^*(1430)\pi^+$	8.81 ± 3.59	24.8 ± 29.4	0.439 ± 0.106

Table 6.9: Results for the fit variant for D^+.

Fit variant errors			
Decay channel	Fit fraction (%)	Phase (degrees)	Coefficient
$\rho(770)K^+$	4.45	0	0
$K^*(892)\pi^+$	1.88	1.8	0.078
$f_0(980)K^+$	2.14	12.7	0.082
$K_2^*(1430)\pi^+$	0.55	20.9	0.087

Table 6.10: Fit variant errors for D^+.

performed. In Table 6.9 the fit results are shown. The corresponding systematic errors are reported in Table 6.10.

The global systematic errors are obtained adding in quadrature the previous components; the results are summarized in Table 6.11.

6.1.3 Final results

The final results for the Dalitz plot analysis of $D^+ \to K^+\pi^-\pi^+$ are reported in Table 6.12.

An amplitude analysis of this decay has been previously performed by the E791 experiment [43]. They describe the decay with two resonant channels, $\rho(770)K^+$ and $K^*(892)\pi^+$, plus a uniform non-resonant component, each accounting for about 1/3 of the decay fraction, as shown in Table 6.13. In the present analysis the non-resonant contribution seems to be better resolved in additional resonant channels. The E791 $\rho(770)/K^*(892)$ relative phase difference is about $0°$, while the measurement reported in this thesis is close to $180°$. This difference can not be attribute to different choices of the helicity angle, because this relative phase difference is free of phase convention ambiguity, due to the vector nature of the two resonances. To compare directly the results, a fit with the same components as E791 is performed; the results are shown in Fig. 6.10 and in Table 6.14. The disagreement in the $\rho(770)/K^*(892)$ relative phase is still confirmed.

Decay channel		Fit var. error	Split sample error	Total sys. error
$\rho(770)K^+$	Fit fraction (%)	4.45	6.82	8.15
	Phase (degrees)	0	0	0
	Coefficient	0	0	0
$K^*(892)\pi^+$	Fit fraction (%)	1.88	6.1	6.38
	Phase (degrees)	1.8	23.0	23.0
	Coefficient	0.078	0.141	0.161
$f_0(980)K^+$	Fit fraction (%)	2.14	3.53	4.12
	Phase (degrees)	12.7	39.9	41.9
	Coefficient	0.082	0.116	0.143
$K_2^*(1430)\pi^+$	Fit fraction (%)	0.55	3.87	3.91
	Phase (degrees)	20.9	0.	20.9
	Coefficient	0.087	0.128	0.129

Table 6.11: Total systematic errors for D^+.

Decay channel	Fit fraction (%)	Phase (degrees)	Coefficient
$\rho(770)K^+$	$39.43 \pm 7.87 \pm 8.15$	$0(fixed)$	$1(fixed)$
$K^*(892)\pi^+$	$52.20 \pm 6.84 \pm 6.38$	$-167.1 \pm 14.4 \pm 23.0$	$1.151 \pm 0.173 \pm 0.161$
$f_0(980)K^+$	$8.92 \pm 3.33 \pm 4.12$	$-134.5 \pm 31.4 \pm 41.9$	$0.476 \pm 0.111 \pm 0.143$
$K_2^*(1430)\pi^+$	$8.03 \pm 3.72 \pm 3.91$	$54.4 \pm 38.3 \pm 20.9$	$0.451 \pm 0.125 \pm 0.129$

Table 6.12: Final fit results for D^+.

Decay channel	Fit fraction (%)	Phase (degrees)
$\rho(770)K^+$	37 ± 14	115 ± 23
$K^*(892)\pi^+$	35 ± 14	103 ± 29
NR	36 ± 14	$0(fixed)$

Table 6.13: Fit results for D^+ obtained by the E791 experiment.

Decay channel	Fit fraction (%)	Phase (degrees)
$\rho(770)K^+$	44.52 ± 5.81	$0(fixed)$
$K^*(892)\pi^+$	43.78 ± 5.00	147.1 ± 13.0
NR	15.60 ± 4.56	75.3 ± 12.9

Table 6.14: Fit results for D^+ with the same mixture of resonances as those of E791 experiment.

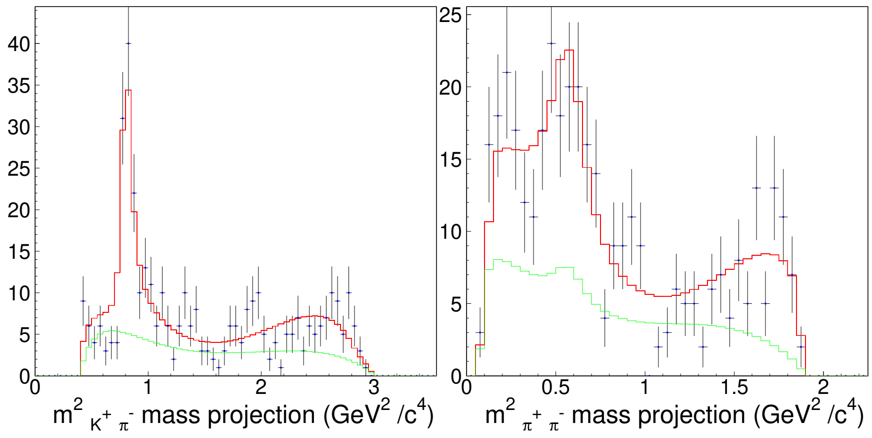

Figure 6.10: Results of the fit performed with the same mixture of resonances as done in the E791 experiment.

6.2 $D_s^+ \to K^+\pi^-\pi^+$

6.2.1 Fit strategy

The Dalitz plot analysis of the singly Cabibbo suppressed decay $D_s^+ \to K^+\pi^-\pi^+$ follows the same strategy and steps as the $D^+ \to K^+\pi^-\pi^+$ analysis. It is performed with a sample of about 570 events, with a signal to noise ratio equal to 2.4; the Dalitz plot under study is shown in Fig. 6.11. Unlike the Dalitz plot of D^+, the D_s^+ channel presents a much more complex events distribution over all the phase-space together with $\rho(770)$ and $K^*(892)$, whose main characteristics are still visible.

The efficiency is evaluated generating about 10 millions of $D_s^+ \to K^+\pi^-\pi^+$ MC events; the fit function is a four degree polynomial, as for D^+, and it is shown in Fig. 6.12.

The sideband regions are chosen to cover the -5σ to -3σ and the $+4\sigma$ to $+6\sigma$ regions from the D_s^+ peak. Also for the D_s analysis it is verified that different choices of the sideband regions do not affect the final results. In Fig. 6.13 the signal and sideband regions for D_s^+ are highlighted, along with the signal region for D^+; the number of sideband events is 180. The fit function which better describes the Dalitz plot of mass sidebands is a second degree polynomial plus a Breit-Wigner function for the resonance $K^*(892)$; in Fig. 6.14 the Dalitz plot and the fit result are shown.

To fit the Dalitz plot of Fig. 6.11, the resonant states initially taken into account are the same as those used for the D^+ and are listed in Table 6.1. The model of each

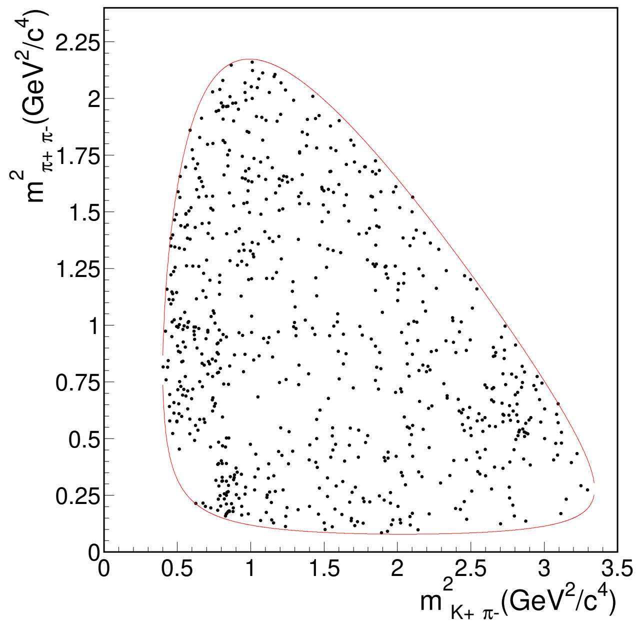

Figure 6.11: D_s^+ Dalitz plot in $K^+\pi^-$ and $\pi^+\pi^-$ squared mass contributions.

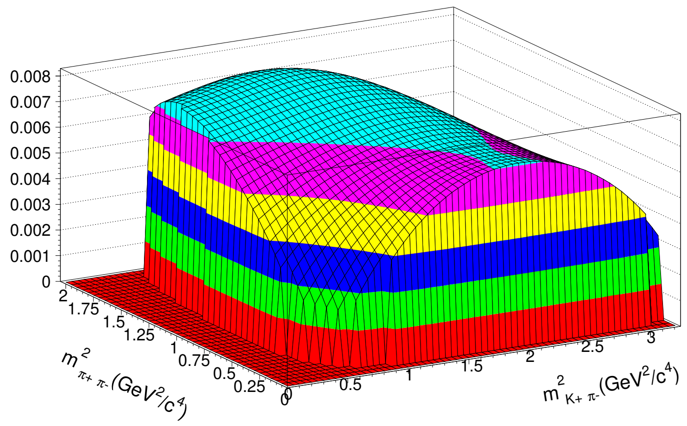

Figure 6.12: Efficiency fit function for $D_s^+ \to K^+\pi^+\pi^-$.

resonance and the corresponding projections on the axes are shown in Appendix B, from Fig. B.10 to Fig. B.18. The fit results, starting with the complete set of resonances, are reported in Table 6.15 and shown in Fig. 6.15. Following the same procedure used for the D^+, the final set of resonances is determined and it is reported in Table 6.16. The results of the fit on the two invariant mass squared projections

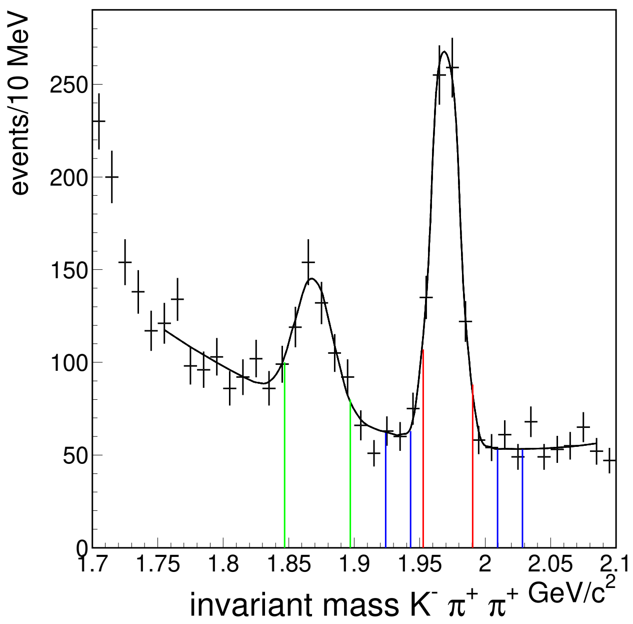

Figure 6.13: Invariant mass distribution $K^+\pi^+\pi^-$ for D_s^+; the red region corresponds to the signal events, the blue regions to the sidebands and the green one represents the D^+ signal.

Decay channel	Fit fraction (%)	Phase (degrees)	Coefficient
NR	17.05 ± 5.51	54.9 ± 10.6	0.785 ± 0.190
$\rho(770)K^+$	27.67 ± 7.00	$0(fixed)$	$1(fixed)$
$K^*(892)\pi^+$	21.62 ± 3.36	158.2 ± 10.7	0.884 ± 0.121
$f_0(980)K^+$	0.69 ± 0.65	−56.0 ± 33.7	0.158 ± 0.079
$f_2(1270)K^+$	1.65 ± 1.24	28.2 ± 21.2	0.244 ± 0.097
$K^*(1410)\pi^+$	4.40 ± 3.33	−2.8 ± 28.0	0.399 ± 0.168
$K_0^*(1430)\pi^+$	7.52 ± 5.20	31.9 ± 22.6	0.521 ± 0.166
$K_2^*(1430)\pi^+$	1.24 ± 1.10	108.5 ± 24.5	0.212 ± 0.103
$\rho(1450)K^+$	6.34 ± 3.06	−159.3 ± 19.4	0.479 ± 0.123
$K^*(1680)\pi^+$	8.27 ± 6.56	−43.9 ± 23.1	0.547 ± 0.267

Table 6.15: Fit results with the complete set of states for D_s^+.

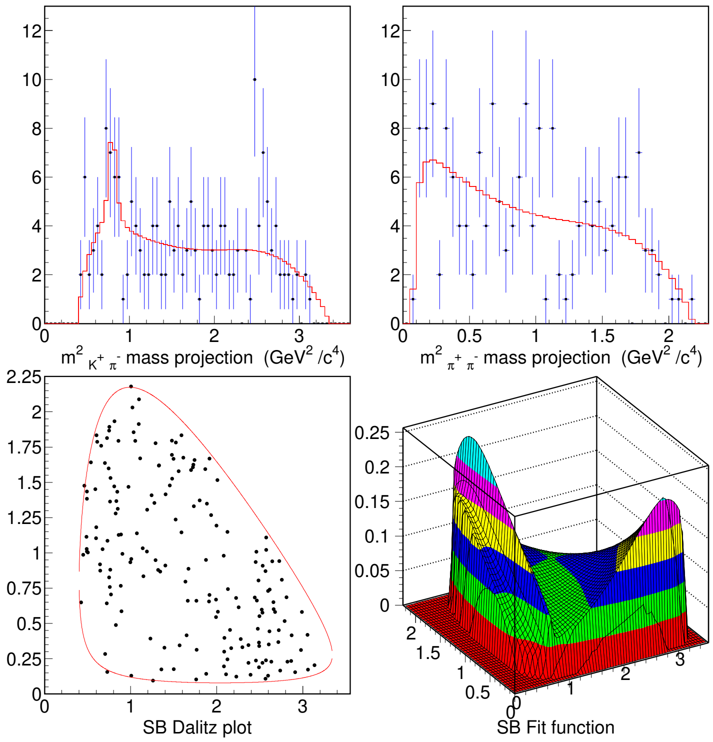

Figure 6.14: Fit to sidebands for D_s^+. At the top of the figure there are the projections of the data and, superimposed, the result of the fit. At the bottom the Dalitz plot of the sideband events and the fit function are shown.

Decay channel	Fit fraction (%)	Phase (degrees)	Coefficient
NR	15.88 ± 4.92	43.1 ± 10.4	0.640 ± 0.118
$\rho(770)K^+$	38.83 ± 5.31	$0(fixed)$	$1(fixed)$
$K^*(892)\pi^+$	21.64 ± 3.21	161.7 ± 8.6	0.747 ± 0.080
$K^*(1410)\pi^+$	18.82 ± 4.03	−34.8 ± 12.1	0.696 ± 0.097
$K_0^*(1430)\pi^+$	7.65 ± 5.00	59.3 ± 19.5	0.444 ± 0.141
$\rho(1450)K^+$	10.62 ± 3.51	−151.7 ± 11.1	0.523 ± 0.091

Table 6.16: Final fit results for D_s^+.

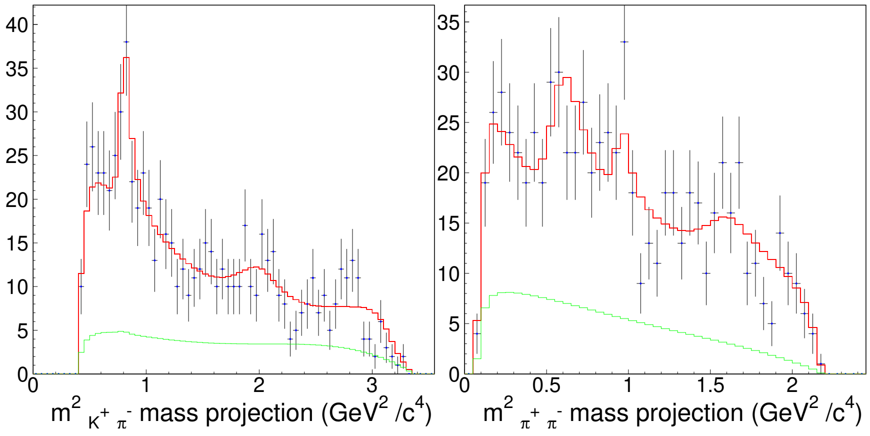

Figure 6.15: Results of the initial fit on the two invariant mass squared projections $m^2_{K\pi}$ and $m^2_{\pi\pi}$: in black the data, in red superimposed the result of the fit, in green the result of the background fit.

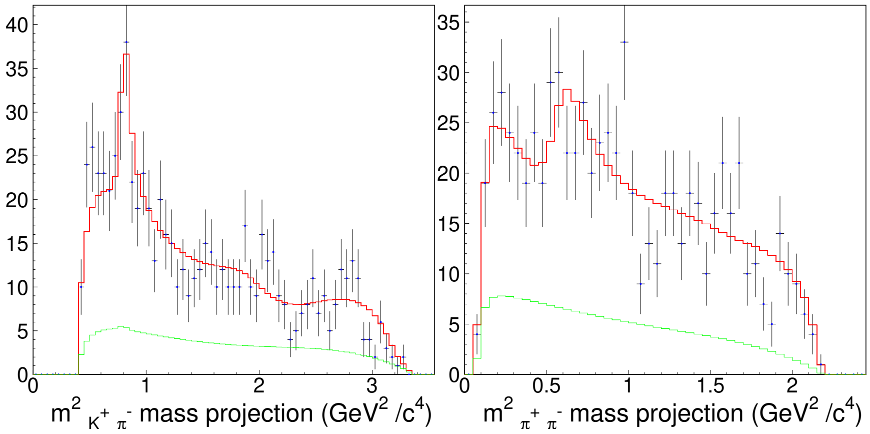

Figure 6.16: Results of the final fit on the two invariant mass squared projections $m^2_{K\pi}$ and $m^2_{\pi\pi}$: in black the data, in red superimposed the result of the fit, in green the result of the background fit.

$m^2_{K\pi}$ and $m^2_{\pi\pi}$ are shown in Fig. 6.16. The $\rho(770)$ and $K^*(892)$ vector resonances have a similar behaviour as in the DCSD: represent the major contributions (cover about 60% of the decay fraction) and their relative phase difference is close to 180°, suggesting a marginal role of FSI in this channel. The depletion of events between the two states (visible at the cross of the bands in Fig. 6.11) suggests a destructive interference effect among the two vector resonances. The description of the event intensity all over the Dalitz plot requires three additional higher mass resonances, two in $K^+\pi^-$ and one in $\pi^+\pi^-$, and a non-resonant term. More precisely

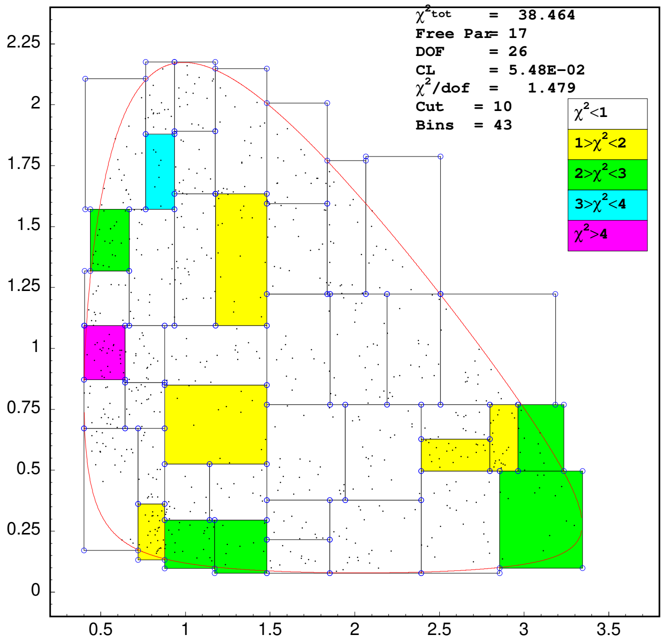

Figure 6.17: Adaptive binning scheme for the final fit of D_s^+.

the two $K^+\pi^-$ states are the scalar $K_0^*(1430)$ and the vector $K^*(1410)$, which are the lowest mass resonances besides the $K^*(892)$, and the $\pi^+\pi^-$ state is $\rho(1450)$, which is the second vector state in the ρ series. They account for a 30–40% resonant portion of the decay; a non-resonant contribution of about 15% completes the event description for this channel. The fit C.L. for the mixture of states selected is 5.5% and the corresponding adaptive binning scheme is shown in Fig. 6.17. This solution satisfactory reproduces the main features of the decay, as indicated by the C.L., and shown in the two invariant mass squared projections in Fig. 6.16. However the absence of the $f_0(980)$ in the fit is a bit suspicious; an accumulation of events at $(1\ \mathrm{GeV}/c^2)^2$ $\pi^+\pi^-$ mass squared, to some extent visually recognizable in the Dalitz plot, would indeed suggest its selection in the resonance final set. On the other hand the isobar model is too naive to describe more complex decays dynamics, which intervenes in the presence of the $K^+\pi^-$ and $\pi^+\pi^-$ S-waves states. Improvements will be possible at higher statistics, when more rigorous treatments, such as that based on the *K-matrix* model, will be necessary.

6.2.2 Systematic error evaluation

Split samples

The split criteria are the same adopted in the D^+ analysis: the D momentum range, the D signum and the high/low purity. The high purity sample is selected with $L/\sigma > 20$, $\Delta W_K > 5$, $\Delta W_{\pi^-} > 4$. In Table 6.17 the χ^2/d.o.f evaluated in these

Split criteria	χ^2/d.o.f.
Momentum	1.2
Signum	0.8
High/low purity	0.6

Table 6.17: χ^2 from the split samples for D_s^+.

Decay channel	Fit fraction (%)	Phase (degrees)	Coefficient
Low momentum split			
NR	15.41 ± 7.14	50.0 ± 19.7	0.612 ± 0.166
$\rho(770)K^+$	41.12 ± 9.26	$0(fixed)$	$1(fixed)$
$K^*(892)\pi^+$	17.61 ± 4.57	171.9 ± 13.6	0.655 ± 0.113
$K^*(1410)\pi^+$	13.12 ± 6.74	−47.6 ± 16.7	0.565 ± 0.163
$K_0^*(1430)\pi^+$	12.40 ± 8.09	57.8 ± 32.3	0.549 ± 0.174
$\rho(1450)K^+$	15.23 ± 6.07	−135.6 ± 15.0	0.609 ± 0.122
High momentum split			
NR	14.22 ± 6.27	40.9 ± 14.1	0.618 ± 0.163
$\rho(770)K^+$	37.21 ± 6.41	$0(fixed)$	$1(fixed)$
$K^*(892)\pi^+$	25.08 ± 4.56	157.1 ± 10.8	0.821 ± 0.113
$K^*(1410)\pi^+$	23.00 ± 5.43	−19.0 ± 19.6	0.786 ± 0.129
$K_0^*(1430)\pi^+$	3.25 ± 4.90	54.6 ± 34.8	0.296 ± 0.215
$\rho(1450)K^+$	7.80 ± 3.81	−164.3 ± 17.6	0.458 ± 0.120

Table 6.18: Results for the momentum split sample for D_s^+.

three different cases are reported; the main contribution comes from the high/low momentum split. In Table 6.18 the results of the fit on the low and high momentum samples are shown and in Table 6.19 the followed systematic errors are reported.

Fit variant

To evaluate the fit variant systematics, the background parametrization is changed; more precisely, the background fit is performed with a first degree polynomial plus the $K^*(892)$ and then with a constant function (zero degree polynomial) plus the $K^*(892)$. In Table 6.20 the results of these two different fits are shown and the systematic errors obtained are reported in Table 6.21.

Adding the previous components the global systematic errors are calculated; the results are summarized in Table 6.22.

Split sample errors			
Decay channel	Fit fraction (%)	Phase (degrees)	Coefficient
NR	1.04	4.4	0.024
$\rho(770)K^+$	1.60	0	0
$K^*(892)\pi^+$	1.11	2.2	0.027
$K^*(1410)\pi^+$	1.0	3.7	0.024
$K_0^*(1430)\pi^+$	0.5	8.0	0
$\rho(1450)K^+$	0	4.2	0

Table 6.19: Split sample errors for D_s^+, from high/low momentum.

Decay channel	Fit fraction (%)	Phase (degrees)	Coefficient
First degree polynomial			
NR	17.80 ± 4.77	43.5 ± 7.1	0.657 ± 0.113
$\rho(770)K^+$	41.22 ± 4.85	$0(fixed)$	$1(fixed)$
$K^*(892)\pi^+$	22.20 ± 2.95	161.4 ± 5.8	0.734 ± 0.072
$K^*(1410)\pi^+$	20.10 ± 3.52	−32.0 ± 10.3	0.698 ± 0.086
$K_0^*(1430)\pi^+$	4.57 ± 3.90	73.2 ± 15.9	0.333 ± 0.134
$\rho(1450)K^+$	12.69 ± 3.22	−153.8 ± 9.1	0.555 ± 0.078
Zero degree polynomial			
NR	17.85 ± 4.98	44.0 ± 9.5	0.645 ± 0.115
$\rho(770)K^+$	42.95 ± 5.11	$0(fixed)$	$1(fixed)$
$K^*(892)\pi^+$	22.01 ± 3.07	161.4 ± 8.5	0.716 ± 0.074
$K^*(1410)\pi^+$	20.04 ± 3.48	−30.6 ± 11.2	0.683 ± 0.085
$K_0^*(1430)\pi^+$	5.27 ± 4.33	79.8 ± 15.3	0.350 ± 0.138
$\rho(1450)K^+$	11.59 ± 3.22	−154.5 ± 11.2	0.519 ± 0.076

Table 6.20: Results for the fit variant for D_s^+.

Fit variant errors			
Decay channel	Fit fraction (%)	Phase (degrees)	Coefficient
NR	1.12	0.4	0.009
$\rho(770)K^+$	2.06	0	0
$K^*(892)\pi^+$	0.28	0.2	0.015
$K^*(1410)\pi^+$	0.7	2.2	0.008
$K_0^*(1430)\pi^+$	1.6	10.5	0.060
$\rho(1450)K^+$	1.04	1.4	0.020

Table 6.21: Fit variant errors for D_s^+.

Decay channel		Fit var. error	Split sample error	Total sys. error
NR	Fit fraction (%)	1.12	1.04	1.53
	Phase (degrees)	0.4	4.4	4.4
	Coefficient	0.009	0.024	0.026
$\rho(770)K^+$	Fit fraction (%)	2.06	1.60	2.61
	Phase (degrees)	0	0	0
	Coefficient	0	0	0
$K^*(892)\pi^+$	Fit fraction (%)	0.28	1.11	1.14
	Phase (degrees)	0.2	2.2	2.2
	Coefficient	0.015	0.027	0.031
$K^*(1410)\pi^+$	Fit fraction (%)	0.7	1.0	1.22
	Phase (degrees)	2.2	3.7	4.3
	Coefficient	0.008	0.024	0.025
$K_0^*(1430)\pi^+$	Fit fraction (%)	1.6	0.5	1.70
	Phase (degrees)	10.5	8.0	13.2
	Coefficient	0.060	0	0.060
$\rho(1450)K^+$	Fit fraction (%)	1.04	0	1.04
	Phase (degrees)	1.4	4.2	4.4
	Coefficient	0.020	0	0.020

Table 6.22: Total systematic errors for D_s^+.

Decay channel	Fit fraction (%)	Phase (degrees)	Coefficient
NR	$15.88 \pm 4.92 \pm 1.53$	$43.1 \pm 10.4 \pm 4.4$	$0.640 \pm 0.118 \pm 0.026$
$\rho(770)K^+$	$38.83 \pm 5.31 \pm 2.61$	$0(fixed)$	$1(fixed)$
$K^*(892)\pi^+$	$21.64 \pm 3.21 \pm 1.14$	$161.7 \pm 8.6 \pm 2.2$	$0.747 \pm 0.080 \pm 0.031$
$K^*(1410)\pi^+$	$18.82 \pm 4.03 \pm 1.22$	$-34.8 \pm 12.1 \pm 4.3$	$0.696 \pm 0.097 \pm 0.025$
$K_0^*(1430)\pi^+$	$7.65 \pm 5.00 \pm 1.70$	$59.3 \pm 19.5 \pm 13.2$	$0.444 \pm 0.141 \pm 0.060$
$\rho(1450)K^+$	$10.62 \pm 3.51 \pm 1.04$	$-151.7 \pm 11.1 \pm 4.4$	$0.523 \pm 0.091 \pm 0.020$

Table 6.23: Final fit results for D_s^+.

6.2.3 Final results

The final results for the Dalitz plot analysis of $D_s^+ \to K^+\pi^-\pi^+$ are reported in Table 6.23. These results represent the first amplitude analysis for this channel.

The fit results have been obtained starting with a complete set of possible well-established resonances; the model is able to reproduce the main features of the D^+ and $D_s^+ \to K^+\pi^-\pi^+$ decays. However the isobar model fit of the $D^+ \to \pi^+\pi^-\pi^+$ [34] and of $D^+ \to K^-\pi^+\pi^+$ [55] have required the introduction of ad hoc resonances as $\sigma(600)$ and $\kappa(900)$ to obtain a good fit C.L., modelled as single Breit-Wigner functions. It has been verified if a possible fit improvement could be achieved including these states in the initial set of resonances. In both the analysis the $\sigma(600)$ and $\kappa(900)$ contributions are returned with a statistical significance of less then 1σ. The real improvement in the D^+ and $D_s^+ \to K^+\pi^-\pi^+$ analysis will be the application of the *K-matrix* approach, as done by the FOCUS collaboration in the three-pion analysis [2]. At this level of statistics this formalism is not viable, considering the large number of free parameters necessary to account for the simultaneous presence of both $\pi^+\pi^-$ and $K^+\pi^-$ resonances.

Conclusions

In this thesis the analysis of the doubly and singly Cabibbo suppressed decays D^+ and $D_s^+ \to K^+\pi^-\pi^+$ has been presented.

The suppressed nature of these channels has required a careful investigation of the possible contaminations from the more copious and favoured decays. The selection cuts have been chosen to reach a reasonable compromise between sufficiently high statistics, a good signal to noise ratio and negligible level of the reflections. The selected samples consist of 189 ± 24 events for the D^+, with S/N ~ 1, and 567 ± 31 for the D_s^+, with S/N ~ 2.5.

The branching ratios have been measured as:

$$\frac{\Gamma\left(D^+ \to K^+\pi^+\pi^-\right)}{\Gamma\left(D^+ \to K^-\pi^+\pi^+\right)} = 0.0065 \pm 0.0008 \pm 0.0004$$

and

$$\frac{\Gamma\left(D_s^+ \to K^+\pi^+\pi^-\right)}{\Gamma\left(D_s^+ \to K^+K^-\pi^+\right)} = 0.127 \pm 0.007 \pm 0.014$$

These measurements improve the statistical accuracy by approximately a factor of 2 and 5 with respect to previous determinations. In particular the comparison of $(1/\tan^4\theta_C) \times \Gamma(D^+_{\mathrm{DCS}})/\Gamma(D^+_{\mathrm{CF}}) = 2.60 \pm 0.32$ with the FOCUS lifetime ratio of $\tau(D^+)/\tau(D^0) = 2.538 \pm 0.023$ and the marginal role of FSI inferred by the D^+_{DCS} Dalitz plot analysis, presented in this thesis, supports the interpretation that destructive interference between spectator amplitudes with indistinguishable quarks in the CF D^+ final state is responsible for the lifetime difference between D^+ and D^0.

The amplitude analysis of D^+ and $D_s^+ \to K^+\pi^+\pi^-$ final states have also been performed. In both the decays the two vector states $K^*(892)$ and $\rho(770)$ have been measured as the dominant components, with a relative phase shift configuration almost real, suggesting a marginal role of FSI in these decays. An amplitude analysis of the DCSD has been previously performed by E791 experiment with a sample of $\sim$ 60 events. They have described the decay with an equal mixture of $K^*(892)$, $\rho(770)$ and a uniform non-resonant component; the higher statistics of the FOCUS data seems to allow a major sensitivity to distinguish between different contributions. The amplitude analysis of the $D_s^+ \to K^+\pi^+\pi^-$ presented in this thesis represents the first available measurement for this decay.

Bibliography

[1] J. M. Link *et al.* [FOCUS Collaboration], Phys. Lett. B **535**, 43 (2002).

[2] J. M. Link *et al.* [FOCUS Collaboration], Phys. Lett. B **585**, 200 (2004).

[3] S. Malvezzi, invited talk at 16th Conference on High Energy Physics (IFAE 2004), Turin, Italy, 14-16 Apr 2004. arXiv:hep-ex/0407039.

[4] D. Pedrini, invited talk at 24th International Conference on Physics in Collision (PIC 2004), Boston, Massachusetts, 27-29 Jun 2004. arXiv:hep-ph/0407293.

[5] K. Hagiwara *et al.* [Particle Data Group Collaboration], Phys. Rev. D **66**, 010001 (2002).

[6] I. I. Y. Bigi, M. A. Shifman and N. Uraltsev, Ann. Rev. Nucl. Part. Sci. **47**, 591 (1997).

[7] G. Burdman and I. Shipsey, Ann. Rev. Nucl. Part. Sci. **53**, 431 (2003).

[8] K. Stenson for the FOCUS collaboration, talk given at Meeting of the Division of Particles and Fields (DPF 2004), University of California, Riverside, 26-31 August 2004.

[9] R. Godang *et al.* [CLEO Collaboration], Phys. Rev. Lett. **84**, 5038 (2000).

[10] B. Aubert *et al.* [BABAR Collaboration], Phys. Rev. Lett. **91**, 171801 (2003).

[11] K. Abe *et al.* [BELLE Collaboration], to appear in the proceedings of 32nd International Conference on High-Energy Physics (ICHEP 04), Beijing, China, 16-22 Aug 2004. arXiv:hep-ex/0408125.

[12] J. M. Link *et al.* [FOCUS Collaboration], Phys. Lett. B **485**, 62 (2000).

[13] S. E. Csorna *et al.* [CLEO Collaboration], Phys. Rev. D **65**, 092001 (2002).

[14] K. Abe *et al.* [Belle Collaboration], Phys. Rev. Lett. **88**, 162001 (2002).

[15] B. Aubert *et al.* [BABAR Collaboration], Phys. Rev. Lett. **91**, 121801 (2003).

[16] I. I. Bigi and A. I. Sanda, *CP violation*, Cambridge University Press (2000).

[17] A. J. Schwartz, Mod. Phys. Lett. A **8**, 967 (1993).

[18] J. M. Link *et al.* [FOCUS Collaboration], Phys. Lett. B **572**, 21 (2003).

[19] E. M. Aitala *et al.* [E791 Collaboration], Phys. Lett. B **462**, 401 (1999).

[20] P. L. Frabetti *et al.* [The E687 Collaboration], Phys. Lett. B **398**, 239 (1997).

[21] G. Burdman, E. Golowich, J. Hewett and S. Pakvasa, Phys. Rev. D **66**, 014009 (2002).

[22] D. Acosta *et al.* [CDF Collaboration], Phys. Rev. D **68**, 091101 (2003).

[23] T. E. Coan *et al.* [CLEO Collaboration], Phys. Rev. Lett. **90**, 101801 (2003).

[24] D. Y. Kim, talk given at 34th International Symposium on Multiparticle Dynamics (ISMD 2004), Rohnert Park, California, 26 Jul - 1 Aug 2004. arXiv:hep-ex/0410015.

[25] D. Aston *et al.* [LASS Collaboration], Nucl. Phys. B **296**, 493 (1988).

[26] J. M. Link *et al.* [FOCUS Collaboration], Phys. Lett. B **544**, 89 (2002).

[27] J. M. Link *et al.* [Focus Collaboration], Phys. Lett. B **541**, 243 (2002).

[28] J. M. Link *et al.* [FOCUS Collaboration], Phys. Lett. B **586**, 183 (2004).

[29] J. M. Link [FOCUS Collaboration], submitted to Phys.Lett.B. arXiv:hep-ex/0410067.

[30] J. M. Link [FOCUS Collaboration], submitted to Phys.Lett.B. arXiv:hep-ex/0410068.

[31] M. Bauer, B. Stech and M. Wirbel, Z. Phys. C **34**, 103 (1987).

[32] J. Wiss, Prepared for International School of Physics, 'Enrico Fermi': Heavy Flavor Physics - A Probe of Nature's Grand Design, Varenna, Italy, 8-18 Jul 1997

[33] S. Malvezzi for the FOCUS Collaboration, published in *Amsterdam 2002, ICHEP* 636 the Proceedings of 31st International Conference on High Energy Physics (ICHEP2002), Amsterdam, The Netherlands, 24-31 Jul 2002.

[34] E. M. Aitala *et al.* [E791 Collaboration], Phys. Rev. Lett. **86**, 770 (2001).

[35] E. P. Wigner, Phys. Rev. **70**, 15 (1946).

[36] S. U. Chung, J. Brose, R. Hackmann, E. Klempt, S. Spanier and C. Strassburger, Annalen Phys. **4**, 404 (1995).

[37] J. M. Link *et al.* [FOCUS Collaboration], Phys. Lett. B **601**, 10 (2004).

[38] J. M. Link *et al.* [FOCUS Collaboration], Phys. Lett. B **537** 192 (2002).

[39] J. M. Link *et al.* [FOCUS Collaboration], Phys. Rev. Lett. **86**, 2955 (2001).

[40] E. Vaandering, Ph.D. thesis, University of Colorado, Boulder (2000).

[41] P. L. Frabetti *et al.* [E687 Collaboration], Phys. Lett. B **331**, 217 (1994).

[42] P. L. Frabetti *et al.* [E687 Collaboration], Phys. Lett. B **359**, 403 (1995).

[43] E. M. Aitala *et al.* [E791 Collaboration], Phys. Lett. B **404**, 187 (1997).

[44] P. L. Frabetti *et al.* [E687 Collaboration], Phys. Lett. B **351**, 591 (1995).

[45] R. Greene, Ph.D. thesis, University of Illinois at Urbana-Champaign (1995).

[46] P. Dini, Ph.D. thesis, Università degli Studi di Milano (1999).

[47] J. Blatt and V. Weisskopf, *Theoretical Nuclear Physics*, New York: John Wiley & Sons (1952).

[48] H. Albrecht *et al.* [ARGUS Collaboration], Phys. Lett. B **308**, 435 (1993).

[49] C. Zemach, Phys. Rev. **133**, 1201 (1964).

[50] C. Zemach, Phys. Rev. **140**, 97 (1965).

[51] S. M. Flatte, Phys. Lett. B **63**, 228 (1976).

[52] F. James, MINUIT Reference Manual Version 94.1, CERN Program Library Long Writeup D506

[53] Jim Wiss and Rob Gardner, E687 memo, `http://web.hep.uiuc.edu/e687/memos/adapt.ps`

[54] A. G. Frodesen *et al.*, *Probability and Statistics in Particle Physics*, Oxford University Press (1979).

[55] E. M. Aitala *et al.* [E791 Collaboration], Phys. Rev. Lett. **89**, 121801 (2002).

[56] Jim Wiss and Rob Gardner, E687 memo, `http://web.hep.uiuc.edu/e687/memos/DALITZ_SYS.PS`

Appendix A

Calculation of systematic errors

In the FOCUS collaboration the systematic errors are estimated through a combination of two contributions, i.e. *split sample* and *fit variant* [56]. In the first case, one estimates systematic errors by splitting the data sample in disjoint subsamples and comparing the fit parameters obtained in each split sample. This is done on the basis of variables which may cause a shift in the measured value. In the second contribution one includes possible systematic errors due to different reconstruction or fitting techniques, such as varying the fit function or the histogram binning. These two systematic sources are independent each other; the total systematic error is obtained adding in quadrature these two components.

A.1 Split sample systematics

We split the data set in N independent samples; we have x_i individual measurements with the associated errors σ_i, where i goes from 1 to N. If the N independent measurements are statistically consistent there is no evidence for a split sample systematic error. To test the statistical consistency we construct a χ^2 with $N-1$ degrees of freedom of the form:

$$\chi^2 = \sum_{i=1}^{N} \frac{(x_i - \overline{x})^2}{\sigma_i^2} \tag{A.1}$$

where $\overline{x}$ is the weighted average

$$\overline{x} = \frac{\sum_{i=1}^{N} x_i/\sigma_i^2}{\sum_{i=1}^{N} 1/\sigma_i^2} \tag{A.2}$$

with an associated statistical error $\overline{\sigma}$

$$\overline{\sigma} = \frac{1}{\sqrt{\sum_{i=1}^{N} 1/\sigma_i^2}}\,. \tag{A.3}$$

If $\chi^2/(N-1) \leq 1$, then our measurements are consistent with each other within their errors. However, if $\chi^2/(N-1) > 1$, then we assume that the split sample true errors are all underestimated because of an unknown systematic problem. If we scale each sub-sample statistical error σ_i to

$$\sigma_i \sqrt{\frac{\chi^2}{(N-1)}} \tag{A.4}$$

then we are guaranteed that $\chi^2/(N-1) = 1$ for the new values of σ_i. In addition $\overline{\sigma}$ will be increased by the same factor and became a scaled error $\widetilde{\sigma}$:

$$\widetilde{\sigma} = \overline{\sigma}\sqrt{\frac{\chi^2}{(N-1)}} = \sqrt{\frac{\overline{x^2} - \overline{x}^2}{N-1}} \tag{A.5}$$

where $\overline{x^2}$ is defined as

$$\overline{x^2} = \frac{\sum_{i=1}^{N} x_i^2/\sigma_i^2}{\sum_{i=1}^{N} 1/\sigma_i^2}\,. \tag{A.6}$$

When this scaled error is smaller than the statistical error from the fit of the unsplit data set (σ_{stat}), any difference between the split samples can be interpreted as being compatible with a statistical fluctuation. The final systematic error σ_{sys} is evaluated as:

$$\begin{aligned} \sigma_{\text{sys}} &= \sqrt{\widetilde{\sigma}^2 - \sigma_{\text{stat}}^2} \quad && \text{if } \widetilde{\sigma} > \sigma_{\text{stat}} \\ \sigma_{\text{sys}} &= 0 && \text{if } \widetilde{\sigma} \leq \sigma_{\text{stat}} \end{aligned} \tag{A.7}$$

In this way we are able to separate true indications of systematic problems from normal statistical fluctuations.

A.2 Fit variant systematics

In this case the results from each different fitting or reconstruction method are considered to be equally valid and, in addition, the statistical errors on the measurement should be correlated. Because each measurement is *a priori* likely, each measurement is given equal weight and the estimate of the systematic error is simply the standard deviation on the set of measurements. In other words, the systematic error is

$$\sigma_{\text{sys}} = \sqrt{\frac{\sum_{i=1}^{N} x_i^2 - N\overline{x}^2}{N-1}} \tag{A.8}$$

where the quantities x_i are the individual measurements and $\overline{x}$ is the mean:

$$\overline{x} = \frac{\sum_{i=1}^{N} x_i}{N} \tag{A.9}$$

This method makes the assumption that each fit variant produces a result of equal "goodness." A measurement that is far from the others, even with a large error, can inflate the overall systematic error.

A.3 Generalization to multi-variables measurements

The previous sections concern the evaluation of the systematic error of a single measurement, such as the branching ratio. The method can be generalized in the case of many simultaneous measurements, such as in the Dalitz plot analysis, when the results of a fit are coefficients and phases, correlated one each other.

A.3.1 Split sample systematics

For the evaluation of the branching ratio we have N split samples and one variable $x_i \pm \sigma_i$, where i goes from 1 to N, while in the Dalitz plot analysis we have N split samples and M correlated variables (coefficients and phases). Now a vector X_i corresponds to the simplest x_i

$$X_i = \begin{pmatrix} \alpha_{1i} \\ \vdots \\ \alpha_{Mi} \end{pmatrix} \tag{A.10}$$

with, instead of the error σ_i, a covariance matrix V_i :

$$V_i = \begin{pmatrix} V_{11} & \dots & V_{1M} \\ \vdots & \ddots & \vdots \\ V_{M1} & \dots & V_{MM} \end{pmatrix}_i \tag{A.11}$$

where the diagonal elements are the squared statistical errors associated to the M variables. To construct a χ^2 in analogy with A.1, we generalize the weighted average A.2 to:

$$\overline{X} = \begin{pmatrix} \overline{\alpha}_1 \\ \vdots \\ \overline{\alpha}_M \end{pmatrix} = \left(\sum_{i=1}^{N} V_i^{-1} \right)^{-1} \cdot \left(\sum_{i=1}^{N} V_i^{-1} \cdot X_i \right) \tag{A.12}$$

with an error matrix $\overline{V}$ equal to:

$$\overline{V} = \left(\sum_{i=1}^{N} V_i^{-1} \right)^{-1} \tag{A.13}$$

The χ^2 is therefore calculated as:

$$\chi^2 = \sum_{i=1}^{N} \left(X_i - \overline{X} \right)^t \cdot V_i^{-1} \cdot \left(X_i - \overline{X} \right) \tag{A.14}$$

Again, if $\chi^2/[(N-1)M] > 1$, we scale each sub-sample statistical matrix V_i and consequently $\overline{V}$ will became a scaled matrix $\widetilde{V}$, defined as:

$$\widetilde{V} = \overline{V} \frac{\chi^2}{(N-1)M} \tag{A.15}$$

To associate a systematic error to the variables (coefficients and phases), we consider the diagonal elements of the statistical matrix V^{stat} of the whole sample and we compare them with the corresponding elements of $\widetilde{V}$:

$$\begin{aligned} \text{if } \widetilde{V}_{ii} > V_{ii}^{\text{stat}} \quad V_{ii}^{\text{sys}} &= \widetilde{V}_{ii} - V_{ii}^{\text{stat}} \\ \text{if } \widetilde{V}_{ii} \leq V_{ii}^{\text{stat}} \quad V_{ii}^{\text{sys}} &= 0 \end{aligned} \tag{A.16}$$

In a Dalitz plot analysis the results of the fit are coefficients and phases; fit fractions are calculated, according to Eq. 5.28, and associated systematic error have to be evaluated, taking into account the correlations among the fit parameters. The problem is how treat the off-diagonal elements of $\widetilde{V}$. We assume that the correlation ρ_{ij} between the off-diagonal elements of $\widetilde{V}$ is the same as the statistical one. We define a new matrix V^{boost} as:

$$\begin{aligned} \text{if } \widetilde{V}_{ii} > V_{ii}^{\text{stat}} \quad V_{ii}^{\text{boost}} &= \widetilde{V}_{ii} \\ V_{ij}^{\text{boost}} &= \rho_{ij}\sqrt{\widetilde{V}_{ii}\widetilde{V}_{jj}} \qquad i \neq j \\ \text{if } \widetilde{V}_{ii} \leq V_{ii}^{\text{stat}} \quad V_{ij}^{\text{boost}} &= V_{ij}^{\text{stat}} \qquad \forall i,j \end{aligned} \tag{A.17}$$

where ρ_{ij} is obtained through V^{stat} as:

$$\rho_{ij} = \frac{V_{ij}^{\text{stat}}}{\sqrt{V_{ii}^{\text{stat}} V_{jj}^{\text{stat}}}} \tag{A.18}$$

Then V^{boost} is propagated and so we have the "boosted" errors on the fit fractions Γ, $\sigma_{\Gamma_i}^{boost}$. Now we can separate the systematic effects from the statistical fluctuations in the usual way:

$$\begin{aligned} \text{if } \sigma_{\Gamma_i}^{boost} > \sigma_{\Gamma_i}^{\text{stat}} \quad \sigma_{\Gamma_i}^{sys} &= \sqrt{(\sigma_{\Gamma_i}^{boost})^2 - (\sigma_{\Gamma_i}^{\text{stat}})^2} \\ \text{if } \sigma_{\Gamma_i}^{boost} \leq \sigma_{\Gamma_i}^{\text{stat}} \quad \sigma_{\Gamma_i}^{sys} &= 0 \end{aligned} \tag{A.19}$$

A.3.2 Fit variant systematics

The fit variant systematics is just a generalization of the single-variable case and it is less complicated than the previous one, because the samples are not correlated. If we have N different fit variant and M variables, then

$$X_i = \begin{pmatrix} \alpha_{1i} \\ \vdots \\ \alpha_{Mi} \end{pmatrix} \tag{A.20}$$

and we calculate the elements of the mean vector $\overline{X}$ as:

$$\overline{\alpha_j} = \frac{\sum_{i=1}^{N} \alpha_{ij}}{N} \tag{A.21}$$

We define the vector θ which elements are:

$$\theta_j = \frac{\sum_{i=1}^{N} \alpha_{ij}^2}{N} \tag{A.22}$$

Now we are able to evaluate the standard deviation of the measurements; the systematic errors for coefficients, phases and fit fractions are simply:

$$V_{kk}^{\mathrm{sys}} = \frac{\theta_k - N\overline{\alpha_k}^2}{N-1} \tag{A.23}$$

Appendix B

Shapes of the resonances involved in D^+ and $D_s^+ \to K^+\pi^-\pi^+$ decays

The shape of each $K^+\pi^-$ and $\pi^+\pi^-$ well-established resonance (Table 6.1) over the Dalitz plot is shown in the following pictures. The different nature of the resonances is visible through their different Zemach term representation (Eq. 5.17): two lobes for a vector ($\mathcal{S}(1\ 3)^2 \propto \cos^2\theta_{13}$), three lobes for a tensor ($\mathcal{S}(1\ 3)^2 \propto (3\cos^2\theta_{13} - 1)^2$) and an uniform band for a scalar ($\mathcal{S}(1\ 3)^2 \propto 1$). For each state the two Dalitz plot projections are also shown.

B.1 Resonances for the $D^+ \to K^+\pi^-\pi^+$ decay

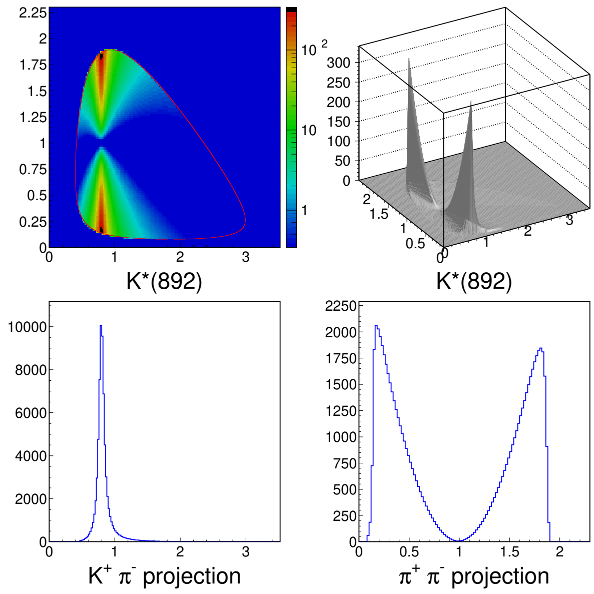

Figure B.1: Model for the vector $K^*(892)$ for the $D^+ \to K^+\pi^-\pi^+$ decay

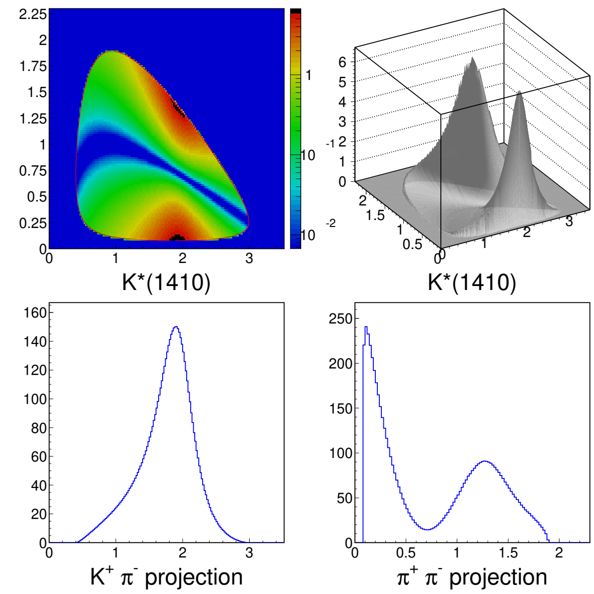

Figure B.2: Model for the vector $K^*(1410)$ for the $D^+ \to K^+\pi^-\pi^+$ decay

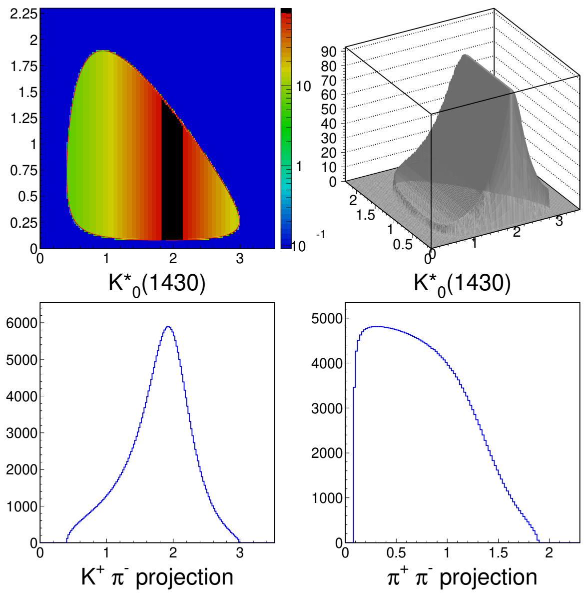

Figure B.3: Model for the scalar $K_0^*(1430)$ for the $D^+ \to K^+\pi^-\pi^+$ decay

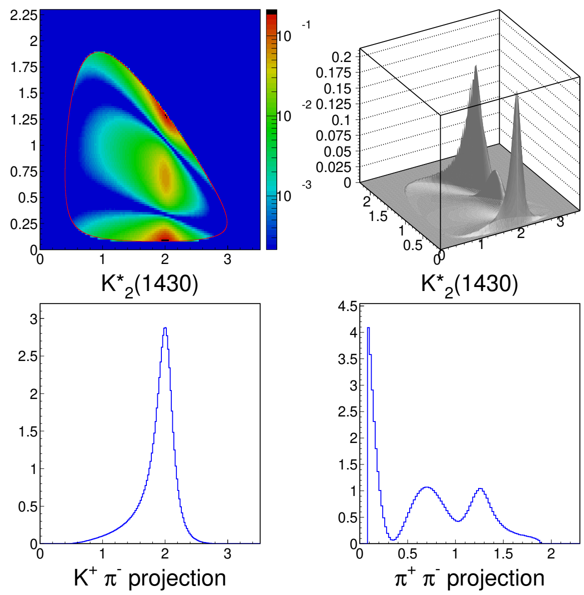

Figure B.4: Model for the tensor $K_2^*(1430)$ for the $D^+ \to K^+\pi^-\pi^+$ decay

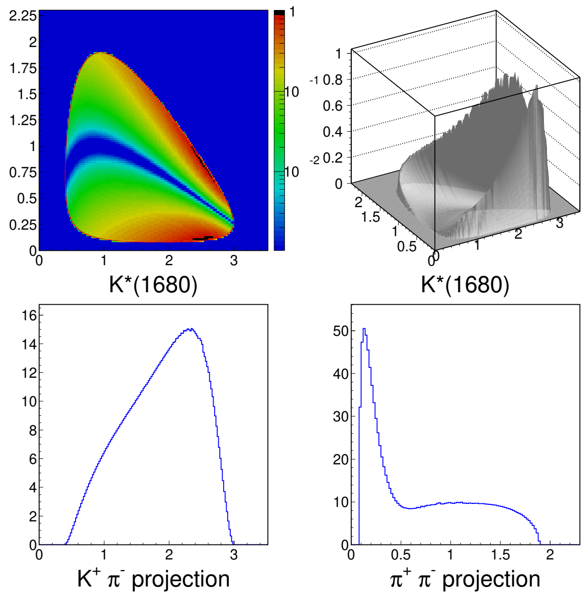

Figure B.5: Model for the vector $K^*(1680)$ for the $D^+ \to K^+\pi^-\pi^+$ decay

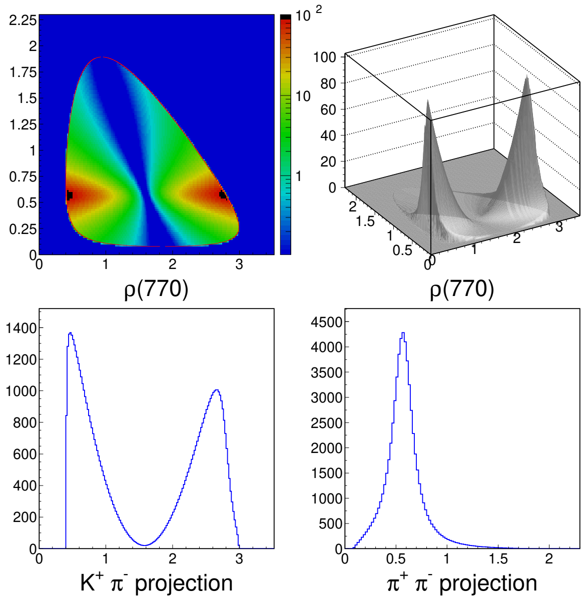

Figure B.6: Model for the vector $\rho(770)$ for the $D^+ \to K^+\pi^-\pi^+$ decay

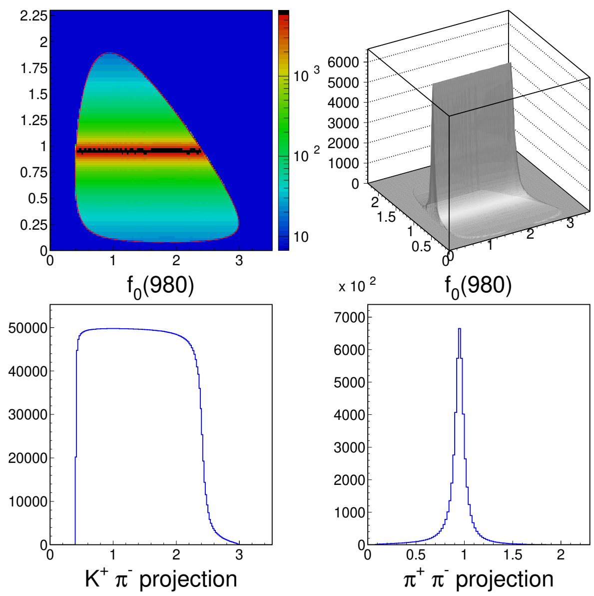

Figure B.7: Model for the scalar $f_0(980)$ for the $D^+ \to K^+\pi^-\pi^+$ decay

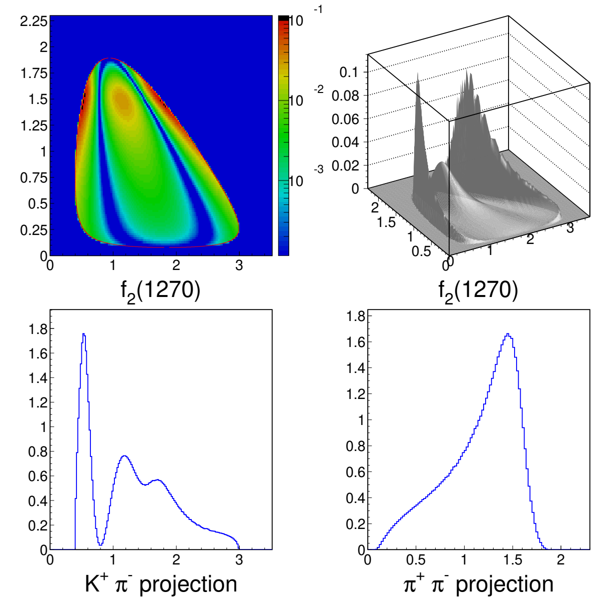

Figure B.8: Model for the tensor $f_2(1270)$ for the $D^+ \to K^+\pi^-\pi^+$ decay

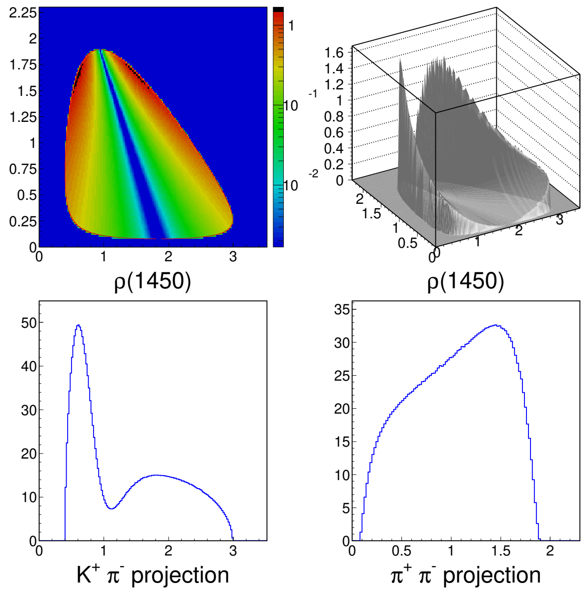

Figure B.9: Model for the vector $\rho(1450)$ for the $D^+ \to K^+\pi^-\pi^+$ decay

B.2 Resonances for the $D_s^+ \to K^+\pi^-\pi^+$ decay

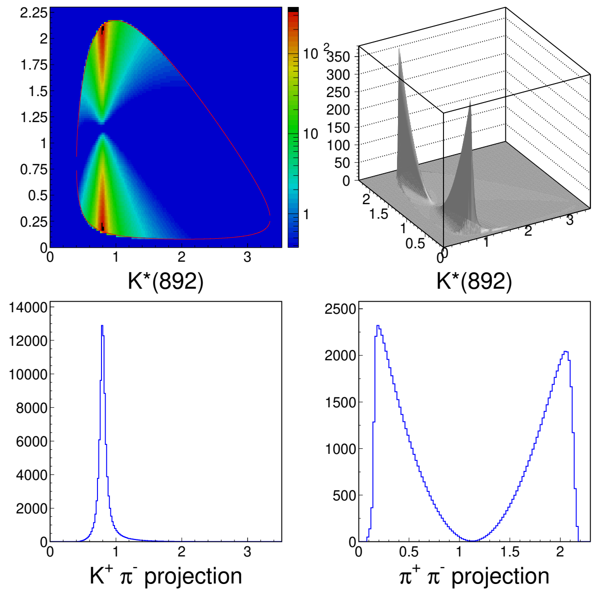

Figure B.10: Model for the vector $K^*(892)$ for the $D_s^+ \to K^+\pi^-\pi^+$ decay

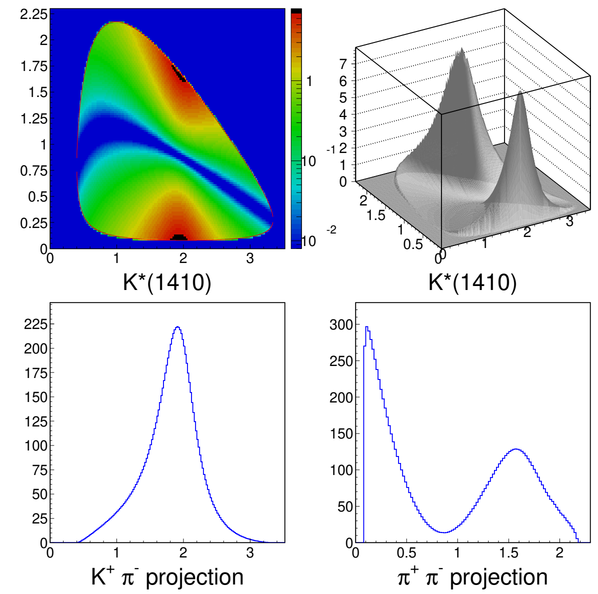

Figure B.11: Model for the vector $K^*(1410)$ for the $D_s^+ \to K^+\pi^-\pi^+$ decay

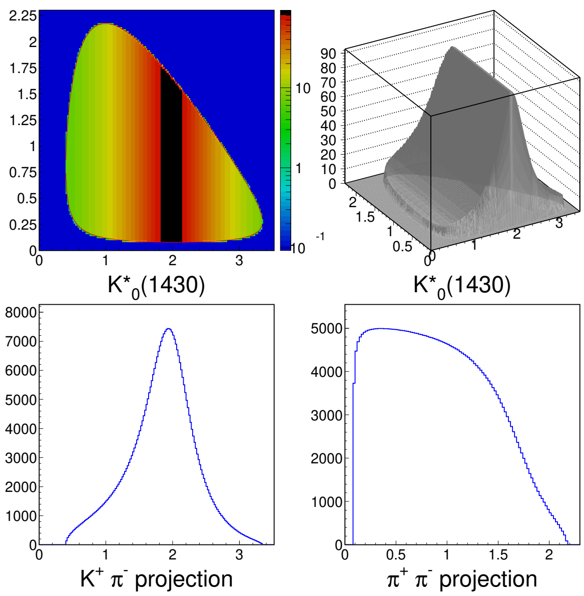

Figure B.12: Model for the scalar $K_0^*(1430)$ for the $D_s^+ \to K^+\pi^-\pi^+$ decay

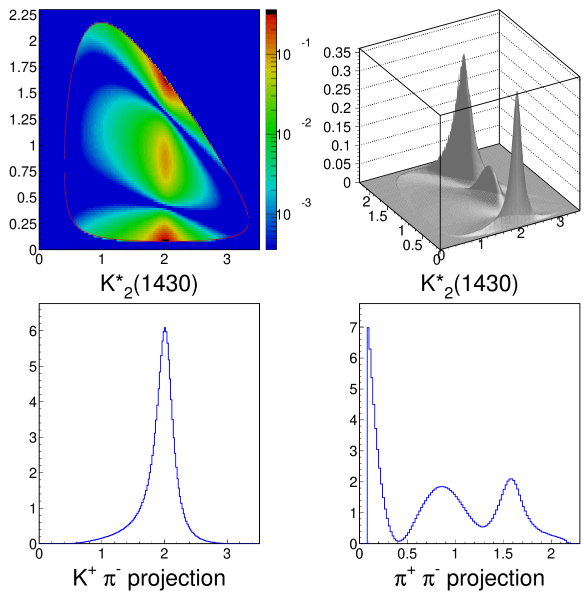

Figure B.13: Model for the tensor $K_2^*(1430)$ for the $D_s^+ \to K^+\pi^-\pi^+$ decay

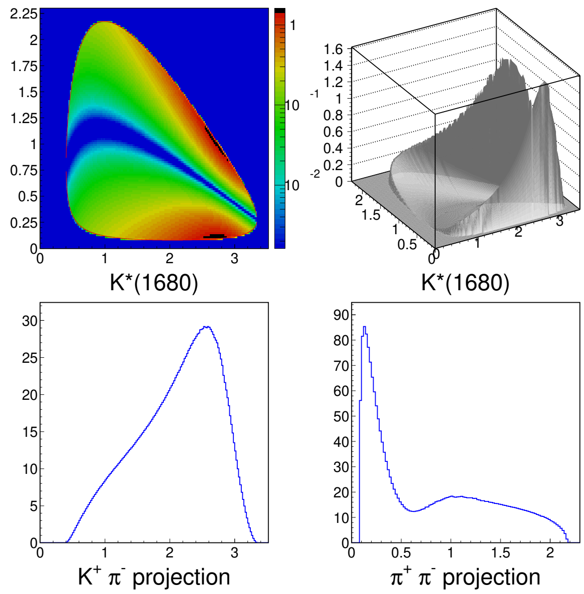

Figure B.14: Model for the vector $K^*(1680)$ for the $D_s^+ \to K^+\pi^-\pi^+$ decay

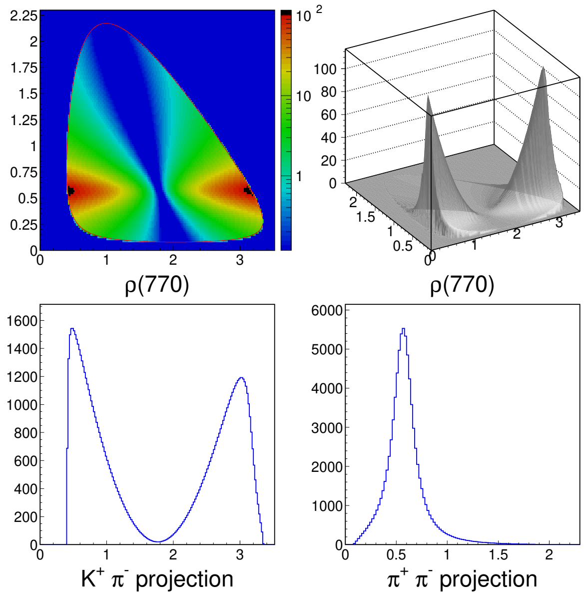

Figure B.15: Model for the vector $\rho(770)$ for the $D_s^+ \to K^+\pi^-\pi^+$ decay

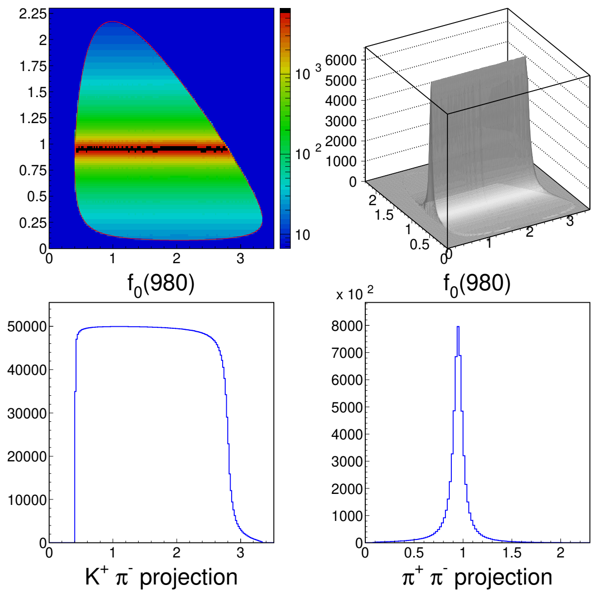

Figure B.16: Model for the scalar $f_0(980)$ for the $D_s^+ \to K^+\pi^-\pi^+$ decay

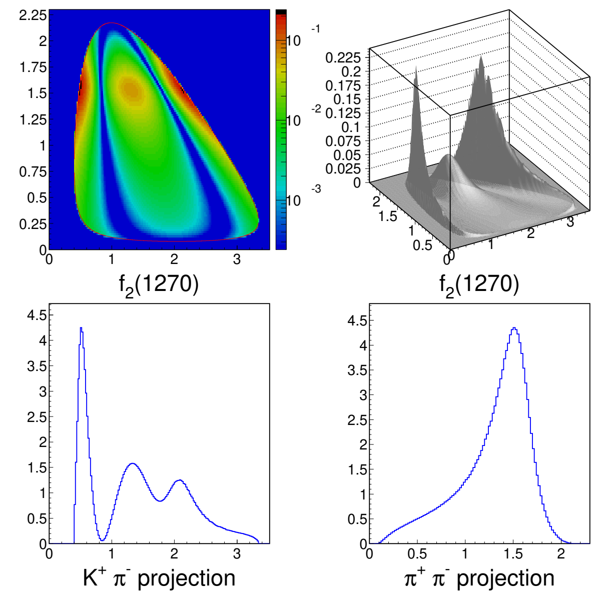

Figure B.17: Model for the tensor $f_2(1270)$ for the $D_s^+ \to K^+\pi^-\pi^+$ decay

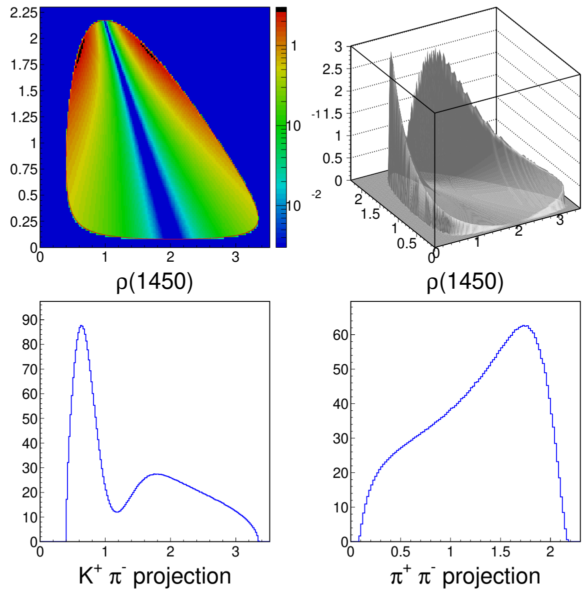

Figure B.18: Model for the vector $\rho(1450)$ for the $D_s^+ \to K^+\pi^-\pi^+$ decay